ENHANCING CENTIMETRE-LEVEL GNSS ACCURACY: EVALUATION OF SPARTN CORRECTION INTEGRATION IN RTKLib AND YorkPPP

SANDESH MISHRA

A THESIS SUBMITTED TO THE FACULTY OF GRADUATE

STUDIES IN PARTIAL FULFILLMENT OF THE REQUIREMENTS

FOR THE DEGREE OF MASTER OF SCIENCE

GRADUATE PROGRAM IN EARTH AND SPACE SCIENCE

YORK UNIVERSITY

TORONTO, ONTARIO

May 2026

© Sandesh Mishra, 2026

Abstract

The Secure Position Augmentation for Real-Time Navigation (SPARTN) protocol has been integrated into two different software structures, i.e., open-source software platform, RTKLib, and YorkPPP, a research-oriented software. SPARTN is a bandwidth optimised message format for high-precision GNSS correction developed by u-blox. The SPARTN solution was validated experimentally using both static and kinematic multi constellations tests. Centimetre-level stability on the horizontal component of 6 cm RMS was achieved in static rooftop tests performed at York University. The QUIN GNSS reference station, part of the International GNSS Service (IGS) network located in Quincy, California, was utilised to provide a geodetic-grade benchmark for performance validation. It demonstrated that the float solution of SPARTN reached convergence in 7.5 minutes, 25% faster than by the corresponding CNES precise products. Incorporating SPARTN corrections into the YorkPPP engine reduced the convergence time by 77% as compared to the float solution. High accuracy decimetre-level stability in an urban environment was also achieved in kinematic test using the SPARTN solution. The results demonstrate a novel open-source implementation of the SPARTN correction that can reliably provide high-precision positioning.

Acknowledgements

I deeply appreciate Professor Sunil Bisnath for his expert supervision and continuous support, and invaluable guidance which he provided during this research. His knowledge of global navigation satellite systems, technical skills, and his genuine passion have strongly influenced my path and excellence of this research. His patience and encouragement allowed for the exploration of new technologies as I continued to educate myself on methods of precise positioning.

I would like to thank the members of the GNSS Laboratory at York University for creating an environment in which collaboration and growth are possible. I thank them for all the technical insight, for proof reading, and for the personal encouragement and support that helped me along the way.

I am grateful to u-blox for the financial and technical backing that underpinned this project. Special thanks are due to Dr. Jiahuan Hu (The Hong Kong Polytechnic University), Michael Albright, and Rodrigo Leandro (u-blox) for their outstanding collaboration. Their technical guidance and provision of hardware and SPARTN correction streams were vital to this research.

I would like to thank my parents and my brother for their support to establish me and have faith in my ability to succeed academically. I would also like to thank my wife, Kritika Poudel and daughter Siana Mishra for their emotional support and for bearing with me during the long hours and period I invested in my research work.

Table of Contents

Abstract ..... **ii**

Acknowledgements ..... **iii**

Table of Contents ..... **iv**

List of Tables ..... **viii**

List of Figures ..... **x**

List of Acronyms ..... **xviii**

1. Introduction **1**

1.1 Problem Statement 3

1.2 Thesis Statement and Objectives 5

1.3 Research Novelty and Significance 6

1.4 Thesis Structure and Organizational Framework 8

2. GNSS Fundamentals: Signal Structures, Errors, and Positioning Techniques **10**

2.1 Fundamental Concepts in Modern Satellite Navigation and Augmentation Systems 10

2.2 GNSS Signal Architecture and Modernization 11

2.3 Comparative Analysis of GNSS Constellations 13

2.3.1 The Global Positioning System (GPS) 15

2.3.2 GLONASS (Russian Federation) 16

2.3.3 Galileo (European Union) 17

2.3.4 BeiDou Navigation Satellite System (BDS) 18

2.4 GNSS Error Sources and Mitigation Strategies 19
2.4.1 Satellite Specific Errors 20
2.4.2 Atmospheric Propagation Errors 21
2.4.3 Station and Receiver Specific Errors 22
2.5 GNSS Observation Models and Positioning Techniques 26
2.5.1 Code Pseudorange Observation Model 26
2.5.2 Carrier-phase Observation Model 27
2.5.3 Integer Ambiguity Resolution (AR) 28
2.5.4 Single Point Positioning 29
2.5.5 Relative Positioning, Real-Time Kinematic (RTK) and Network RTK (NRTK) 31
2.5.6 Precise Point Positioning (PPP) 34
2.6 GNSS Correction Formats and Services 36
2.7 GNSS Correction Methodologies: OSR vs SSR 39
2.8 RTKLib Software 41
2.9 YorkPPP Software 44
3. The SPARTN Protocol and Corrections Framework and Implementation 48
3.1 SPARTN Orbit, Clock and Bias Messages 50
3.1.1 GNSS Orbit Corrections 51
3.1.2 GNSS Clock Corrections 53
3.1.3 GNSS Bias Corrections 54

3.2 SPARTN geographic area definition message 55
3.3 Atmospheric correction messages 56
3.3.1 Ionospheric corrections 57
3.3.2 Tropospheric corrections 60
3.4 Corrections implementation 62
3.4.1 Decoding of corrections 64
3.4.2 Correction Implementations in RTKLib 70
3.4.3 Correction Implementations in YorkPPP 76
3.4.4 Data used 83
4. Experiments and Analysis from RTKLib 85
4.1 PPP-Static Performance Analysis: York University 87
4.1.1 Empirical Validation of Geodetic-Grade Hardware Performance 88
4.1.2 Empirical Validation of Low-Cost Hardware Performance 99
4.2 PPP-Static Performance Analysis with IGS station 103
4.2.1 Satellite Visibility and Correction Availability Analysis 108
4.2.2 Multipath and Residual Analysis 111
4.2.3 Frequency-Specific SNR-Elevation Relationships 115
4.2.4 Satellite Availability and Correction Limitations 117
4.3 PPP-Kinematic with Test Vehicle 119
4.3.1 SPARTN Correction Service Performance Evaluation 120
4.3.2 CNES Correction Service Performance Assessment 121

4.3.3 Statistical Performance Comparison and Analysis 123

5. Experiments and Analysis from YorkPPP 125

5.1 Static Positioning Performance at York University 125

5.1.1 Empirical Validation of Geodetic grade Hardware Performance via YorkPPP 125

5.1.2 Empirical Validation of Low-Cost Hardware Performance via YorkPPP 137

5.2 Static Validation: QUIN IGS Station 144

5.2.1 Evaluation of Orbit, Clock, and Signal Bias Correction 144

5.2.2 Multi-Constellation Impact and Statistical Validation 155

5.3 Kinematic PPP Performance: Vehicle-Based Dynamic Validation 160

6. Conclusions and Recommendations 167

6.1 Conclusions 167

6.2 Recommendations 169

6.2.1 Advanced Performance and Integrity Evaluation 169

6.2.2 Enhanced Atmospheric Modelling Implementation 170

6.2.3 Advanced Machine Learning for Ambiguity Validation 170

6.2.4 Extended Validation and Operational Deployment 171

6.2.5 Architectural Enhancements for Open-Source SSR-AR 172

6.2.6 Mitigating Correction Gaps and Improving Stream Reliability 172

6.2.7 GNSS/IMU Fusion for Continuity in Denied Environments 173

7. References 174

List of Tables

Table 2.1: Comparative overview of GNSS constellations (Adopted from Montenbruck et al., 2017). 14

Table 2.2: Summary of GNSS measurement error sources, magnitude, and mitigation strategies (Adapted from Misra and Enge, 2011; Teunissen and Montenbruck, 2017). .. 25

Table 3.1: Horizontal and vertical positioning error statistics for SPARTN and CNES corrections during the kinematic GNSS test. 84

Table 4.1: Horizontal and vertical positioning error statistics for SPARTN and CNES corrections during the kinematic GNSS test on DOY 221, 2024. 123

Table 5.1: Performance metrics for dual-frequency positioning: CV and RMS error analysis using CNES products. 127

Table 5.2: Performance metrics for dual-frequency positioning: CV and RMS error analysis using SPARTN corrections. 131

Table 5.3: Comparative analysis of solution convergence and east, north and up precision: CNES versus SPARTN corrections. 135

Table 5.4: Comparative analysis of average solution convergence and east, north and up precision: CNES versus SPARTN corrections for four dataset. 136

Table 5.5: Performance metrics for dual-frequency positioning: CV and RMS error analysis using SPARTN corrections. 152

Table 5.6: Performance metrics for dual-frequency positioning: CV and RMS error analysis using CNES corrections. 155

Table 5.7: Summary of convergence time and horizontal, vertical, and 3D RMS positioning errors for float and fixed solutions by GNSS constellation (GPS, GLONASS, Galileo, BeiDou) at QUIN station. 157

Table 5.8: Summary of convergence time and horizontal, vertical, and 3D RMS positioning errors for float and fixed solutions for ALGO, NRC1, and QUIN stations. 158

Table 5.9: Average convergence time and horizontal, vertical, and 3D RMS positioning errors for float and fixed solutions for ALGO, NRC1, and QUIN stations. 160

Table 5.10: Comparison of horizontal and vertical positioning errors for CNES and SPARTN corrections using YorkPPP. 162

List of Figures

Figure 2.1: Illustration of GNSS signal modulation process (Adapted from Misra and Enge, 2011). 12

Figure 2.2: Components of the GNSS pseudorange measurement. The observed pseudorange is the summation of the geometric range and various satellite, receiver, and atmospheric error sources (Adapted from ESA, 2011). 20

Figure 2.3: GNSS receiver tracking signals from multiple satellites for position determination (Adopted from Takasu 2013). 30

Figure 2.4: Geometry of a GNSS baseline setup used in relative positioning processing (Adopted from Takasu 2013). 32

Figure 2.5: Real-Time Kinematic (RTK) positioning through simultaneous observation of common satellites by reference and rover receivers. 33

Figure 2.6: Conceptual framework of Precise Point Positioning (PPP). High-accuracy positioning is achieved by applying precise orbit and clock corrections (e.g., from IGS) to a standalone receiver. 35

Figure 2.7: RTKLAUNCH interface showing core modules (Adapted from Takasu, 2013). 43

Figure 2.8: York-PPP system overview showing the integration of multi-GNSS data and error modelling via sequential least-squares filtering. (Adapted from Aggrey, 2014; Seepersad, 2012). 45

Figure 3.1: Overview of SPARTN-based GNSS correction delivery architecture (Adapted

from u-blox AG, 2021). 49

Figure 3.2: Structure of the SPARTN area-based grid used for atmospheric correction representation (Adapted from u-blox AG, 2021)..... 56

Figure 3.3: Example of geographic area definitions (tiles) used in SPARTN correction services for North America (Adapted from u-blox AG, 2021)..... 56

Figure 3.4: SPARTN correction decoding and processing workflow. 65

Figure 3.5: SPARTN correction application flow for precise orbit, clock, biases, and atmospheric delay computation. 69

Figure 3.6: Ephemeris selection and orbit/clock correction logic in RTKLib, including SPARTN path. 72

Figure 3.7: Measurement correction flow including SPARTN phase and code bias application..... 74

Figure 3.8: Ionospheric correction option flow including SPARTN, SBAS, TEC, and broadcast models..... 75

Figure 3.9: Tropospheric correction option flow including SPARTN, SBAS, SAAS, and estimated models..... 76

Figure 3.10: Correction data flow in the YORKPPP software. Multiple correction sources (orbit, clock, biases, antenna, and atmospheric) are integrated through dedicated input modules to support precise positioning..... 78

Figure 3.11: Correction application loop in the YORKPPP engine. Multiple correction sources are integrated within the forward and backwards processing loop to support

sequential least-squares positioning. 80

Figure 3.12: Implementation of additional error corrections in the YORKPPP engine. SPARTN-based ionospheric and tropospheric models are integrated alongside existing models to enhance positioning accuracy. 81

Figure 4.1: GNSS data collection setups used in this study. (a) A reference station installed on the rooftop of 4751 Keele St, York University, providing high-quality static observations for reference trajectory generation. (b) Kinematic test platform mounted on a vehicle roof, used to collect GNSS data for evaluating positioning performance under dynamic conditions. 85

Figure 4.2: Kinematic GNSS test trajectory conducted around York University campus and surrounding area. The vehicle followed the indicated loop route, starting and ending at designated points, to evaluate positioning performance. 86

Figure 4.3: Signal-to-noise ratio (SNR) variation over time for GNSS observations. The different colours represent signals from various constellations, showing relative signal strength and elevation throughout the observation session on DOY 223, 2024. 89

Figure 4.4: Skyplot of GPS (blue), GLONASS (green), Galileo (pink), and BeiDou (orange) satellite tracks during the static test on DOY 223, 2024, showing strong multi-constellation visibility and favourable geometric coverage. 90

Figure 4.5: Horizontal and vertical position error comparison between CNES and SPARTN corrections in RTKLib float solution on DOY 223, 2024. 92

Figure 4.6: Time series of east-west, north-south, and up-down position errors during the static GNSS test conducted on DOY 223, 2024. The blue line represents the solution

using CNES corrections, while the light red line corresponds to the solution using SPARTN corrections on DOY 223, 2024. 93

Figure 4.7: Satellite elevation angles over time for Global Positioning System (blue), GLONASS (red), Galileo (green), and BeiDou Navigation Satellite System (purple) signals during the static GNSS test conducted on DOY 223, 2024. 95

Figure 4.8: Elevation plot illustrating fragmented satellite visibility tracks caused by periods of invalid SPARTN corrections during the static GNSS test conducted on DOY 223, 2024..... 96

Figure 4.9: Signal-to-noise ratio (SNR) versus elevation angle at the York University Rooftop for L1/E1/B1 frequencies. SNR variations for GPS (blue), GLONASS (red), Galileo (green) and BeiDou (purple) satellites reflect differences in signal strength and propagation conditions on DOY 223, 2024. 97

Figure 4.10: Signal-to-noise ratio (SNR) versus elevation angle at the York University Rooftop for L2/E5b/B2 frequencies. GPS (blue), GLONASS (red), Galileo (green) and BeiDou (purple) signals exhibit expected SNR patterns across elevation angles, with generally higher SNR at higher elevations on DOY 223, 2024. 98

Figure 4.11: ENU position error comparison between CNES and SPARTN corrections using low-cost GNSS hardware on DOY 223, 2024.on DOY 223, 2024..... 101

Figure 4.12: Horizontal and vertical positioning error comparison between CNES and SPARTN corrections using low-cost GNSS hardware on DOY 223, 2024. 102

Figure 4.13: JPL-managed ASH701945E_M antenna with radome at the QUIN IGS station, supporting geodetic and atmospheric monitoring (Adapted from International

GNSS Service, 2024). 104

Figure 4.14: Comparison of east, north, and up coordinate errors at the QUIN reference station on DOY 222, 2024, using CNES (blue) and SPARTN (red) corrections. 106

Figure 4.15: Comparison of horizontal and vertical positioning errors at the QUIN reference station on DOY 222, 2024, using CNES (blue) and SPARTN (red) corrections. 108

Figure 4.16: Signal-to-noise ratio (SNR) and satellite elevation angles observed at the QUIN IGS station on DOY 222, 2024, during a 24-hour static test. 109

Figure 4.17: Elevation plot showing satellite exclusion due to SPARTN correction unavailability at the QUIN IGS station on DOY 222, 2024. 111

Figure 4.18: Estimated multipath error for GNSS observations at the QUIN IGS station on DOY 222, 2024, during a 24-hour static test. 112

Figure 4.19: Residuals of L1/E1 pseudorange (left) and carrier-phase (right) measurements at the QUIN IGS station on DOY 222, 2024, during a 24-hour static test. 114

Figure 4.20: Signal-to-noise ratio (SNR) versus elevation angle at the QUIN IGS station on DOY 222, 2024, for L1/E1/B1 frequencies. 116

Figure 4.21: Signal-to-noise ratio (SNR) versus elevation angle at the QUIN IGS station on DOY 222, 2024, for L2/E5b/B2 frequencies. 117

Figure 4.22: Number of valid satellites used in CNES (blue) and SPARTN (red) solutions during static testing at the QUIN IGS station on DOY 222, 2024. 119

Figure 4.23: Position errors of the SPARTN solution relative to the reference trajectory during the kinematic GNSS test on DOY 221, 2024. RMS errors and the 0.5 m threshold are shown for the east, north, and up components. 121

Figure 4.24: Position errors of CNES solution relative to the reference trajectory during the kinematic GNSS test on DOY 221, 2024. RMS errors and the 0.5 m threshold are shown for the east, north, and up components. 122

Figure 5.1: ENU errors (float versus fixed solutions) using YorkPPP with CNES corrections from the rooftop experiment at York University on DOY 223, 2024. 126

Figure 5.2: Horizontal and vertical positioning performance of float and fixed solutions using YorkPPP with CNES corrections, including satellite count and PDOP variation from the rooftop experiment at York University on DOY 223, 2024. 128

Figure 5.3: Pseudorange and carrier-phase residuals for L1/E1 and L2/E5b signals using CNES corrections in YorkPPP from the rooftop experiment at York University on DOY 223, 2024..... 129

Figure 5.4: ENU errors (float versus fixed solutions) using YorkPPP with SPARTN corrections in YorkPPP from the rooftop experiment at York University DOY 223, 2024. 130

Figure 5.5: Horizontal and vertical positioning performance of float and fixed solutions using YorkPPP with SPARTN corrections, including satellite count and PDOP variation from the rooftop experiment at York University on DOY 223, 2024. 132

Figure 5.6: Pseudorange and carrier-phase residuals of the rooftop station for L1/E1 and L2/E5b signals using SPARTN corrections in YorkPPP from the rooftop experiment at

York University on DOY 223, 2024. 134

Figure 5.7: ENU errors (float versus fixed solutions) using YorkPPP with CNES corrections in YorkPPP from the rooftop experiment using low-cost hardware at York University on DOY 223, 2024. 138

Figure 5.8: Horizontal and vertical positioning performance of float and fixed solutions using YorkPPP with SPARTN corrections, including satellite count and PDOP variation from the rooftop experiment at York University using low-cost hardware on DOY 239, 2024 139

Figure 5.9: ENU errors (float versus fixed solutions) using YorkPPP with SPARTN corrections in YorkPPP from the rooftop experiment using low-cost hardware at York University on DOY 223, 2024. 141

Figure 5.10: Horizontal and vertical performance of float and fixed solutions using YorkPPP with CNES corrections, including satellite count and PDOP variation from the rooftop experiment using low-cost hardware on DOY 239, 2024. 143

Figure 5.11: SPARTN orbit and clock correction errors on DOY 222, 2024: radial, along-track, and cross-track orbit correction components, along with total clock correction error across all satellites 145

Figure 5.12: SPARTN correction biases for code (P1, P2) and carrier-phase (L1, L2) signals on DOY 222, 2024. 146

Figure 5.13: SPARTN orbit, clock, and signal bias errors versus elevation angle at the QUIN IGS station on DOY 222, 2024. 147

Figure 5.14: Time series of SPARTN ionospheric and tropospheric correction errors

across satellites on DOY 222, 2024. 148

Figure 5.15: Time series of pseudorange and carrier-phase residuals for L1/E1 and L2/E5b signals after applying SPARTN corrections on DOY 222, 2024. 149

Figure 5.16: Time series of east, north, and up (ENU) positioning errors for float and fixed solutions with SPARTN corrections applied on DOY 222, 2024. 150

Figure 5.17: Horizontal and vertical positioning errors, satellite visibility, PDOP, and convergence metrics at the QUIN IGS station on DOY 222, 2024, using SPARTN corrections for float and fixed solutions. 151

Figure 5.18: Percentage of satellite observations by elevation angle and constellation at QUIN station. 153

Figure 5.19: Horizontal and vertical positioning errors, satellite visibility, PDOP, and convergence metrics at the QUIN IGS station on DOY 222, 2024, using CNES corrections for float and fixed solutions. 154

Figure 5.20: Horizontal and vertical positioning error convergence by GNSS constellation (GPS, GLONASS, Galileo, and BeiDou) at the QUIN IGS station on DOY 222, 2024, using SPARTN corrections and comparing float and fixed solutions. 156

Figure 5.21: Time series of ENU and horizontal/vertical positioning errors on DOY 221, 2024, using CNES corrections in YorkPPP and referenced to the ground-truth trajectory. 163

Figure 5.22: Time series of ENU and horizontal/vertical positioning errors on DOY 221, 2024, using SPARTN corrections in YorkPPP and referenced to the ground-truth trajectory. 165

List of Acronyms

ANTEX	Antenna Exchange Format
APC	Antenna Phase Centre
AR	Ambiguity Resolution
ARP	Antenna Reference Point
BDT	BeiDou Time
BeiDou	China's Satellite System
C/A code	Coarse/Acquisition Code
C/N_0	Carrier-to-Noise Density Ratio
CDMA	Code Division Multiple Access
CGCS2000	China Geodetic Coordinate System 2000
CNES	Centre National d'Études Spatiales
CORS	Continuous Operating Reference Station
DCB	Differential Code Bias
DCM	Decoupled Clock Model
DGNSS	Differential GNSS
DOP	Dilution of Precision
DOY	Day of Year
ECEF	Earth-Centred, Earth-Fixed
EKF	Extended Kalman Filter
FCB	Fractional Cycle Bias
GEO	Geostationary Earth Orbit

GIOVE	Galileo In-Orbit Validation Element
GLONASS	Globalnaya Navigatsionnaya Sputnikovaya Sistema
GNSS	Global Navigation Satellite System
GPS	Global Positioning System
GTRF	Galileo Terrestrial Reference Frame
GUI	Graphical User Interface
Galileo	European Satellite Navigation System
IGS	International GNSS Service
IGSO	Inclined Geosynchronous Orbit
IMU	Inertial Measurement Unit
IRC	Integer Recovery Clocks
IS-GPS	Interface Specification for GPS
ISGO	Inclined Synchronous Geostationary Orbit
ITRF	International Terrestrial Reference Frame
IoT	Internet of Things
LAMBDA	Least-squares AMBiguity Decorrelation Adjustment
MBOC	Multiplexed Binary Offset Carrier
MEO	Medium Earth Orbit
MLAMBDA	Modified LAMBDA
NAV	Navigation Message
NRTK	Network Real-Time Kinematic
OCB	Orbit Clock Bias
P(Y)-code	Encrypted Precision code

PDOP	Position Dilution of Precision
PNT	Positioning, Navigation, and Timing
PPP	Precise Point Positioning
PPP-AR	PPP with Ambiguity Resolution
PRN	Pseudo Random Noise
RAIM	Receiver Autonomous Integrity Monitoring
RDSS	Radio Determination Satellite Service
RINEX	Receiver Independent Exchange Format
RMS	Root Mean Square
RTCM	Radio Technical Commission for Maritime Services
RTK	Real-Time Kinematic
SAR	Search and rescue
SBAS	Satellite-Based Augmentation System
SNR	Signal-to-Noise Ratio
SPARTN	Secure Position Augmentation for Real-Time Navigation
SPP	Single Point Positioning
SSR	State Space Representation
TAI	International Atomic Time
TEC	Total Electron Content
TGD	Total Group Delay
UTC	Coordinated Universal Time
ZTD	Zenith Total Delay
PPM	Parts Per Million

1. Introduction

Positioning technology has experienced enormous evolution in the decades since the Global Positioning System was first introduced to the world (Heo & Yan, 2009). The development of positioning technology has changed the way many industries have approached Positioning, Navigation, and Timing (PNT) solution (Hirokawa & Fernández-Hernández, 2020). As a global economy becomes increasingly dependent on positioning with precision solution, the need for increased accuracy of PNT applications has grown exponentially fuelling technological innovation in Global Navigation Satellite Systems.

The requirement for accurate position at the centimetre level in various applications such as autonomous vehicles, precision agriculture, geodetic surveying and emergency services continues to grow (Ferguson et al., 2020). While standard GPS provides sufficient accuracy for general navigation, the requirements for global signal redundancy and improved satellite geometry drove the development of multiple GNSS constellations. However, to compensate atmospheric delays and orbital errors found in standalone positioning, augmentation services are available to provide the necessary corrections for cm-level accurate positioning (Hofmann-Wellenhof et al., 2007). Global Navigation Satellite Systems (GNSS) such as the Global Positioning System (GPS), Global Navigation Satellite System (GLONASS), Galileo, BeiDou Navigation Satellite System (BDS) and many regional and local systems complement the stand-alone solution to significantly improve the position results. This multi-constellation framework increases satellite availability and improves geometric strength, which directly contributes to higher positioning accuracy and system reliability across diverse applications (Naciri et al., 2023).

There has been an increasing interest in high-accuracy GNSS correction augmentation technologies that preserve fundamental positioning principles while offering global accessibility and interoperability (Vana et al., 2019). These advanced systems utilise State Space Representation (SSR), which marks a technical shift from traditional Observation Space Representation (OSR). While OSR techniques, such as conventional RTK, provide a "lumped" sum of errors specific to a single reference station, state-space representation (SSR) decomposes the GNSS error budget into individual physical components, including precise satellite orbits, clock offsets, and signal biases (Hirokawa and Fernández-Hernández, 2021). This state-space approach allows corrections to be broadcast as a single global or regional data stream to an unlimited number of users, significantly reducing bandwidth requirements and enabling high-precision positioning without the need for a nearby physical base station (Wübbena et al., 2005).

The integration of modern GNSS corrections into open-source processing engines represents a critical convergence of state-of-the-art error-correction methodologies with accessible software platforms. The high-precision positioning market is often a “black-box”, dominated by proprietary correction data formats, closed-source hardware, complex software solutions and a general lack of transparency in positioning algorithms, particularly ambiguity resolution and atmospheric modelling (Odolinski and Teunissen, 2017). To encourage both academic and commercial innovation in positioning technology, the barriers to entry into the current closed ecosystem need to be broken by introducing open-source alternatives that are interoperable with the existing system. Using correction data and integrating with existing hardware and software, the open-source solution RTKLIB has been utilised to develop a high-precision, standalone positioning system.

SPARTN is a new open, royalty-free format for delivering GNSS corrections developed by u-blox for today's positioning needs which enables higher industry interoperability and transparency (u-blox AG, 2021). The format optimises bandwidth efficiency and integrates essential security features including integrity-monitoring capabilities, which makes it uniquely suited for safety-critical applications (Ferguson et al., 2020). This open-access approach addresses the growing demand for scalable and secure correction delivery across various hardware platforms (Vana et al., 2019).

The widely used GNSS processing platforms RTKLib and university developed YorkPPP lack native support for the SPARTN format. The open-source GNSS data processing engine RTKLib developed by Tomoji Takasu, has gained industry-wide recognition as the reference for GNSS data processing (Takasu, 2013). YorkPPP, a research-grade platform developed at the York University GNSS Laboratory, provides advanced Precise Point Positioning (PPP) capabilities, including Ambiguity Resolution (PPP-AR) functions. While both platforms support a wide range of positioning methods from Single Point Positioning to RTK and PPP, neither currently possesses the compatibility to ingest and decode SPARTN corrections, a gap which this research aims to resolve.

1.1 Problem Statement

The GNSS positioning of today encounters multiple complex issues that strongly affect operational efficiency and performance, together with accessibility of high precision correction services. Multiple obstacles emerge from these challenges, which prevent the widespread implementation of centimetre- level positioning accuracy throughout different application fields like autonomous cars, precision agriculture and IoT.

The primary challenges forming this problem statement are summarized below:

1. Proprietary Barriers and the "Black-Box" Paradigm: High-precision positioning has historically been dominated by proprietary, closed-source formats and hardware-locked ecosystems. This creates a "black-box" environment where researchers cannot inspect or verify the underlying algorithms, stifling academic innovation and forcing a costly dependency on specific vendors (Odolinski & Teunissen, 2017).
2. Lack of Open-Source Support for SSR Corrections: While State Space Representation (SSR) is the modern standard for scalable, global corrections, popular open-source engines like RTKLib and research platforms like YorkPPP lack native support for emerging SSR-based protocols such as SPARTN. Since there are no built-in decoders for these formats in open-source tools, advanced positioning capabilities are not accessible to the community (Hirokawa and Fernández-Hernández, 2020; Takasu, 2013).
3. Bandwidth and Scalability: Whilst traditional RTK and Observation Space Representation (OSR) methods have high bandwidth requirements and are not globally scalable, recent developments aim to address these limitations. Formats like SPARTN reduce bandwidth requirements by up to 50% yet lack integration in routine processing tools on small bandwidth connections to test and implement on (Vana et al., 2019; Ferguson et al., 2020).
4. Performance Trade-offs and Validation Uncertainty: Most current navigation systems make an unavoidable compromise between local RTK positioning with baselines on the order of 10 to 20 km on one hand, and the global coverage of PPP solutions with typical convergence times of 15 to 30 minutes on the other hand. Furthermore, the

absence of standardized validation frameworks for new formats like SPARTN creates uncertainty regarding their reliability across different operational environments (Hofmann-Wellenhof et al., 2007; Kim et al., 2021).

1.2 Thesis Statement and Objectives

The main purpose of this research is to develop multi-frequency, multi-constellation Precise Point Positioning (PPP) and Ambiguity Resolution (PPP-AR) by integrating SPARTN corrections into the open-source platform RTKLib and the research-grade software YorkPPP, developed at York University. The proposed integration aims to achieve centimetre-level positioning accuracy while significantly improving bandwidth efficiency and convergence performance. Instead of relying solely on proprietary solutions that restrict innovation and over-pricing closed-source commercial processing chains, this work provides a cost-effective framework for efficiently interoperating proprietary State Space Representation (SSR) signals with open-source signal processing architectures.

To achieve this goal, the thesis follows three primary objectives:

1. Develop and implement a standardized SPARTN decoding and integration module for the RTKLIB and YorkPPP software platforms. This provides the open-source community with the necessary tools to ingest next-generation state-space representation (SSR) corrections for both traditional PPP and advanced PPP-AR applications.
2. Evaluate the performance of SPARTN-enhanced positioning solutions across diverse operational scenarios. This includes a rigorous benchmarking of positioning accuracy, convergence latency, and solution stability against established correction standards, such as CNES real-time streams and IGS ultra-rapid products.

3. Establish a validated framework and implementation guidelines for using SPARTN corrections in open-source software and provide best practices for utilising modern state-space representation (SSR) corrections into existing processing workflows, fostering broader adoption and interoperability.

This research addresses critical interoperability barriers between proprietary formats and open-access software. By delivering a functional, public implementation of the SPARTN protocol, this work facilitates major performance gains in PPP and PPP-AR systems, accelerating the transition of high-precision GNSS capabilities into mass-market, academic, and commercial research applications.

1.3 Research Novelty and Significance

The novelty and significance of this research are defined by the following key contributions to the field of Global Navigation Satellite Systems:

1. First Open-Source Integration of SPARTN for PPP-AR: This study presents the first complete integration of the SPARTN protocol into both the industry-standard RTKLib (Takasu, 2013) and the research-grade YorkPPP platform. Unlike previous studies that focused on proprietary automotive implementations (Ferguson et al., 2020), this work bridges the gap between mass-market state space representation (SSR) corrections and processing platform like RTKLib and YorkPPP which supports ambiguity resolution (PPP-AR) methodologies.

2. Dual-Architecture Decoding Framework: A significant technical contribution of this research is the development of a modular decoding and translation framework. This system aligns the bit-level SPARTN specifications (u-blox AG, 2021) with the distinct processing structures of RTKLib and the sophisticated filtering requirements of

YorkPPP. This architecture serves as a scalable template for integrating future state-space representation (SSR) based formats into various GNSS software (Hirokawa and Fernández-Hernández, 2021).

3. Component-Level Sensitivity Analysis: This research advances the theoretical understanding of SSR corrections by conducting a granular assessment of individual correction elements, including precise orbits, clocks, code and phase biases and atmospheric correction. By isolating these components, the study provides new empirical evidence on their specific impacts on convergence latency and ambiguity fix success rates, extending the fundamental frameworks established by Collins et al. (2010) and Kim et al. (2021).

4. Unified Benchmarking Methodology: The study introduces an original validation platform that enables a direct "head-to-head" comparison between CNES/IGS products and SPARTN streams under identical hardware and environmental conditions. This addresses a critical void in GNSS literature where performance evaluations are often incomparable due to varying test environments (Odolinski and Teunissen, 2017).

5. Democratization of High-Precision PNT: Scientifically, this work removes the "black-box" barrier associated with commercial high-precision services. By making SPARTN compatible PPP-AR accessible via open-source tools, this research empowers academic institutions and independent researchers to conduct advanced GNSS studies without the prohibitive costs of proprietary subscriptions, fostering industry-wide interoperability (Vana et al., 2019).

1.4 Thesis Structure and Organizational Framework

This thesis is organised into six chapters, providing systematic progression from theoretical foundations to the technical implementation and empirical validation of SPARTN corrections.

Chapter 1: Introduction presents research motivation, problem statement, and specific objectives, highlighting the gap in open-source support for modern state-space representation (SSR) correction formats.

Chapter 2: GNSS Fundamentals: Signal Structures, Errors, and Positioning Techniques examine the evolution of GNSS positioning, from SPP and RTK to advanced PPP and PPP-AR. This chapter establishes the mathematical basis for error modelling, atmospheric delays, and integer ambiguity resolution, while situating RTKLIB and YorkPPP within the current software landscape.

Chapter 3: The SPARTN Protocol and Corrections Framework and Implementation provides a technical dissection of the SPARTN protocol, including message structures and implementation requirements. It details the architectural modifications required to integrate these corrections into both RTKLIB and YorkPPP, focusing on data flow design and processing sequence alignment.

Chapter 4: Experiments and Analysis from RTKLib describes the experimental validation of SPARTN within the RTKLib environment. This chapter focuses on traditional PPP processing in static and kinematic modes, benchmarking positioning accuracy and convergence latency against established CNES and IGS products.

Chapter 5: Experiments and Analysis from YorkPPP focus on the high-precision

capabilities of the YorkPPP platform. It evaluates the impact of SPARTN corrections on Integer Ambiguity Resolution (AR) success rates, time-to-first fix (TTFF) metrics, and solution stability in complex operational scenarios.

Chapter 6: Conclusions and Recommendation summarize the research findings regarding SPARTN's efficiency and interoperability. This chapter discusses the practical implications for the GNSS community, provides operational guidelines for open-source state-space representation (SSR) integration, and identifies future research trajectories for next-generation positioning formats.

2. GNSS Fundamentals: Signal Structures, Errors, and Positioning Techniques

This chapter presents a brief overview of core GNSS principles, the identification and explanation of important error sources that affect positioning accuracy and positioning modes. The RTKLib and YorkPPP software are given a particular focus and importance throughout the thesis since they are vital analytical tools from the beginning to the end. This chapter provides precise information regarding the hardware platforms and software implementations that were utilised throughout this research. The theoretical framework presented in this chapter provides conceptual support for the experimental design, data collection processes, and analytical methodologies that are covered in later chapters.

2.1 Fundamental Concepts in Modern Satellite Navigation and Augmentation Systems

A Global Navigation Satellite Systems offers worldwide, continuous, and all-weather three-dimensional positioning, navigation, and timing information (PNT). Modern GNSS architecture are described by a so-called tri-architectures consisting of a Space Segment (Satellites), a Control Segment (ground stations) and a User Segment (receivers, software). (Hofmann-Wellenhof et al., 2007).

The GNSS positioning is based on the principle trilateration, where the simultaneous measurement of distances between a receiver and multiple satellites with known orbital positions are measured. Because receiver clocks are typically not synchronised with the highly stable atomic clocks on board the satellites, receivers must solve four unknowns: the three spatial coordinates (X, Y, Z) and the receiver clock offset. Thus, minimum four

satellites are required to compute a 3D position solution (Misra and Enge, 2011).

Since the operational maturity of the United States' Global Positioning System (GPS), GNSS technology has experienced a dramatic shift from a purely military application to a fundamental global infrastructure. There is a rapidly increasing variety of high-precision applications such as geodesy, precision agriculture, road surveying, autonomous traffic systems and telecommunications (Seeber, 2003). Many of these applications require precise time information and accurate positions. As global economies increasingly depend on high accuracy data, the technology is continuously improving towards a multi-constellation approach and higher quality error mitigation techniques to reduce effects of atmospheric and orbital errors (Montenbruck et al., 2017).

2.2 GNSS Signal Architecture and Modernization

Modern GNSS signal design has evolved far beyond legacy signals and moves step by step from single frequency carrier through multi-frequency to mitigate range error caused by atmosphere and to combat signal corruption by interference. While transmissions primarily utilised constant amplitude Binary Phase Shift Keying (BPSK), higher spectral efficiency and better immunity against multipath were the reason for introducing recent modern signals with Binary Offset Carrier (BOC) modulation to satisfy higher requirements for accuracy (Betz, 2015). Figure 2.1 illustrates modulation scheme of GNSS signals, on example of signals which are in use presently, where radio carrier is modulated by navigation data and with code for measuring of distance to satellite. The GNSS signal transmitted by a satellite is often termed as the combined signal. The modulation of the combined signal onto the high-frequency L-band carrier is used for transmission. The first step in the modulation process is the application of a PRN ranging code (also referred to as

a code) to the carrier wave. This code enables the receiver to calculate the travel time of the signal and thus to determine the distance of the receiver from the satellite. A unique pseudo-random noise (PRN) ranging code is then applied to the carrier to enable receiver-based travel time estimation and satellite identification. The navigation message, which carries information on the ephemeris of a satellite, clock corrections as well as information on the satellite's health, is combined with the PRN code prior to the carrier modulation. The combined signal is then modulated onto the carrier using Binary Phase Shift Keying (BPSK). The unique PRN codes enable several satellites to transmit at the same time on the same frequency using a technique called code-division multiple access (CDMA) (Hofmann-Wellenhof et al., 2008).

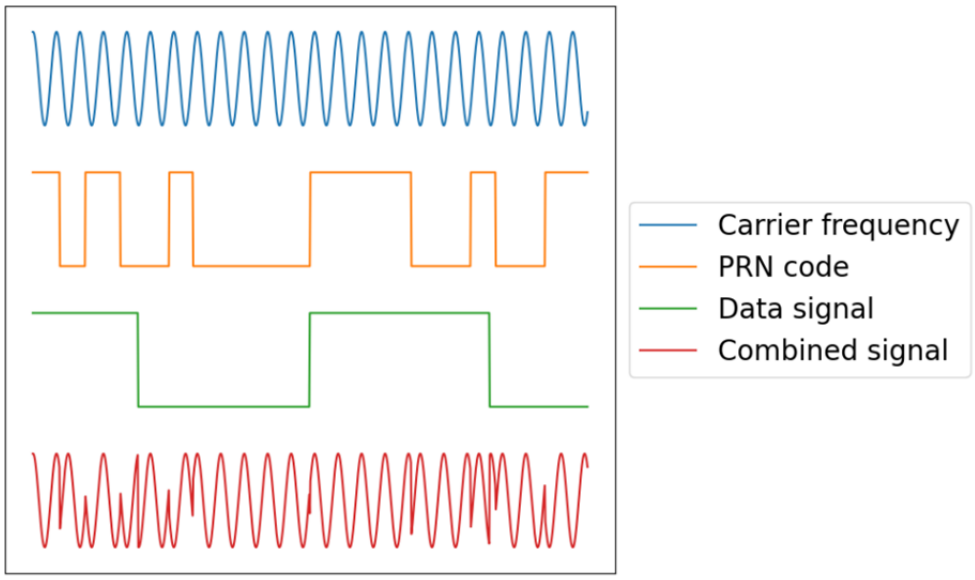


Figure 2.1: Illustration of GNSS signal modulation process (Adapted from Misra and Enge, 2011).

With the modernisation of existing and new constellation systems (such as GPS, Galileo and BeiDou), there is a strategy for frequency re-use between these different

constellations. By adopting the same signal structure on different carrier frequencies, chip rate and bandwidth manufacturers can develop more efficient multi-constellation receivers. Signal presence and geometry (DOP) is dramatically improved for users of modern mass market receivers that can now see signal from this frequency aligned constellations. Frequencies are reused for these next-generation systems include the L-band spectrum, specifically the L1/E1/B1C signals at 1575.42 MHz and the L5/E5a/B2a signals at 1176.45 MHz (Kaplan & Hegarty, 2017).

Positioning accuracy is only one of several criteria which need to be optimised for a signal portfolio. There is also the issue of Signal Integrity, which is gaining importance, and Signal Security, for which a number of techniques have been developed, some of which are already implemented in the GNSS constellations. The increasing reliance on GNSS for critical applications, such as timing dissemination for infrastructure synchronisation, also necessitates the implementation of authentication mechanisms. Galileo's Open Service Navigation Message Authentication (OSNMA) is a currently available example, which provides a method to authenticate the navigation message to mitigate the risk of parametric spoofing and interference (Teunissen and Montenbruck, 2017).

2.3 Comparative Analysis of GNSS Constellations

The operational performance of high-precision positioning is mainly determined by the system architecture of the corresponding satellite constellations in space. Table 2.1 outlines the main characteristics of current GNSS systems, including GPS, GLONASS, Galileo and BeiDou. The term ‘accuracy’ refers to the degree with which the receiver’s position determined by the system corresponds to the real position of the receiver. The transmission of the signals and their multiplexing are different for the respective systems. While GPS

and Galileo utilise the Code Division Multiple Access (CDMA) method for transmitting signals, all on the same frequency, and are thus separated by different PRN codes (Pseudo-Random Noise codes), GLONASS makes use of the traditional Frequency Division Multiple Access (FDMA) method. Here, each satellite transmits on a different carrier frequency within a frequency band assigned for this purpose. Observations using several frequencies are essential for a correct determination of the delay that is caused by the ionosphere and for highly precise applications, such as the carrier-phase tracking or the Precise Point Positioning (PPP).

Table 2.1: Comparative overview of GNSS constellations (Adopted from Montenbruck et al., 2017).

System	Owner	Coding	Orbit Height	Period	Number of Satellites	Accuracy	Frequency (RINEX Notation)
BeiDou	China	CDMA	21,150 km (MEO), 35,786 km	12 h 38 m (MEO), 23 h 56 m	24 (MEO), 3 (ISGO), 3 (GEO)	10 m	L1, L2, L6, L7
Galileo	EU	CDMA	23,222 km	14 h 5 m	24	1 - 5 m	L1, L5, L6, L7, L8
GLONASS	USSR	FDMA (CDMA)	19,130 km	11 h 16 m	24	5 - 10 m	L1, L2, (L5)
GPS	US	CDMA	20,180 km	11 h 58 m	31	3.5 - 7.8 m	L1, L2, L5

The most critical information in Table 2.1 is the frequency diversity and multi-constellation signal harmonization, which serve as the foundation for modern high-precision positioning. By providing multiple frequency signals (e.g. L1, L2, L5), current positioning constellations provide the necessary foundations for deriving the ionosphere-

free linear combinations, which are widely used in GNSS processing software. In addition, the signals from all three positioning systems (GPS, Galileo, BeiDou) operate using a unified CDMA signal architecture which allows for friendly interoperability, i.e. a single receiver can track more than 100 satellites at once. From a geometric standpoint, this greatly increases signal availability and resulting DOP strengths, often resulting in robust position fixes when single constellation GPS signals are at or near geometric limit (Montenbruck et al., 2017).

2.3.1 The Global Positioning System (GPS)

The Global Positioning System (GPS) operated by the United States Space Force depicts a baseline constellation of 31 satellites orbiting the Earth on six unique planes with a 55° east/west inclination. The satellites are arranged in Medium Earth Orbit at a nominal altitude of 20,200 kilometres. Prior to the GPS III modernization initiative, the legacy GPS signal provided to civil users consisted of L1 C/A code, while military users were able to access L1 P(Y) code as well as L2 P(Y) code. The new GPS signal architecture for civilian users provides L2C, L5, and L1C signals in addition to the previously mentioned L1 C/A code signal. The modern GPS signals include advanced Binary Offset Carrier (BOC) modulation, which offer much improved signal code-tracking, multipath mitigation, and cross-correlation characteristics when compared with legacy BPSK-modulated signals (Kaplan and Hegarty, 2017).

Precision system time and orbit are provided by the Control Segment through accurate ephemeris and clock determination disseminated via monitor station telemetries received at the Master Control Station, with determination performed using an extended Kalman filter (Misra and Enge, 2011). Managing this data are substantial monitor station and

Master Control Station resources, in contrast to Tracking Stations. The transition to packetized modernized data messages has improved navigation message robusticity, reduced Time-to-First Fix, and provided greater atmospheric parameters. Such enhancements in signal robusticity and message flexibility are essential prerequisites for the integration of State Space Representation (SSR) formats like SPARTN, which demand high-integrity, low-latency satellite data to achieve stable centimetre-level positioning (Montenbruck et al., 2017).

2.3.2 GLONASS (Russian Federation)

Russian Federation operates the GLONASS, which comprises 24 Medium Earth Orbit (MEO) satellites in three separate orbital planes, positioned at approximately 19 100 km altitude with an orbital inclination of 64.8°. The higher orbital altitude and orbital inclination of GLONASS satellites above the equator afford excellent ground visibility, especially towards high latitudes relative to other global constellations (Hofmann-Wellenhof et al. 2007). Historically FDMA has been used for distribution of RF signal frequency for GLONASS space vehicles, with each individual satellite allocated a distinct centre frequency for signal transmission. This signal distribution methodology, whilst robust, introduces so-called Inter-Frequency Biases (IFBs) that must be treated within high-precision positioning processing engines, such as those supported by software utilities like RTKLIB and YorkPPP (Misra and Enge 2011).

With the GLONASS-K and K2 satellites new generation of Russian space-based navigation system is modernising its signal structure and transitioning from Hyper-Pulse Positioning Modulation to Code Division Multiple Access (CDMA) compatible with GPS and Galileo. Also, the new generation of Russian navigation system is approaching the

transition to the PZ-90 terrestrial reference frame, which opens the opportunity for integration into a multi constellation SSR approach like in SPARTN (Montenbruck et al., 2017). By enhancing satellite availability and geometric strength (DOP), GLONASS remains an essential component for achieving stable, global centimetre-level positioning (Kaplan and Hegarty, 2017).

2.3.3 Galileo (European Union)

Galileo is the European Union's independent space-based navigation system developed for civilian use and to complement the US GPS for commercial use. The space component is composed of a nominal constellation of 24 operational satellites, distributed across three circular orbits, placed at a nominal altitude of 23,222 km with an inclination of 56°. Unlike legacy systems, Galileo is designed to be interoperable with GPS, and the Galileo Terrestrial Reference Frame (GTRF) is utilised for time and reference purposes. The GTRF is aligned with the International Terrestrial Reference Frame ITRF used by global state-space representation (SSR) correction services like SPARTN (Montenbruck et al., 2017).

Galileo space-based navigation system offers several technical advantages based on its signals spread across several frequency bands: E1 (1575,42 MHz), E5 (Historic (1197,42 MHz), AltBOC (1206,15 MHz), E6 (1278,75 MHz). Modulation scheme applied in E1 band offers lower noise and multipath effects, whereas in E5 band Alternative Binary Offset Carrier (AltBOC) ensures lower code noise and higher multipath rejection. In addition, Galileo's High Accuracy Service (HAS) and Open Service Navigation Message Authentication (OSNMA) offer highest signal integrity and built-in precise positioning. Because PHM clocks onboard Galileo satellites are extremely stable, Galileo represents one of fundamental parts of positioning systems that enable fast positioning based on PPP-

AR methodology (Misra and Enge, 2011).

2.3.4 BeiDou Navigation Satellite System (BDS)

The third generation of the BeiDou Navigation Satellite System (BDS-3) provided by the People's Republic of China is operating globally with a hybrid orbit constellation of satellites. The BDS-3 constellation consists of 30 satellites in orbit: 24 Medium Earth Orbit (MEO), 3 Geostationary Orbit (GEO), and 3 Inclined Geosynchronous Orbit (IGSO) satellites. With this constellation, BeiDou has excellent satellite visibility as well as good geometric configurations (DOP values) in Asia-Pacific and around the globe. In addition, BeiDou uses its own coordinate reference system called BeiDou Coordinate System (BDCS) for positioning and time determination and has very good interoperability to the China Geodetic Coordinate System 2000 (CGCS2000) and maintains high interoperability with the ITRF standard used in global state-space representation (SSR) correction services (Montenbruck et al., 2017).

From a signal processing perspective, BDS-3 introduced new signals: B1C, B2a, and B2b, which are frequency compatible with GPS L1/L5 and Galileo E1/E5a. The new signals are modulated with QMBOC (Quadrature Multiplexed Binary Offset Carrier) signals, which improves code-tracking performances with higher signal to noise ratio compared with legacy GPS/Galileo signals. (Kaplan and Hegarty, 2017). Also, Satellite-Based Augmentation (SBAS) and PPP services are embedded into the constellation broadcast. With the aid of high-stability clock, hydrogen maser and rubidium, BDS signals can be utilised to achieve rapid ambiguity resolution to reach high-precision positioning in multi-constellation architecture like open source RTKLIB software and research software YorkPPP (Misra and Enge, 2011).

2.4 GNSS Error Sources and Mitigation Strategies

Achieving centimetre-level accuracy in Precise Point Positioning (PPP) and RTK requires the rigorous modelling or systematic elimination of multiple error sources. These biases are generally categorized into satellite-specific, atmospheric, and receiver-specific effects (Hofmann-Wellenhof et al., 2008).

Errors in GNSS positioning are defined as differences between observed values or calculated positions and their true values. There are two types of errors: systematic errors which can be modelled with math and then corrected with external streams of corrections, and random errors that are filtered using statistics. It is the aim of the Precise Point Positioning (PPP) to individually remove errors from the total error budget such as the satellite clock error, the satellite orbital error, and the atmospheric delay error. This decrease of the total error budget from the decimetre/metre-range to the centimetre-range is the goal of the PPP-method.

Unlike relative positioning, the standalone nature of PPP necessitates absolute correction methods. Certain factors, such as satellite antenna phase centre variations (PCV) and phase wind-up, are critical as they directly influence ambiguity resolution and convergence time. While deterministic models account for several of these discrepancies, others require empirical estimation or external State Space Representation (SSR) corrections, such as SPARTN. Figure 2.2 displays the components of a pseudorange measurement. The calculated distance of the pseudorange is the speed of light multiplied by the difference of the time t_R and the time t^S of receipt of the signal. This diagram shows the satellite at two points along its orbit of approximately 300 metres in total distance for the signal to travel to the receiver. Note that there are several errors that need to be corrected

to achieve precise positioning which include atmospheric delays as well as receiver/satellite clock offsets. The error in the position of the satellite is not shown as a vector but does affect the calculated coordinates of the satellite.

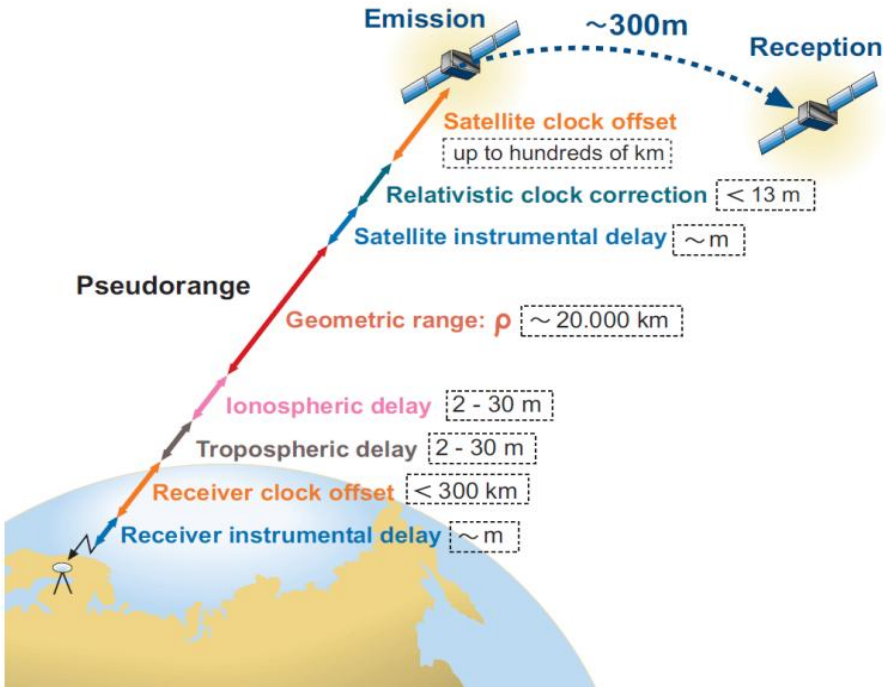


Figure 2.2: Components of the GNSS pseudorange measurement. The observed pseudorange is the summation of the geometric range and various satellite, receiver, and atmospheric error sources (Adapted from ESA, 2011).

2.4.1 Satellite Specific Errors

The following sections describe the various satellite-specific errors that affect GNSS positioning accuracy and overall system performance.

Relativistic Effects: GNSS satellites experience time dilation (due to high velocity) and gravitational frequency shifts (due to reduced gravitational potential). Without corrections, these would result in a clock drift of approximately 38μs per day. PPP and RTK engines apply relativistic correction terms based on the satellite's orbital eccentricity and velocity

(Ashby, 2003).

Satellite Clock Drift: Even atomic clocks exhibit small instabilities. The satellite clock error (*dt*) is modelled using a second-order polynomial:

$$dt = \alpha_o + \alpha_1(t - t_{oc}) + \alpha_2(t - t_{oc})^2 \quad (2.1)$$

The mathematical equation functions to calculate satellite clock error. The symbols α_o, α_1, and α_2 represent the clock offset from reference time, the clock drift rate, and half of the clock drift acceleration at the reference clock time t_{oc}, respectively (Bossler et al., 2002).

Ephemeris: Discrepancies between the predicted and actual satellite positions can lead to several metres of error in standard point positioning. High-precision applications utilise Precise Ephemerides (e.g., from IGS) to reduce this to the 1–5 cm level (Misra and Enge, 2011).

2.4.2 Atmospheric Propagation Errors

The following sections describe the various atmospheric propagation errors that affect GNSS positioning accuracy and overall system performance.

Ionospheric Refraction: The ionosphere (50–1000 km) is a dispersive medium that causes group delay in codes and phase advance in carrier waves. The delay is proportional to the Total Electron Content (TEC) and inversely proportional to the square of the frequency. The frequency dependence of the ionospheric effect can be described through the expression developed by Brunner and Welch (1993):

$$I = \frac{40.3}{c.f^2} .TEC \quad (2.2)$$

The quantity of free electrons per cubic metre is denoted by TEC, while the ionospheric

delay is represented by I, and the speed of light in metres per second is denoted by c and the frequency of the signal in hertz is denoted by f. Dual-frequency receivers substantially reduce ionospheric effects through their direct relationship with frequency. The receivers can effectively minimise ionospheric effects by a significant amount.

According to Klobuchar (1987) and Grewal et al. (2001), the Klobuchar model, which can partially simulate ionospheric effects for users of a single frequency, uses eight parameters which are transmitted in the navigation message. The model can perform this task because it uses the navigation message. The model generally achieves a delay correction rate of about fifty percent of the actual delay. Ionospheric corrections can be enhanced by calibrating TEC data, with notable approaches developed by Klobuchar and further refined by Ciraolo et al. (Klobuchar, 1987; Ciraolo et al., 2007).

Tropospheric Delay: Unlike the ionosphere, the troposphere (0–50 km) is non-dispersive. It consists of a Dry (Hydrostatic) component, representing 90% of the delay, and a Wet component, which is highly variable due to local humidity. Models such as Saastamoinen or Hopfield are typically used to estimate the zenith delay, which is then projected to the satellite's elevation using a mapping function (Saastamoinen, 1973).

2.4.3 Station and Receiver Specific Errors

The following sections describe the various receiver-specific errors that affect GNSS positioning accuracy and overall system performance.

Receiver Clock Error: The receiver clock offset (δt_r) arises by the lack of synchronisation of the receiver internal oscillator with the reference time of the GNSS signal. While satellites are equipped with atomic clocks of high stability, receiver clocks are normally composed of cost-effective Temperature-Compensated Crystal Oscillators (TCXO) with

typical drifts of about 1 ns every 10 s (Misra, 1996). In the standard navigation solution, this offset is treated as a stochastic parameter and estimated as the fourth unknown alongside the three-dimensional coordinates (X, Y, Z). This requires a minimum of four satellites for a closed mathematical solution (El-Rabbany, 2002). For high-precision applications, the resulting receiver noise, stemming from antenna design and tracking loops, is generally modelled as 1% of the carrier wavelength (Langley, 1997). Maintaining stable clock is essential to prevent cycle slips and preserve the integrity of the real-time ambiguity resolution process (Ward, 1994).

Multipath Effects: Multipath in GNSS occurs when part of the signal is reflected off a nearby surface such as a building or the ground before arriving at the antenna. For the code, this can easily amount to tens of metres but for the carrier phase the effect is more typically limited to a quarter of a wavelength, ~5 cm. Mitigation includes the use of choke-ring antennas and elevation masks (Raquet, 2002).

Antenna Phase Centre (PCO/PCV): The electrical Phase Centre of an antenna is not identical to its physical geometric centre and varies with the signal's angle of incidence. PPP requires ANTEX files to correct for Phase Centre Offsets (PCO) and Phase Centre Variations (PCV) for both the satellite and the receiver (Schmid et al., 2016).

Site Displacements: For centimetre-level consistency, the displacement of the station itself should be modelled, including the Solid Earth Tides (to ~30cm) due to the Moon and Sun, and the Ocean Tide Loading (to ~5cm) due to the mass of the tidal water distorting the crust. (Petit and Luzum, 2010; Bos et al., 2008).

Phase Wind-Up: This is a time dependent geometric error that occurs between the satellite antenna and the receiver antenna. As the receiver antenna rotates in a fixed mount, the

phase of the RHCP GNSS signals received changes. The phase wind-up error must be removed in order to obtain integer ambiguities for precision positioning (Wu et al., 1992).

Solid Earth Tides and Ocean Loading: In high-precision positioning the elastic deformation of the Earth's crust needs to be taken into account. Solid Earth Tides, caused by the gravitational pull of the Sun and Moon, result in periodic vertical movements of up to 30 cm and periodic horizontal movements in the order of several centimetres (Petit and Luzum, 2010). Modern GNSS algorithms implement standard IERS models to correct for these long-period and diurnal tidal components.

Additionally, Ocean Tide Loading represents the crustal deformation caused by the redistribution of oceanic mass. This site-specific effect is most pronounced in coastal regions, where displacements can reach several centimetres (Scherneck, 1991). Mitigation involves utilising global tide models, such as FES2014, to calculate time-dependent displacement corrections for the station coordinates (Bos et al., 2008).

Hardware Delays: Hardware delays result from electronic component imperfections during signal generation, modulation, and reception. Satellite-side biases are largely addressed via pre-launch calibration and the distribution of correction parameters, including Timing Group Delays (TGD), Differential Code Biases (DCB), and Observable-Specific Signal Biases (OSB) (Teunissen and Montenbruck, 2017).

At the receiver level, delays vary by model and tracking channel. While these effects are negligible in Single Point Positioning (SPP), they cause significant distortion in carrier-phase solutions. Achieving centimetre-level precision in PPP requires the rigorous modelling or estimation of these residual hardware biases to ensure signal integrity (Banville and Langley, 2012). Table 2.2 summarises the sources of GNSS measurement

errors, along with their typical magnitudes and corresponding mitigation strategies. It should be noted that the mitigation strategies and precise error models for the most common effects are summarized for Precise Point Positioning (PPP) only. Other relative positioning techniques, such as Real-Time Kinematic (RTK), also mitigate common-mode errors like satellite clock offsets, satellite orbital errors, and first order atmospheric delays by means of differencing between the base and the rover. However, for PPP type positioning, all individual physical effects are modelled mathematically in detail. High-precision PPP is performed by the YorkPPP engine, which, in the absence of a local reference station, still achieves a positioning accuracy in the centimetre range. Phase wind-up, relativistic effects, and solid Earth tides are some of the secondary effects that are considered in the modelling.

Table 2.2: Summary of GNSS measurement error sources, magnitude, and mitigation strategies (Adapted from Misra and Enge, 2011; Teunissen and Montenbruck, 2017).

Error Source	Magnitude Range	Mitigation Approach
Satellite Orbit Errors	1–10 cm (PPP), up to metres (SPP)	Precise ephemerides, real-time orbit corrections
Satellite Clock Errors	1–3 ns (~30 cm)	Precise clock products, satellite clock modelling
Relativistic Effects	~2.5 cm (orbit), ~2 ns (clock)	Relativistic correction equations
Ionospheric Delays	Up to tens of metres	Dual-frequency receivers, ionospheric models
Tropospheric Delays	Up to 2.5 m (zenith)	Tropospheric models, estimation in PPP
Satellite/Receiver Hardware Delays	Few cm to decimetres	Calibration, bias estimation
Satellite Antenna Phase Variations	Few mm to cm	Antenna phase centre correction (ANTEX)
Carrier-Phase Wind-Up	Up to a few decimetres	Polarization modelling and correction

Solid Earth Tides	Up to 30 cm	Tidal displacement models (IERS)
Ocean Loading	Up to 5 cm	Ocean tide loading models

2.5 GNSS Observation Models and Positioning Techniques

GNSS positioning is a Time-of-Arrival (TOA) ranging problem. By measuring the signal propagation delay between a satellite's transmission and the receiver's reception, a "pseudorange" is derived. To achieve centimetre-level accuracy, however, receivers must transition from coarse code-based tracking to high-precision carrier-phase measurements (Hofmann-Wellenhof et al., 2007).

2.5.1 Code Pseudorange Observation Model

The GNSS utilises signal processing of multiple satellite constellations currently orbiting the Earth to provide precise positioning of receivers on Earth. These satellite signals carry specific time and position information; using the signal time-of-arrival from multiple satellites before performing trilateration to determine a receiver's location, precise distance to satellites can be obtained.

The pseudorange measurement (P) is calculated using the speed of light (c) and the apparent signal propagation time (Δt), expressed as equation (2.3):

$$P = c.\Delta t = c\,.(t_R - t_S) \tag{2.3}$$

Where t_R is the reception time at the receiver and t_S is the transmission time by the satellite. The pseudorange (P) represents the geometric distance between the satellite and the receiver, biased by the lack of synchronisation between their respective atomic and quartz clocks. The observation model for a satellite (i) and receiver (r) is expressed according to Misra and Enge (2011) as shown in equation (2.4). While this model accounts

for the primary geometric and atmospheric delays, it is a simplified representation that does not explicitly include satellite and receiver hardware biases, which must be considered in high-precision PPP-AR applications.

$$P_r^i = \rho_r^i + c\,.\left(\delta t_r - \delta t^i\right) + I_r^i + T_r^i + M_{r,P}^i + \epsilon \tag{2.4}$$

Where ρ_r^i is the geometric distance, δt_r and δt^i are the receiver and satellite clock errors, I_r^i is the ionospheric delay, T_r^i is the tropospheric delay, $M_{r,P}^i$ is the multipath error, and ϵ represents receiver noise.

2.5.2 Carrier-phase Observation Model

Carrier-phase measurements make use of the high-frequency GNSS signal carrier wave to achieve higher positioning accuracy compared to measurements based on the lower frequency code pseudoranges. The primary carrier-phase observable is the measured signal phase difference in cycles between satellite and receiver at the instant of measurement. This phase observable consists of an integer number of wavelengths and a residual phase (in fractional cycle) of the carrier wave, which is referred to as the integer ambiguity (Teunissen and Montenbruck, 2017).

The range, R, derived from carrier-phase measurements, is modelled as shown in equation (2.5):

$$R = \lambda \cdot (N + \phi_{frac}) \tag{2.5}$$

where:

λ is the carrier wavelength

N is the integer ambiguity

ϕ_{frac} is the fractional part of the phase

The complete carrier-phase model for a signal from satellite *i* received by receiver *r* at time *t* is given by equation (2.6):

$$\phi_r^i = \frac{1}{\lambda}\left[\rho_r^i + c\,.\left(\delta t_r - \delta t^i\right) - I_r^i + T_r^i + \lambda N_r^i + M_{r,P}^i + \epsilon_\phi\right] \tag{2.6}$$

Here, λ is the carrier wavelength and N_r^i is the integer ambiguity, representing the unknown number of full carrier cycles between the satellite and receiver. Resolving this ambiguity is key to achieving centimetre-level accuracy.

2.5.3 Integer Ambiguity Resolution (AR)

In high-precision GNSS positioning, the terms “float” and “fixed” are used to describe the way in which carrier-phase ambiguities are estimated within the solution. A float solution is generated when all the carrier-phase ambiguous are estimated as a continuous real-value. They are not yet resolved to their correct integer value. The resulting position solution will have a high level of uncertainty that decreases as the filter processes more data and refines the values. A fixed solution is one in which all the carrier-phase ambiguous have been resolved to their correct integer value. Once the ambiguous have been resolved, the level of estimation uncertainty is significantly decreased which results in a solution that fixes very quickly and provides very stable position estimates. The solution typically has an accuracy of a few centimetres. The fixed solution is particularly good at fixing the vertical component that tends to wobble about in the float solution due to residual errors.

As the receiver only measures the fractional part of the carrier-phase, the primary challenge in carrier-phase positioning lies in resolving the integer ambiguity, Efficient resolution of this ambiguity requires both robust statistical algorithms and accurate bias

modelling. Various sophisticated algorithms, such as the Least Squares Ambiguity Decorrelation Adjustment (LAMBDA) method, have been developed to resolve this ambiguity using statistical techniques and data from multiple epochs and satellites (Teunissen and Kleusberg, 2012). The MLAMBDA method has also proven effective for rapid and reliable integer ambiguity resolution in high-precision applications (Chang et al., 2005). Critical to the success of these methods are improved fractional-cycle bias estimation techniques, which are crucial for resolving ambiguities efficiently in PPP (Geng et al., 2012). These technological advances have yielded significant practical improvements, with advanced ambiguity resolution techniques, including single-receiver phase ambiguity methods and the decoupled clock model, enabling near-instantaneous PPP convergence (Bertiger et al., 2010; Collins et al., 2008).

2.5.4 Single Point Positioning

The most basic GNSS positioning method exists as Single Point Positioning (SPP). The receiver functions independently to calculate its position using GNSS code-based pseudorange measurements from a minimum of four satellites, as shown in Figure 2.3. SPP operates with broadcast ephemerides and embedded clock corrections, which are received from satellite navigation messages. Due to its dependency on internal measurements, SPP achieves position accuracy at the metre level.

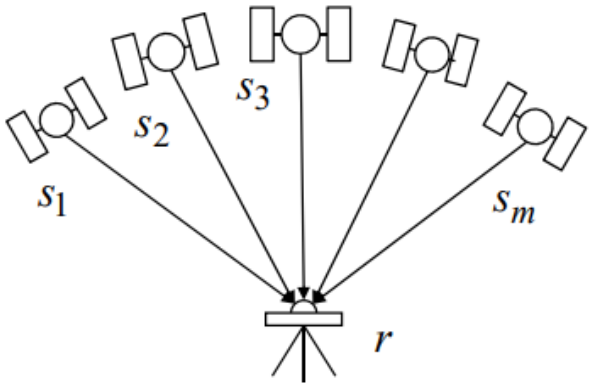


Figure 2.3: GNSS receiver tracking signals from multiple satellites for position determination (Adopted from Takasu 2013).

The observation model for SPP is primarily based on the pseudorange measurement equation:

$$P_r^s = \rho_r^s + c(\delta t_r - \delta t^s) + T_r^s + I_r^s + \varepsilon \qquad (2.7)$$

The observed pseudorange from satellite s to receiver r appears in the equation (2.7) as P_r^s, while ρ_r^s represents the actual satellite-receiver distance, and c represents the speed of light. The receiver clock error δt_r and satellite clock error δt^s are part of the equation along with true geometric distance ρ_r^s and tropospheric delay T_r^s and ionospheric delay I_r^s, and measurement noise ε. The system contains four unknowns that are the receiver coordinates (x, y, z) and the receiver clock offset. The method works globally, yet SPP lacks the accuracy needed for precision agriculture and surveying applications.

In Single Point Positioning (SPP) only single frequency observations are available, so the ionospheric delay is generally accounted for by using an empirical broadcast model. As SPP users cannot form an ionosphere-free combination as is done with dual frequency receivers, they rely on parameters transmitted within the satellite's navigation message that can be used to estimate the delay through a model. For GPS, the most common model used

is the Klobuchar model that uses broadcast coefficients to model the daily ionospheric delay. This model treats the ionosphere as a single thin shell at a fixed altitude and corrects for approximately 50% of the total ionospheric delay (Misra & Enge, 2011). While such a correction is generally sufficient for SPP applications targeting a decimetre to metre accuracy, higher accuracy techniques, such as Precise Point Positioning (PPP), utilise dual frequency measurements and/or external corrections such as State Space Representation (SSR) that are broadcast in the SPARTN protocol and offer centimetre accuracy.

2.5.5 Relative Positioning, Real-Time Kinematic (RTK) and Network RTK (NRTK)

The Relative Positioning system that offers users better GNSS positioning using a second receiver, simultaneously eliminating errors to boost accuracy. In Relative Positioning, a rover receiver determines its location while a fixed reference receiver is positioned at a known location and simultaneously receiving GNSS signals. The rover receives differential corrections through transmission after the base station compares its predicted pseudoranges to its measured pseudoranges. The rover gains satellite-related error compensation through this method, which includes orbit and clock inaccuracies as well as ionospheric and tropospheric delays and hardware biases. Figure 2.4 illustrates the geometry of two satellites, j and k, and two receivers, r (rover) and b (base). The carrier-phase measurements $\phi_r^j, \phi_b^j, \phi_r^k$anb ϕ_b^k are taken between each receiver and each satellite. The baseline between the two receivers is also clearly indicated. The setup enables the formation of double-differenced carrier phase measurements which remove satellite and receiver clock effects and substantially mitigates atmospheric effects and other common

biases, thereby improving positioning accuracy.

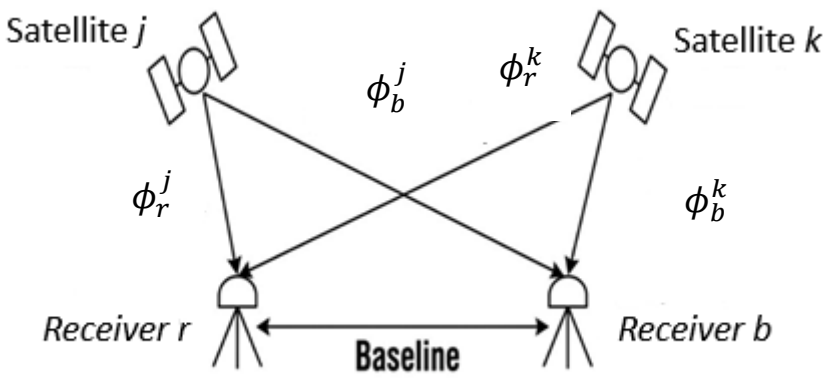


Figure 2.4: Geometry of a GNSS baseline setup used in relative positioning processing (Adopted from Takasu 2013).

Relative positioning uses single differencing to subtract observations that originate from the same satellite but reach two different receivers as follows:

$$\Delta P^s = \mathrm{P}_r^s - \mathrm{P}_b^s \tag{2.8}$$

This eliminates the satellite clock error. To reach higher precision, the method employs double differencing, which calculates differences between satellites and receivers:

$$\nabla\Delta \mathrm{P}_{r,b}^{s_i,s_j} = \left(\mathrm{P}_r^{s_i} - \mathrm{P}_r^{s_j}\right) - \left(\mathrm{P}_b^{s_i} - \mathrm{P}_b^{s_i}\right) \tag{2.9}$$

Relative positioning provides real-time cm level positioning when properly implemented. The system operates in marine navigation and vehicle tracking applications and general GIS data collection operations. Longer distances between base and rover receivers reduce the system performance because atmospheric errors become spatially decorrelated.

The RTK system requires both base and rover receivers to observe the same satellite

signals for their operation, as illustrated in Figure 2.5. While carrier-phase measurements offer millimetre-level precision, they are inherently ambiguous due to the unknown number of full wavelengths between the satellite and the receiver. In an RTK configuration, the carrier-phase integer ambiguities are solved in real time and fixed very rapidly, often within few minutes or seconds, changing from "float" solution to a "fixed" solution. Real-time fixing of ambiguities is the prerequisite to achieving reliable, stable single-cycle positioning of sub-centimetre accuracy for dynamic users. (Kaplan and Hegarty, 2017).

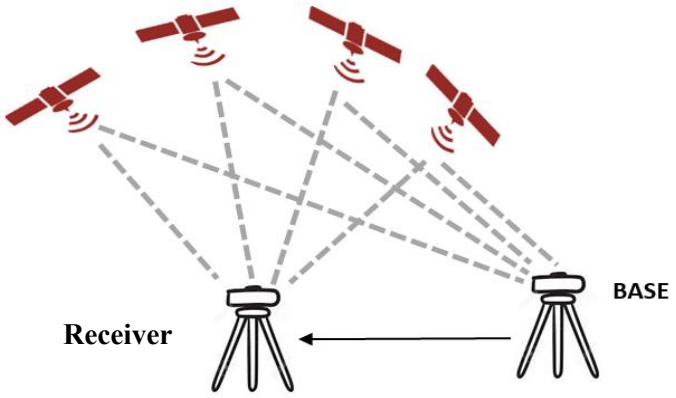


Figure 2.5: Real-Time Kinematic (RTK) positioning through simultaneous observation of common satellites by reference and rover receivers.

The basic equation for carrier-phase relative positioning uses the double-differenced carrier-phase model.

$$\nabla\Delta\Phi_{r,b}^{s_i,s_j} = \nabla\Delta\rho_{r,b}^{s_i,s_j} + \lambda\nabla\Delta N_{r,b}^{s_i,s_j} + \varepsilon_{\Phi} \tag{2.10}$$

This expression represents the carrier-phase measurement Φ and includes geometric range ρ and signal wavelength λ, and integer ambiguity N, as well as measurement noise ε_{Φ}. RTK technology provides real-time position data at centimetre accuracy levels and

finds application in land surveying and machine control and precision farming, and autonomous navigation. The NRTK method enables precise positioning throughout extensive areas because it utilises base station networks and correction interpolation techniques which preserve performance quality. The research by Bisnath et al. (2013) and Jensen and Cannon (2000) shows that RTK has a faster convergence time than PPP, but it also has some challenges in terms of network reliability.

Network RTK (NRTK) offers an improvement over single-base RTK. Rather than relying on single reference station for positioning, NRTK utilises a network of reference stations, often Permanent Reference Stations spread over an extensive geographic region. The centralized processing capability of the NRTK service interpolates atmospheric and orbital parameters to provide precise positioning corrections for the rover's exact location on the surface of the Earth. Both the Virtual Reference Station (VRS) and Master-Auxiliary Concept (MAC) approaches are implemented by the online software to counter ionospheric and tropospheric decorrelation effects. As a result, carrier phase integer ambiguities are resolved online over extended distances, and positioning accuracy and reliability are maintained at sub-centimetre levels throughout the service's geographic footprint (Bisnath et al., 2013).

2.5.6 Precise Point Positioning (PPP)

The Precise Point Positioning (PPP) method provides accurate positioning from a single GNSS receiver which operates independently without requiring reference station support, as shown in Figure 2.6. PPP has a global application and operates without reference stations in areas with restricted ground infrastructure. The IGS analysis centres, such as CNES, as well as the commercial SPARTN service, provide sufficient precise

satellite orbit and clock corrections for PPP applications. PPP processes both code and carrier phase measurements and requires physical models for tropospheric, ionospheric and hardware delays.

The effect of PPP has evolved from simple single-frequency effect to complex multi-frequency, multi-constellation effects (Bisnath and Gao, 2009). In particular, the Precise Point Positioning with Ambiguity Resolution (PPP-AR) technique is a significant development in PPP field which can resolve the integer phase ambiguities. To this end, several techniques have been proposed, e.g., decoupled clock models, fractional cycle biases estimation, etc. (Ge et al., 2008; Geng et al., 2019). In addition, the combination of Galileo and BDS signals can significantly improve the reliability of solution and shorten the convergence time (Li et al., 2022).

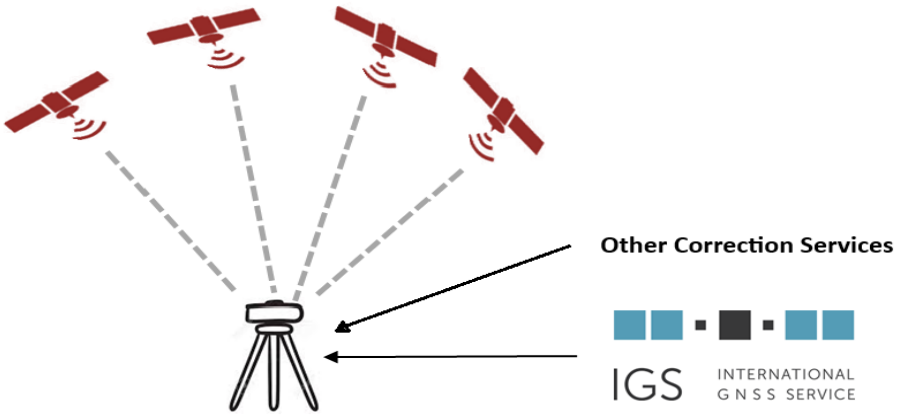


Figure 2.6: Conceptual framework of Precise Point Positioning (PPP). High-accuracy positioning is achieved by applying precise orbit and clock corrections (e.g., from IGS) to a standalone receiver.

The general observation models used in PPP are as follows:

Code measurement:

$$P_r^s = \rho_r^s + c(\delta t_r - \delta t^s) + T_r^s + I_r^s + d_p^s - d_p^r + \varepsilon_P \quad (2.11)$$

Carrier-phase measurement:

$$\Phi_r^s = \rho_r^s + c(\delta t_r - \delta t^s) + T_r^s - I_r^s + \lambda N_r^s + d_\Phi^s - d_\Phi^r + \varepsilon_\Phi \quad (2.12)$$

Here, d_p^s, d_p^r, and d_Φ^s, d_Φ^r are the satellite and receiver hardware biases for code and phase, respectively. N_r^s represents the carrier-phase ambiguity term. Ionospheric delays significantly impact positioning accuracy and can be modelled using various approaches that have undergone extensive evaluation in Precise Point Positioning (PPP) solutions. Research has demonstrated substantial improvements in ionospheric modelling performance, particularly in multi-GNSS environments (Aggrey, 2018; Banville et al., 2014).

PPP does not require the aid of a base station, however it suffers from longer convergence time (5–30 minutes) to achieve fixed position fixed state solution, unless integer ambiguity resolution (PPP-AR) is applied to resolve the ambiguities in the floating point solution.

2.6 GNSS Correction Formats and Services

The evolution of GNSS correction technology and services is driven by the growing need for accuracy and integration of diverse systems across various applications and users. The GNSS community has developed data standards to address issues of real-time provision and error mitigation, moving from global service availability challenges addressed by proprietary solutions to those met by open standards.

A common format for recording and post processing GNSS data was developed in the form of RINEX. This has become crucial as many applications can use RINEX data

generated by any receiver with any post processing software. For Real Time applications a different format is used, specified by the SC-104 committee of RTCM who have published several documents detailing the messages found within RTCM v3.0. The robust set of error detection and correction capabilities, along with the improved use of bit encoding and multi constellations have improved this version over previous releases. (RTCM SC-104, 2016).

The delivery of real-time correction information experienced improvements on both the NTRIP/RTIGS paradigm based on the internet and the traditional VHF/UHF broadcast paradigm, where improvements were realised using satellite links to boost coverage and reduce delays (Hirokawa & Fernández-Hernández, 2020). The Real-Time Service of the IGS provides free of charge real-time correction information with unprecedented accuracy and reduced latency for PPP applications performed in real time (Yi et al., 2020). These improvements in information distribution have generally been positive for users of state-space representation (SSR) information both in static and real-time environments. However, there are problems related to bandwidth and latency in the processing and distribution of state-space representation (SSR) products which can cause difficulties to users that are operating in real-time and mobile environments.

To address these gaps, several open correction formats have been developed:

- RTCM SSR: The state-space method of RTCM SSR delivers orbit and clock corrections with bias information along with a scalable message structure that supports real-time PPP and PPP-RTK operations (Vana et al., 2019).
- IGS SSR: The IGS SSR system is built upon RTCM SSR to provide universal open standards for worldwide services along with complete interoperability and future-proof design (IGS, 2016).

- CSSR: The CSSR which was originally developed for Japan's QZSS, CSSR utilises satellite and signal masking techniques to achieve up to a 70% reduction in data volume. These principles have since influenced global high-accuracy services, including the Galileo HAS (Hirokawa, 2019).

- SPARTN: It is a highly compressed, bandwidth-efficient binary structure. Optimised for low-latency delivery in constrained environments, SPARTN enables the secure, unidirectional broadcast of corrections over satellite and IP networks. It is specifically designed for mass-market applications, including automotive, IoT, and mobile robotics (Ferguson et al., 2020; u-blox AG, 2021).

GNSS correction formats started as basic differential corrections and now include advanced real-time-capable state-space representation (SSR) formats. The ongoing development of these open standards demonstrates a clear trajectory toward achieving precision while ensuring dependability and minimizing data bandwidth and expanding user access across all precision levels.

The correction data that are generated by the SPARTN correction services and the CNES correction services are both represented in a state space representation (SSR) and represent physical errors that affect the GNSS signals, such as satellite orbit errors, satellite clock errors, and signal bias errors (Hirokawa et al. 2021). The SPARTN correction services are generated for high-volume, real-time applications. The correction data are therefore produced in a bandwidth efficient format that is suitable for industry. The SPARTN correction services use a regional network approach, and include data that describe the atmospheric delays, such as the tropospheric delays and the ionospheric delays. The slant delays are typically represented on a wide-area grid, which enables fast

convergence of the measurement updates (Banville et al. 2022). In contrast, the CNES correction services generate real-time PPP products using a global tracking network that consists of around eighty permanent tracking stations (Rovira-Garcia et al. 2021). The real-time PPP products are generated using a multi-frequency, multi-constellation approach, in which the carrier-phase ambiguities are resolved in an undifferenced manner, using a Kalman filter to track the required parameters. The satellite orbit is updated every fifteen minutes, and the satellite clock is updated every second (Rovira-Garcia et al. 2021; Laurichesse et al. 2010). The primary focus of the CNES correction services is the geodetic-grade, high-precision, stability of the integer ambiguity resolution, which achieves a horizontal precision of a few centimetres (Hirokawa et al. 2021; Laurichesse et al. 2010). The SPARTN correction services are designed for mass-market, real-time navigation, and have a data rate of around 500 bps (He et al. 2020).

2.7 GNSS Correction Methodologies: OSR vs SSR

In recent years, more accurate GNSS correction augmentation systems have been developed aiming to provide high accuracy positioning service while preserving basic navigation principles. High-precision GNSS positioning is the ability to exactly determine the position of a user on earth within a few centimetres (1-10 cm) and thus clearly goes beyond the normal positioning on the metre level, which is done by means of the pseudoranges of the used satellites. High-precision positioning is achieved by Precise Point Positioning (PPP) and Real-Time Kinematic (RTK) positioning by means of the carrier-phase measurement of the used GNSS signals. By elimination of most errors, like ionosphere and troposphere delay, satellite-clock-errors and orbit-errors by using corresponding correction data and communication protocols (like SPARTN) within the

system, the normal error of some metres can be reduced to some centimetres. The high-precision positioning is required for applications like autonomous navigation, precision agriculture, mobile mapping services, surveying and many other geospatial services, which need exact positioning. The systems should enable global coverage and full interoperability among them. Utilising the State Space Representation (SSR) in system modelling is a novelty compared to traditional approach based on the Observation Space Representation (OSR).

Observation Space Representation (OSR) methodology currently employed by conventional Real-Time Kinematic (RTK) and Network RTK (NRTK) services aggregate error corrections specific to a reference station location into a “lumped” parameter that represents corrections computed as the difference between actual and theoretical distances to GNSS targets observing from the know reference station location. These corrections are then broadcast to rovers for positioning. Although Observation Space Representation (OSR) possesses high accuracy, it generally requires a bidirectional communication link (e.g., NTRIP) to obtain the rover's approximate position. This in fact limits the scalability of the approach because of the huge server-side computing intensity and bandwidth consumption per user.

Unlike object-space representation (OSR) approaches which provide a single correction value for every observable satellite signal, SSR approaches attempt to decompose the GNSS error budget into individual physical error sources. This is achieved by modelling the 'state' of the GNSS system:

- Satellite-specific states (Orbit, Clock Offset, Code/Phase Bias, etc.)
- Atmospheric States - Regional Slant Range Delays (Ionosphere) and Zenith Path

Delays (Troposphere)

State space representation (SSR) provides a more flexible positioning filter. The error components can be separately modelled and broadcast in a unidirectional stream to an arbitrary number of users. This enables error corrections to be distributed efficiently over an extensive area without a nearby physical base station, and with a drastically reduced bandwidth for high-precision positioning. The SSR-based corrections enable PPP-RTK (Precise Point Positioning-RTK), a hybrid approach that combines the global availability and fast convergence of PPP with the accurate local network corrections including atmospheric parameters distributed by SSR (Wübbena et al. 2005; Hirokawa and Fernández-Hernández 2021; Takasu 2013).

GNSS positioning can be performed in real-time as well as in a post-processed way. For real-time positioning, data from the GNSS receivers is processed immediately within the application. Such processing is done in real-time utilising permanent data streams, such as the above-mentioned SPARTN protocol, and allows for highly accurate positioning in the order of sub-decimetres and is mainly used for dynamic applications (Vana et al., 2019). In the post-processed case, precise satellite orbits (so called precise satellite products) are applied in a retrospectively manner. While unsuitable for real time application, post-processing provides the geodetic-grade accuracy necessary to serve as a reference 'ground truth' against which real-time system performance is measured.

2.8 RTKLib Software

RTKLib is an open-source software capable of fully conducting GNSS positioning, developed by Takasu (2013). The software delivers multiple positioning functionalities which includes Single Point Positioning (SPP), Precise Point Positioning (PPP), and Real-

Time Kinematic (RTK), and it can be applied in geodesy surveying and navigation. RTKLib includes position calculation methods which are optimised for GNSS functions. The extended Kalman filter (EKF) of the software generates accurate positions during PPP and RTK, and Differential GNSS operations. The filtering approach minimises typical errors such as satellite and receiver clock biases and ionospheric delays, and tropospheric delays, especially when the rover-base station distance reaches less than 10 kilometres (Takasu, 2013).

The PPP solution in the RTKLib can be performed with different correction models which use satellite broadcast messages, space-based augmentation systems (SBAS), and precise ephemerides and clock products (SP3-c or RINEX files). It allows PPP solutions to be processed in post-processing instead of real-time operations. At present, this code is experimental and only tested and working for the wide-lane FCB (Fractional Cycle Bias) and IRC (Integer Recovery Clock) products provided by CNES (Takasu, 2013). It requires accurate time keeping, which is given by GPS Week and GPS Time of Week in fractional second increments on sub-millisecond time scales. As a software application, it requires precise range calculations to the satellites for its accurate positioning determination. The satellite positions for range calculations are provided in the Earth-Centred Earth-Fixed (ECEF) reference frame. The software performs essential transformations between geodetic, local, and ECEF coordinates to ensure smooth reference frame operations.

RTKLib applies various methods to apply atmospheric corrections because these corrections are essential for improving positioning accuracy. The Saastamoinen model, together with SBAS and zenith tropospheric delay (ZTD) estimation methods, serves as a tropospheric correction model that RTKLib implements according to specific application

requirements. It implements multiple ionospheric correction techniques, including satellite broadcast corrections together with SBAS and an ionosphere-free linear combination model to reduce ionospheric disturbances in signal propagation (Takasu, 2013).

RTKLib provides calculations for pseudorange measurements as well as carrier-phase ranges and geometric distances between satellites and receivers. It generates satellite elevation and azimuth measurements, which serve as vital data for both immediate positioning and subsequent analysis. This system consists of multiple programs which function as separate modules to process GNSS data processing requirements. The real-time processing program RTKNAVI enables file-based or serial or network-based data input/output functionality with or without RTK capabilities. The RINEX format converter RTKCONV processes raw GNSS data before RTKPOST executes post-processing solutions that duplicate real-time operations on recorded data. RTKPLOT offers graphical tools for GNSS result evaluation through ground tracks and position plots, and sky plots (Takasu, 2013). Figure 2.7 shows the main graphical user interface (GUI) of RTKLib version 2.4.2, highlighting its key components such as RTKPLOT, RTKCONV, STRSVR, RTKPOST, NTRIP Browser, RTKNAVI, and RTKGET. These modules serve various functions in GNSS data processing, from real-time kinematic (RTK) positioning to file conversion and visualization.

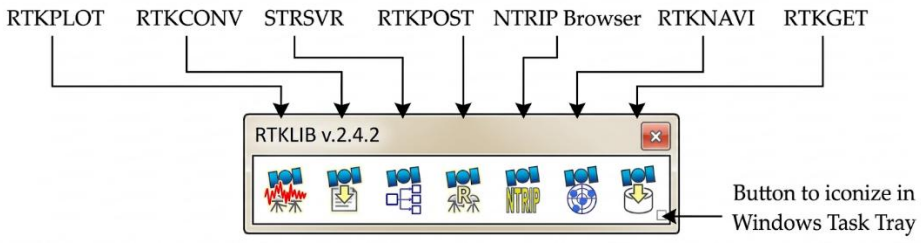


Figure 2.7: RTKLAUNCH interface showing core modules (Adapted from Takasu, 2013).

RTKLib functions on Windows and UNIX platforms by providing Windows users with GUIs and UNIX users with CLIs. The software supports a wide range of GNSS receiver protocols, including Novatel, u-blox, Hemisphere and JAVAD models, providing maximum flexibility for users implementing GNSS systems. This is a software library developed for researchers and engineers, and surveyors alike that supports basic GNSS positioning, advanced PPP and RTK positioning functionality. RTKLib remains a widely used GNSS positioning and research tool because of its open-source nature and extensive algorithm capabilities and platform compatibility (Takasu, 2013).

2.9 YorkPPP Software

YorkPPP software is capable of tracking a wide range of positioning satellites from multiple constellations. The software utilises Microsoft .NET Framework and ANSI C++ for its development, creating robust, portable yet optimally performing code. Over 27k lines of C++ code comprise the software's architecture. Modern software engineering techniques have been utilised when designing the software. A flexible and scalable design framework was developed, with an object orientated design core. The rapidly changing satellite navigation landscape has been considered adequately allowing for straightforward integration of new satellite constellations as well as additional processing routines. The system used four essential blocks, including File Readers for data input processing, as well as Error Correction and Data Quality Control and Filters. Figure 2.8 shows the architecture of the YorkPPP processing engine before the implementation of SPARTN corrections (Aggrey, 2014; Seepersad, 2012).

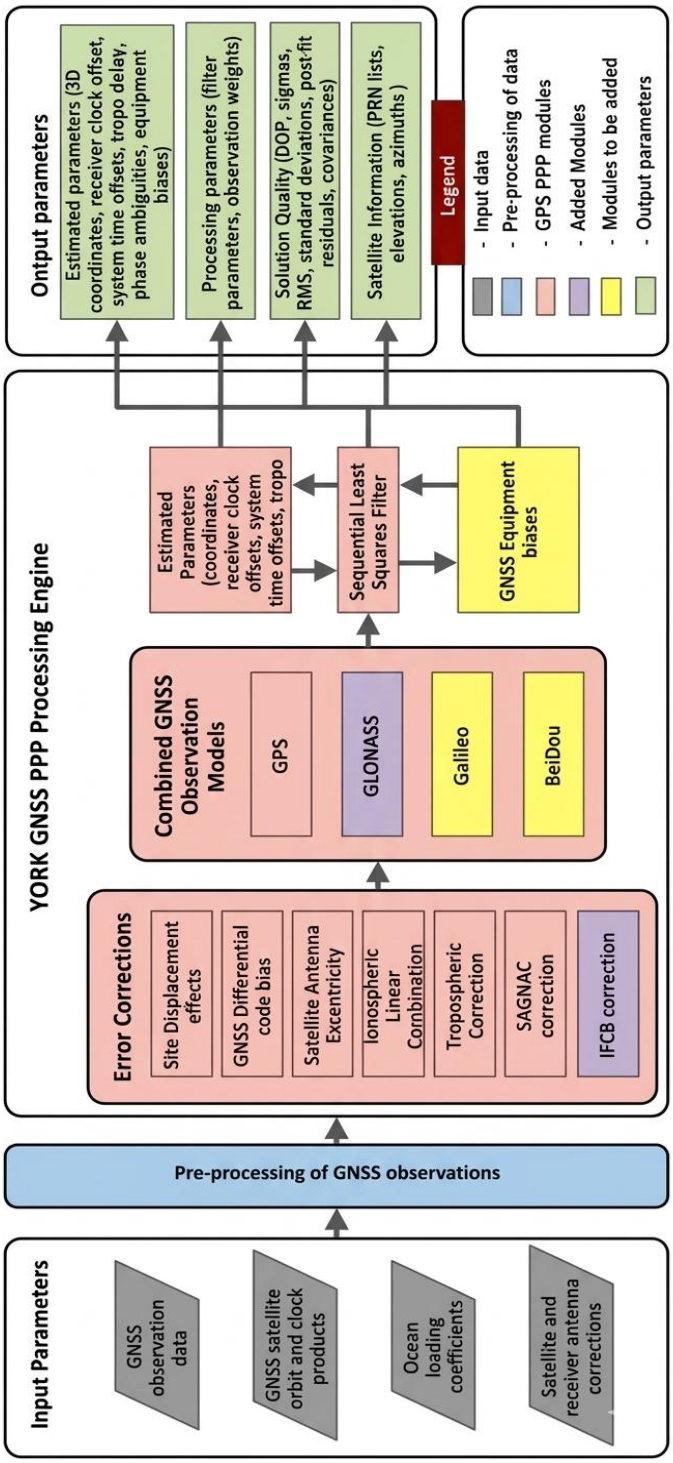


Figure 2.8: York-PPP system overview showing the integration of multi-GNSS data and error modelling via sequential least-squares filtering. (Adapted from Aggrey, 2014; Seepersad, 2012).

The File Reader block is followed by the Error Correction block to prevent systematic errors that would decrease position accuracy. The component integrated complex atmospheric emission correction models, which included tropospheric delay models and ionospheric error correction techniques. The system implemented solutions to three satellite anomalies by processing relativistic effects and orbital anomalies, and clock error calibrations. The Data Quality Control component was added for validating satellite observations before PPP processing. The block applied satellite data analysis and filtering through advanced methods, which included cycle slip recognition and geometry-free carrier-phase linear combination. The positioning solutions operated exclusively on high-quality satellite data. Data preprocessing techniques, such as cycle slip detection, are essential for maintaining high GNSS positioning quality (Blewitt, 1990).

The Filters block operated as the core processing component of the software. This block executes sophisticated parameter estimation through epoch-by-epoch least-squares filtering and sequential least-squares estimation. The observations from both stationary terrestrial sites and mobile positions needed for kinematic applications are managed by this filtering approach. Real-time parameter adjustments became possible through the addition of adaptive state tracking functionality.

A highly adaptable setup procedure was developed, allowing users to specify processing parameters through configuration files. The parameters controlled which satellite systems to use (GPS, GLONASS, Galileo, BeiDou), which observation types to combine (single, dual, or triple frequency observations), which error correction models to apply, how to resolve ambiguities and what output formats to generate.

The processing software enables GNSS processing of multiple frequencies and

constellations, which allows GPS and Galileo and GLONASS, and BeiDou observation integration. The software achieves high-precision results by utilising the Decoupled Clock Model (DCM) to isolate and estimate code and phase clock biases, followed by the LAMBDA algorithm to perform the actual integer ambiguity resolution. The system includes bias compensation for inter-system and inter-frequency signals, which enhances carrier-phase ambiguity resolution and positioning accuracy during the initial processing stages.

The software can generate multiple output files. The FilterOutput file contains the final data output of positions for analysis and decision making. The ProcessedEpochOutput file can contain a time series evaluation of the data by epoch. The newGeneralOutput file contains output of the software in a machine-readable form that can be passed directly to other software programs for automated post processing. The debugOutput file can contain development test data and diagnostics at an intermediate point in the software processing.

The software demonstrated its ability to achieve centimetre-level horizontal accuracy while maintaining efficient processing even when dealing with complex observation environments. The software provides better precision and faster convergence through its ability to process multiple GNSS signals.

3. The SPARTN Protocol and Corrections Framework and Implementation

The SPARTRN protocol is optimised for use in automotive and mass-market applications requiring high accuracy GNSS. The low-bandwidth State Space Representation (SSR) architecture ensures integrity of data and is specifically suited for safety-critical applications (Ferguson et al., 2020; Vana et al., 2019). The configurable message structure is capable of efficiently supporting a variety of communication channel types including L-band satellite as well as IP-based networks, and can support multi constellations of GPS, GLONASS, Galileo and BeiDou. Analysis of the corrected data stream reveals the SPARTN protocol can provide sub-decimetre horizontal positioning accuracy within a few minutes for initial fix (Vana et al., 2019; Kim et al., 2021). As an open standard, the protocol optimises bandwidth without compromising security. The frame structure includes a clear repeatable preamble, message type, length of payload fields, and encryption/authentication flags, and is protected by a dual-layer Cyclic Redundancy Check (CRC) to safeguard against data corruption and/or unauthorized access (Ferguson et al., 2020; Vana et al., 2019).

The SPARTN protocol is extended to support position information by transmitting High Precision Atmospheric Correction (HPAC) data, which corrects for ionospheric and tropospheric delays. This correction data provides a Message Type 1, commonly referred to as HPAC. The advantage of this Message Type 1 is that it enables ionospheric modelling using Slant Total Electron Content (STEC) as opposed to the conventional Vertical Total Electron Content (VTEC) and provides also accurate tropospheric delay values. As a result,

the final position information is significantly more accurate due to the line-of-sight correction which is relevant for the actual signal path to the receiver location (Kim et al., 2021, u-blox AG, 2021).

The application of these atmospheric corrections depends on the Geographic Area Definition (Message Type 2). This message defines the spatial validity of the atmospheric model, specifying the valid regions, grid points, and polynomial expansion points for the data transmitted in Message Type 1. The geographic area is structured around a defined reference point with coordinates represented by a network of evenly spaced grid points (u-blox AG, 2021). Users can specify a geographic area relevant to their current estimated position and then use this area to interpolate both gridded and polynomial atmospheric data to apply the broadcast corrections with high spatial accuracy. This is a key factor in ensuring the integrity and precision of the positioning solution (u-blox AG, 2021). Figure 3.1 illustrates the full chain of correction data derivation at the GNSS reference stations and its broadcasting over IP and L-band channels.

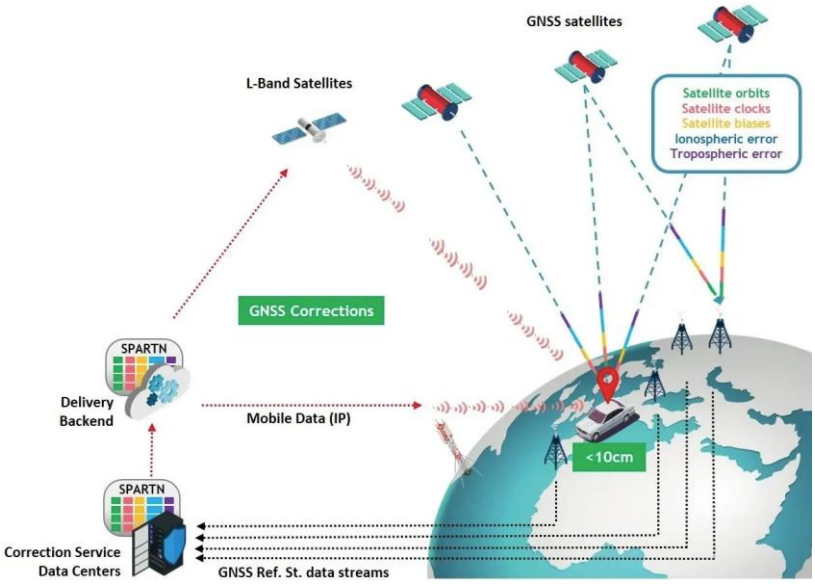


Figure 3.1: Overview of SPARTN-based GNSS correction delivery architecture (Adapted

from u-blox AG, 2021).

3.1 SPARTN Orbit, Clock and Bias Messages

While the implementation of SPARTN differs from that of RTCM SSR and Compact SSR (CSSR), all three use State Space Representation (SSR). In the case of the SPARTN correction format, it combines several correction parameters, which are transmitted in one message (e.g. satellite masks, orbit and clock corrections, code and phase corrections as well as User Range Accuracy (URA) information) for a given time frame (epoch) in a unified message structure. By packaging all essential correction data for a given epoch into a unified message structure, SPARTN reduces message header overhead and minimises the latency commonly associated with fragmented multi-part RTCM SSR transmissions (Vana et al., 2019; Hirokawa & Fernández-Hernández, 2020).

To satisfy the large number of mass-market customers requiring real-time positioning information, efficient transmission of information to users in a timely manner is crucial. SPARTN information is of different nature, and therefore it is sent at different time intervals, based on the time variability of each error source. Orbit, Clock, and Bias (OCB) corrections, transmitted through Message Type 0, contain parameters with varying update requirements. Satellite clock corrections, which vary rapidly, are typically broadcast at intervals of approximately 5 seconds to capture short-term clock drift, whereas orbital corrections are generally updated every 30 seconds due to their slower temporal variation. The High Precision Atmosphere Correction (HPAC) information is sent every 30–60 seconds as the ionospheric and tropospheric errors vary at a much slower rate and can be modelled with high precision using information from a regional network of Continuously Operating Reference Stations (CORS).

Atmospheric corrections are typically generated from measurements of local continuously operating reference stations (CORS) and modelled at high spatial resolution. The local corrections are distributed in SPARTN via Geographic Area Definition (GAD) messages. These messages split the area where a service is provided into several localized correction grids, enabling efficient distribution of the corrections for a given region, while achieving nominal end-to-end latency of below 5 seconds, thereby supporting real-time centimetre-level positioning performance.

3.1.1 GNSS Orbit Corrections

Precise satellite positioning is essential for modern PPP techniques. To determine satellite position, RTKLib utilises satellite ephemerides broadcast in the navigation message and data provided by agencies such as IGS, a technique called augmented positioning. This software decodes SP3 file from IGS and corresponding RINEX files, and by utilising Lagrange interpolation, it computes positions at any time for satellites in orbit around the Earth (Takasu, 2013). Similarly, for York-PPP, satellite orbits are corrected using precise products from GFZ and IGS where accuracies on the order of 1–2 cm have been achieved. The code features a modular design that includes dedicated reader classes for high-precision orbital data of all relevant constellations (Aggrey, 2014).

As part of this research, SPARTN corrections were integrated into RTKLib and YorkPPP, enabling the augmentation of broadcast ephemerides to generate more accurate satellite positions. The standardized Message Type 0 (SM 0) serves as the SPARTN container for Orbit, Clock, and Bias (OCB) corrections, which include mask data and orbit corrections and clock corrections and code biases and phase biases and User Range Accuracy that enhance the overall accuracy of satellite positioning (u-blox AG, 2021). The

orbit corrections improve the satellites' positions in three dimensions: radial, along-track and cross-track.

The calculation of the correction vector δX starts with determining the satellite position correction vector. The correction vector δX derives its values by determining the direction unit vectors for radial and along-track and cross-track components from the satellite broadcast position vector (r) and velocity vector (ṙ). The radial unit vector (e_{radial}) results from taking the cross product of the along-track (e_{along}) and cross-track (e_{cross}) unit vectors, which are derived from the broadcast velocity and position vectors. The correction vector δX results from combining the unit vectors with their respective orbit correction values δO_{radial}, δO_{along} and δO_{cross} (u-blox AG, 2021).

The satellite position correction δX is computed as:

$$e_{along} = \frac{\dot{r}}{|\dot{r}|}$$

$$e_{cross} = \frac{r \; x \; \dot{r}}{|r \; x \; \dot{r}|}$$

$$e_{radial} = e_{along} \; x \; e_{cross}$$

$$\delta X = [\, e_{radial} \quad e_{along} \quad e_{cross}] \begin{bmatrix} \delta O_{radial} \\ \delta O_{along} \\ \delta O_{cross} \end{bmatrix} \tag{3.1}$$

Were

r = satellite broadcast position vector, $\dot{r}$ =satellite broadcast velocity vector and e = direction unit vector

This correction vector is applied to the broadcast satellite position (X_b) from RTKLib to produce the corrected position of the satellite's nominal antenna phase centre (X_{orb}). The

corrected position of the satellite's nominal antenna phase centre $X_{Orb} = X_b - \delta X$, where X_{Orb} represents the corrected satellite position after incorporating the SPARTN corrections(u-blox AG, 2021). This correction allows the satellite's position to be corrected with higher precision by accounting for the real-time condition with significantly improved accuracy compared to using only the broadcast ephemerides (u-blox AG, 2021).

3.1.2 GNSS Clock Corrections

Synchronous satellite clock bias and drift estimation is essential for achieving high accuracy positioning. RTKLib uses broadcast information for conventional clock bias and drift estimation. For higher accuracy positioning, it also enables the use of accurate satellite clock information provided by IGS in SP3 or Clock RINEX format. It linearly interpolates between precise clock epoch and applies relativistic correction using satellite position and velocity (Takasu, 2013).

The York-PPP system is based on a more advanced Decoupled Clock Model (DCM) that separates the receiver clock terms for pseudorange and carrier-phase measurements to allow for better estimation of receiver hardware biases. It supports the use of precise satellite clock corrections (e.g., from GFZ) that are compatible with CNES bias products, thus enabling PPP with ambiguity resolution (PPP-AR). York-PPP further has the capability to handle constellation specific offsets, such as offsets between BDS-2 and BDS-3 to prevent misalignment of clock terms that otherwise would impede accuracy improvement and ambiguity resolution (Adu, 2025).

As part of the SPARTN integration, the Message Type 0 (OCB) provides a specific clock correction parameter, denoted as δC. This correction is combined with the broadcast satellite clock time, t_b, from RTKLib to compute the corrected satellite clock, t_s, using the

formula $t_s = t_b - \frac{\delta C}{c}$, where c represents the speed of light. It's important to note that relativistic effects must be applied to all constellations except for GLONASS, where these effects are already accounted for in the broadcast clock parametre (u-blox AG, 2021).

3.1.3 GNSS Bias Corrections

For multi-frequency processing and integer ambiguity determination, precise bias modelling is necessary. In RTKLib, the carrier-phase biases are incorporated into the state vector of an Extended Kalman Filter (EKF). For code biases, the system uses Differential Code Bias (DCB) products of mapping centres, such as those provided by the Centre for Orbit Determination in Europe (CODE), to correct the systematic frequency differences. These corrections are applied by subtracting the DCB values from the measured distances (pseudoranges) in the navigation algorithm (Takasu, 2013).

York-PPP uses Observable-Specific Biases (OSB) and existing code/phase bias products from CNES that are consistent with GFZ orbit and clock time series (Adu, 2025). Within the Decoupled Clock Model (DCM) framework, the receiver hardware biases are parameterized and treated as independent time series parameters as they are generally assumed to be much more stable than the position and clock parameters rather than as constant offsets (Aggrey, 2014). For multi-frequency processing (beyond L1/L2), the biases between frequency pairs (IFB) are modelled as white noise processes to enable use of a Filter object rather than requiring separate Dynamic Models for each (Adu, 2025). This allows both satellite and receiver hardware delays to be modelled for all constellations.

In the SPARTN protocol, the Message Type 0 (OCB) provides high-precision bias parameters for specific signal tracking types, which are then subtracted from the original pseudorange and carrier-phase measurements relevant to each type (u-blox AG, 2021).

3.2 SPARTN geographic area definition message

The Geographic Area Definition (Message Type 2) provides the geographic area for which atmospheric corrections can be applied and complements the information contained in Message Type 1. The geographic area is defined by a reference point expressed in latitude and longitude, and a grid of points. The message also specifies the expansion points for the polynomial that models the data for the atmospheric corrections (Hirokawa & Fernández-Hernández, 2020). The geographic area is defined by a series of points of an equally spaced grid of nodes (u-blox AG, 2021).

During the positioning process, the receiver selects the appropriate geographic area based on its approximate coordinates. This selection allows for the secure and precise interpolation of both polynomial and gridded atmospheric data. By localized modelling of the ionospheric and tropospheric delays, the system maintains high positioning accuracy and solution reliability across diverse regional environments (u-blox AG, 2021). Figure 3.2 illustrates the standardized grid layout and the spatial relationship between the expansion points and the user's location.

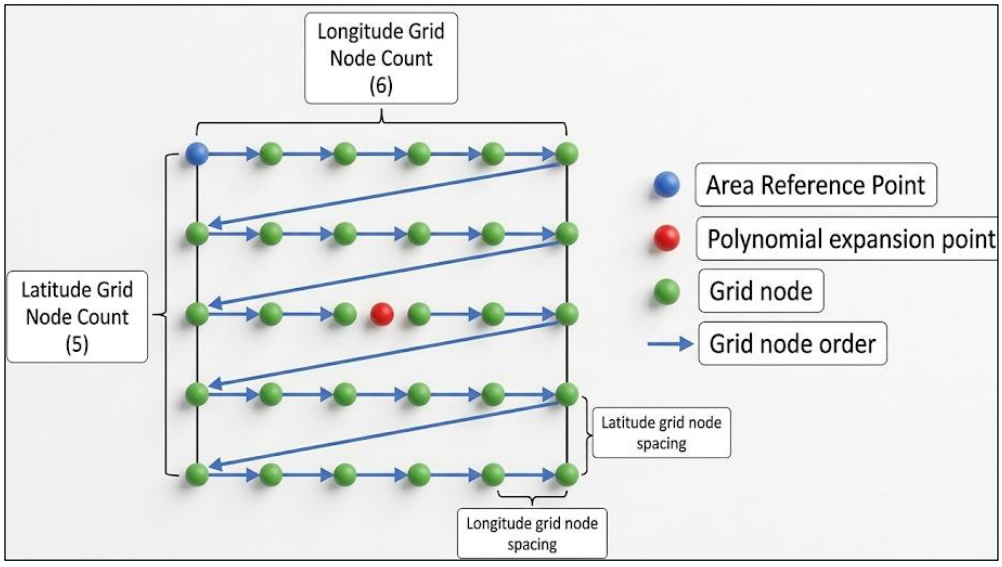


Figure 3.2: Structure of the SPARTN area-based grid used for atmospheric correction representation (Adapted from u-blox AG, 2021).

3.3 Atmospheric correction messages

SPARTN provides a correction message called Type 1 High Precision Atmospheric Correction (HPAC), which focuses on correcting ionospheric and tropospheric delays. High Precision Atmospheric Correction (HPAC) offers ionospheric delay corrections using Slant Total Electron Content (STEC) rather than Vertical Total Electron Content (VTEC), and it includes corrections for tropospheric delays, enhancing the accuracy of positioning for users (Kim et al., 2021). Figure 3.3 illustrates the of geographic area definitions (tiles) used in SPARTN correction employed by SPARTN correction.

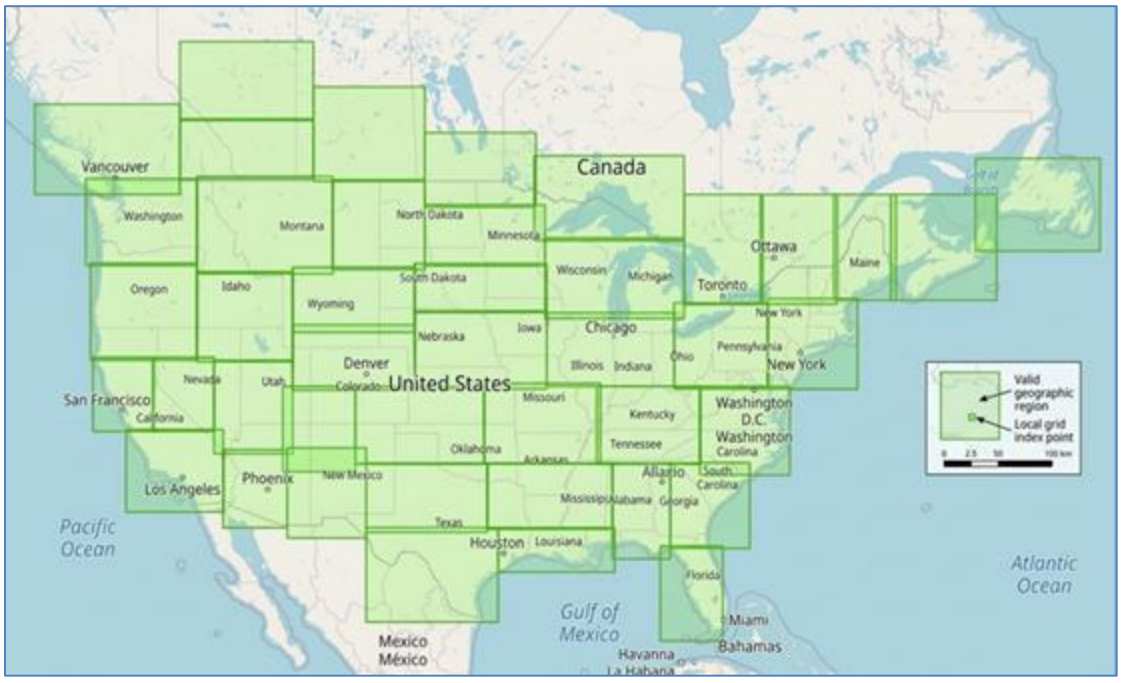


Figure 3.3: Example of geographic area definitions (tiles) used in SPARTN correction services for North America (Adapted from u-blox AG, 2021).

3.3.1 Ionospheric corrections

The ionospheric correction in RTKLib is calculated using various model depending on the specified processing option. Single frequency users can use the broadcasted ionosphere model using Klobuchar model, which is described in the GPS Interface Document. The Klobuchar model uses constants of the ionospheric delay that are contained in the GPS and QZSS navigation messages and estimates the ionospheric delay based on the satellite position, receiver position and the Total Electron Content (TEC) along the signal path. For dual frequency measurements, the ionospheric effects can be reduced or eliminated using an ionosphere-free linear combination (LC) of L1/L2 or L1/L5 signals based on the supported GNSS. Additionally, SBAS ionospheric corrections can also be applied by using messages in the SBAS data. IONEX files, which contain a TEC grid, can also be read for more accurate ionospheric correction. Appropriate values are then interpolated to the position of the ionospheric pierce point (IPP) for the time of the measurement was made. This allows a very accurate removal of the ionospheric delay from the measurements for accurate GNSS positioning (Takasu, 2013).

The YorkPPP engine uses an uncombined processing method for ionospheric correction that estimates ionospheric delays as independent variables instead of combining them into linear equations (Adu, 2025). Delays are determined for the primary frequency and is scaled to other frequency using frequency-dependent γ ratios (Aggrey, 2014). The ionospheric delay parameters receive white noise treatment in the estimation filter which enables their epoch-by-epoch variation to capture ionospheric condition changes (Adu, 2025). YorkPPP's uncombined approach delivers superior ionospheric delay estimation compared to traditional Klobuchar models, because it works well for single-frequency

users and areas with intense ionospheric activity.

In the context of high-precision atmospheric correction within SPARTN, the ionospheric slant delay for each satellite is calculated using a specific formula that differentiates between carrier-phase and pseudorange measurements. The slant ionospheric delay for the carrier-phase measurement δI_{CP}^{i} and the pseudorange measurement δI_{PR}^{i} for a given satellite i are calculated as follows:

$$\delta I_{CP}^{i} = -40.3 \,.\, \frac{10^{-16}}{f_j^2} \,.\, \left(I_P^i + I_G^i\right) \tag{3.2}$$

$$\delta I_{PR}^{i} = 40.3 \,.\, \frac{10^{-16}}{f_j^2} \,.\, \left(I_P^i + I_G^i\right) \tag{3.3}$$

Here, δI_{CP}^{i} represents the slant ionospheric delay for the carrier-phase, and δI_{PR}^{i} represents the same for the pseudorange, both measured in metres. f_j^2 is the frequency of the GNSS signal. I_P^i refers to the slant ionospheric delay evaluated through a polynomial model for the satellite i and is measured in TECU (Total Electron Content Units). I_G^i is the interpolated residual slant ionospheric delay, derived from a gridded set of residuals for the satellite, also in TECU. If grid data are unavailable, I_G^i is assumed to be zero (u-blox AG, 2021).

To calculate the residual slant delay I_G^i for the user's position, a bi-linear grid interpolation method is employed. This method uses the weights W_k corresponding to the grid points k and the associated residual slant ionospheric delay values I_G^i. The formula is given by:

$$I_G^i = \sum_{k=1}^{4} W_k \,.\, I_{G\,k}^{\,i} \tag{3.4}$$

Where, W_k is the weight applied to the grid point k, and I_G^i is the residual slant ionospheric delay at grid point k for satellite i.

The slant ionosphere delay I_P^i is calculated for the user's location by considering the distance between the user's latitude and longitude coordinates and the centroid of the specific area being considered. The user's latitude ϕ_u and longitude λ_u are compared to the centroid latitude ϕ_c and longitude $\delta\lambda_c$ of the area, with the differences $\delta\emptyset_p = \phi_u - \phi_c$ and $\delta\lambda_p = \lambda_u - \lambda_c$ used in the polynomial model f_p to compute I_P^i. The polynomial representation, as described in data field SF054, can take different forms depending on the degree of complexity required, ranging from a simple constant to a more complex polynomial involving both latitude and longitude differences. This model ensures that the ionospheric delay is accurately adjusted based on the user's position, leading to more precise GNSS measurements (u-blox AG, 2021). The polynomial representation for ionospheric correction in SPARTN is:

$$0: I_P^i = C_{00}$$

$$1: I_P^i = C_{00} + C_{01}(\delta\emptyset_p) + C_{10}(\delta\lambda_p)$$

$$2: I_P^i = C_{00} + C_{01}(\delta\emptyset_p) + C_{10}(\delta\lambda_p) + C_{11}(\delta\emptyset_p)(\delta\lambda_p) \qquad (3.5)$$

These SPARTN messages make use of a very flexible polynomial-based atmospheric modelling approach. The coefficients C_{00}, C_{01}, C_{10}, and C11 represent the spatial parameters for modelling the ionospheric delay within a service area. The mathematical formulation for applying these corrections is defined by an equation-type flag (0, 1, or 2) embedded in the header of each SPARTN message for a particular epoch. Equation type 0 represents a constant ionospheric correction which is applied uniformly throughout the

service area. Equation type 1 represents a linear or first-order ionospheric correction that includes first-order spatial gradients, while equation type 2 models higher-order behaviour, represented by a linear mixed model of higher orders. This hierarchical approach allows the positioning engine to select an ionospheric correction model that best matches the complexity of the atmosphere for a given point in space as determined by the SPARTN correction provider.

3.3.2 Tropospheric corrections

RTKLib computes tropospheric delay using models like the Saastamoinen model, which estimates the zenith hydrostatic delay based on surface conditions and applies mapping functions such as the Niell Mapping Function to account for satellite elevation angles. In addition, Global Pressure and Temperature (GPT) model and Global Mapping Function (GMF) are utilised to precisely determine atmospheric parameters. Tropospheric delay can be finely adjusted within Kalman filter processing, especially in PPP mode. The delay is represented as Zenith Tropospheric Delay (ZTD) in Kalman filter's state vector, and it is updated based on time-series observed data with the random-walk nature of change. ZTD + Gradient model of RTKLib even accurately estimates not only ZTD but also two horizontal gradients (north/south and east/west) which are affected by atmospheric asymmetry, and tropospheric delay is adjusted dynamically to increase accuracy of GNSS positioning. (Takasu, 2013).

YorkPPP implements a dual-component tropospheric delay correction system which separates dry atmospheric effects from wet atmospheric effects (Aggrey, 2014; Adu, 2025). The GMF with established atmospheric models that include temperature and pressure, and seasonal variations models the dry tropospheric component, which makes up about 90% of

the total zenith delay (Adu, 2025). The wet tropospheric component receives a random walk process treatment with a 0.05 $\frac{mm}{\sqrt{h}}$ process noise to enable its adaptation to changing atmospheric water vapour conditions. The zenith wet tropospheric delay serves as an unknown parameter which gets transformed into satellite-receiver line-of-sight directions through suitable mapping functions (Aggrey, 2014). YorkPPP uses two techniques for modelling the dry components and dynamically estimating the time changing wet components for robust tropospheric path delay corrections.

In SPARTN, the tropospheric slant delay δT^i for a satellite at the user's location is calculated by combining several key components. The process begins with the zenith hydrostatic delay $\overline{T_h^z}$, which is the average delay for the given area, referenced to zero ellipsoidal height (WGS 84). This delay is adjusted using two mapping functions: the hydrostatic mapping function $m_h(\epsilon_i, h)$, which accounts for the satellite's elevation angle and the user's ellipsoidal height, and the non-hydrostatic mapping function $m_{nh}(\epsilon_i)$, which adjusts for non-hydrostatic components based on the satellite's elevation angle. Additionally, residual tropospheric delays are incorporated into the calculation. The residual delay T_G is interpolated from a grid of precomputed values using bi-linear interpolation, where the delay is weighted by proximity to four surrounding grid points (u-blox AG, 2021):

$$T_G^i = \sum_{k=1}^{4} W_k \,.\, {T_G}_k^i \tag{3.6}$$

Another residual delay, T_p, is calculated using a polynomial expansion that considers the difference in latitude $\delta\emptyset_p = \phi_u - \phi_c$ and longitude $\delta\lambda_p = \lambda_u - \lambda_c$ between the user's location and the area's centroid. The polynomial representation for tropospheric correction

in SPARTN is:

$$0: T_P^i = T_{00}$$

$$1: T_P^i = T_{00} + T_{01}(\delta\emptyset_p) + T_{10}(\delta\lambda_p)$$

$$2: T_P^i = T_{00} + T_{01}(\delta\emptyset_p) + T_{10}(\delta\lambda_p) + T_{11}(\delta\emptyset_p)(\delta\lambda_p) \quad (3.7)$$

The tropospheric delay is also addressed using adaptive modelling in the SPARTN High Precision Atmosphere Correction (HPAC) processing, for estimating Zenith Wet Delay (ZWD) corrections, using coefficients T_{00}, T_{01}, T_{10}, and T_{11}. The equation-type flag (0, 1, or 2) embedded in the SPARTN message determines the mathematical model representation. For Equation type 0, a constant tropospheric model is used where a single uniform correction is applied for the entire observing region. Equation type 1 corresponds to a linear model, or first-order spatial variations of the slant wet delay, accounting for variations of atmospheric water vapor and pressure. For Equation type 2, a higher-order linear mixed model representation is used to model the more complex, non-linear variations of the tropospheric wet delay. This allows the processing engine to choose the most appropriate model to represent the tropospheric delay for the given atmospheric conditions, and to correct for the highly variable wet delay component to provide highest possible positioning accuracy and solution stability.

The final slant delay is the sum of these adjusted and interpolated values, allowing for a precise estimation of the tropospheric delay at the user's specific location (u-blox AG, 2021).

$$\delta T^i = \overline{T_h^z} m_h(\epsilon_i, h) + (T_p + T_G).m_{nh}(\epsilon_i) \quad (3.8)$$

3.4 Corrections implementation

By using State Space Representation (SSR) corrections of satellite and atmospheric errors instead of the traditional Observation Space Representation (OSR) methods employed by GNSS positioning systems, corrections of satellite and atmospheric errors processed at reference stations are transmitted as state variables to users. Measured correction updates of state-space representation (SSR) are transmitted as time correlated time series. Users can perform an interpolation measurement to obtain the current measurement, which reduces the required bandwidth as compared to traditional methods using raw observation corrections in Observation Space Representation (OSR) systems (Wübbena and Willgalis 2001).

The state-space representation (SSR) methodology overcomes the traditional problem of back-and-forth communication between users and network providers by using dense reference networks to provide precise atmospheric corrections to users. As a result, user positioning becomes fast and accurate without requiring prior knowledge of user location. The principal benefit of SSR corrections lies in their ability to quickly converge in a few fixes via interpolation of network boundary atmospheric corrections, particularly for dense reference station configurations (Talbot et al. 2002; Wübbena et al. 2005). The state-based frameworks of SSR-based systems use station networks to compute satellite corrections before distribution, which resembles PPP processing but delivers regional network precision.

The modern implementation of state-space representation (SSR) based positioning services is represented by SPARTN corrections. The research assesses both the practicability and performance effects of using local SSR corrections in PPP processing systems, which guides the implementation of SPARTN corrections in existing PPP

frameworks. The study breaks away from conventional practices by studying how local network corrections can boost PPP performance through state-space representation while preserving its core benefits.

3.4.1 Decoding of corrections

The SPARTN protocol optimises bandwidth usage to efficiently distribute highly accurate GNSS corrections (u-blox, 2021; ESA, 2022). Its primary objective is to maximize bandwidth efficiency without compromising the resolution of the correction data. The compact binary format organises a diverse set of correction parameters including satellite ephemerides, clock corrections, tropospheric and ionospheric total delays and signal specific biases for code and carrier phase measurements. With a goal of optimizing efficiency without sacrificing resolution, the protocol applies a range of optimizations including satellite grouping and time-scaled SSR as well as multi-resolution models of the troposphere and ionosphere. Figure 3.4 illustrates the staged decoding architecture employed by the SAPALIB library to manage and parse these incoming SSR messages.

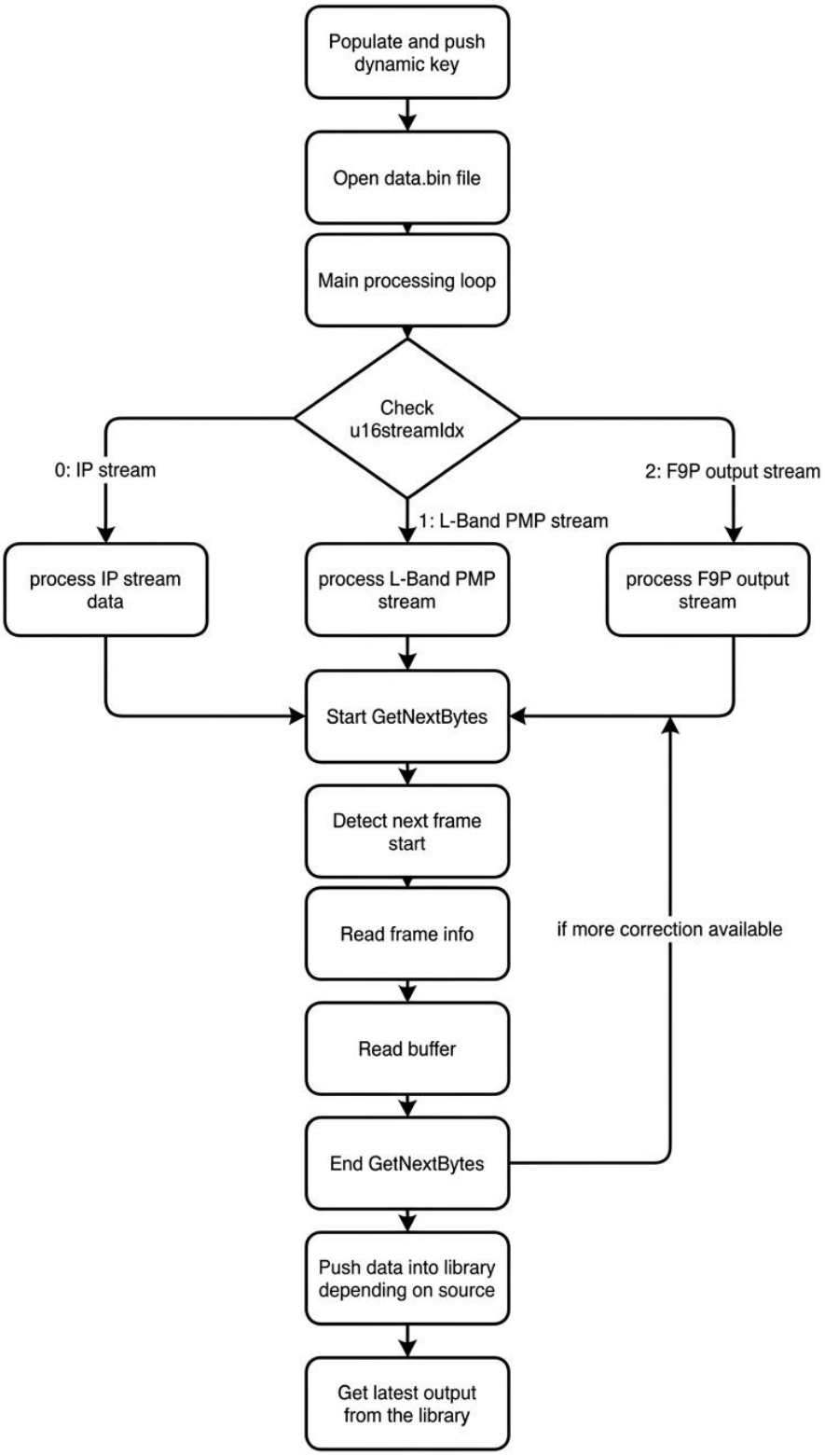


Figure 3.4: SPARTN correction decoding and processing workflow.

By adapting the correction service to the local environment, a high-quality representation of ionospheric and tropospheric gradients can be delivered. The u-blox SPARTN decoder provides a structured process to decode these complex corrections.

The software architecture that has been developed as part of this research, to utilise the SPARTN protocol, is based on the SAPALIB open-source software library. SAPALIB is an application-layer software framework that enables the transport, decoding and management of SSR (State Space Representation) correction streams as generated by a GNSS tracking receiver. The SAPALIB open-source software library is independent of this research and has been used as the interface to organise and access the SPARTN binary payloads prior to their utilisation within the positioning engines. To transform the received SPARTN messages to physical GNSS corrections that can be used by positioning engines, a SPARTN decoder was embedded in the framework. This decoder was initially developed by u-blox and was used as a starting point. Considerable work was, however, required to port the decoder to run within the RTKLib and YorkPPP frameworks. In particular, the output of the decoder was modified to better fit the structure of the observation models and the estimation used within the two positioning engines and developed the synchronisation protocols necessary to ensure the real-time SPARTN state vectors were correctly applied to the measurement epochs.

The encryption, along with authentication methods, protects the transmission of SPARTN correction streams, particularly when u-blox's PointPerfect service is used. The secure management of cryptographic keys marks the initial step of the decoding process. The decryption module becomes operational after receiving a dynamically populated decryption key, which unlocks the encrypted data stream. The decoder opens the SPARTN

data stream from the “Data.bin” file and in the first section of code, goes through three transport layer validation steps to ensure correct reception of the data. It identifies message boundaries using frame synchronisation, verifies data correctness using CRCs and then decrypts the payload using the correct keys.

After transport layer validation, the decoder determines the type of incoming stream. Although the SPARTN signal is versatile enough to support even complex precision applications, primarily L-band PMP (Radio) and IP-based data streams are processed within the high-precision SSR decoder. Upon detection of the incoming stream type, the decoder calls the StartGetNextBytes function to read the decoder’s input byte by byte. The byte is validated to determine if it is the start of a new frame, the contents of the buffer are read, and the byte is at the end of the frame is signalled to the software by the EndGetNextBytes function. The detected correction parameters are then fed into an SSR-compliant data structure within the decoder. For proper tracking and correlation with the GNSS observations, the decoder assigns precise time tags to the detected correction parameters. The decoder follows the instructions from the SPARTN Interface Control Document (ICD) to extract and process its essential message types. The Orbit and Clock Bias (OCB) message contains satellite orbit corrections, which start as radial along-track and cross-track components before the system converts them into Earth-Centred Earth-Fixed (ECEF) coordinates. The message contains exact satellite clock corrections along with precise signal biases which affect both code and carrier-phase signals. The High-Precision Atmospheric Corrections (HPAC) message delivers ionospheric and tropospheric delay corrections through gridded models. The Geographic Area Definition (GAD) message defines spatial model boundaries, which show how atmospheric correction

tiles should be structured and referenced throughout the spatial domain.

The decoded corrections from the library structure allow SAPALIB to generate the necessary parameters for precise point positioning (PPP). The precise satellite orbits are computed through the ComputeSatPrecOrbit function, which merges broadcast ephemeris data with the received orbit correction information. The ComputeSatPrecClock function produces precise satellite clock values through clock bias integration and relativistic compensation. The library extracts signal biases from the OCB (Orbit, Clock, Bias) message stream, which provides the necessary corrections for both code and carrier-phase measurements to ensure consistency in the positioning engine.

The ComputeSatIonoSlantDelay function uses the ion correction grid and satellite-receiver geometry to compute ionospheric slant delay corrections. The ComputeSatIonoSlantDelay function determines tropospheric slant delay corrections. The receiver-specific geographic location and observation geometry determine the delay corrections, which ensure proper signal propagation delay modelling. Figure 3.5 illustrates the details of correction integration and computation process performed by the high-precision SSR decoder within the SAPALIB.

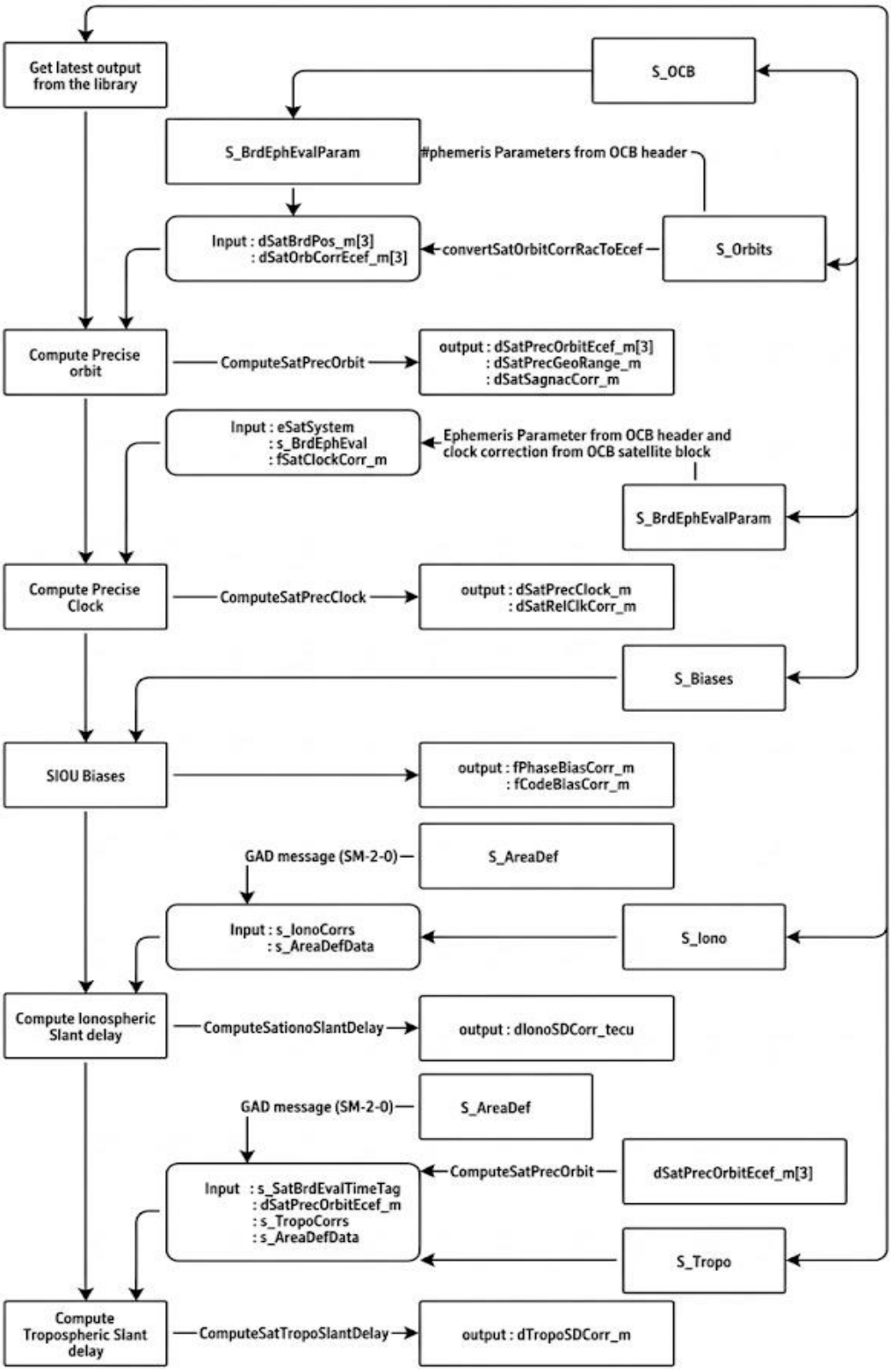


Figure 3.5: SPARTN correction application flow for precise orbit, clock, biases, and

atmospheric delay computation.

SAPALIB controls correction update, buffering and interpolation operations to preserve the continuous nature of corrections in time. The positioning accuracy requires this mechanism to function because signal interruptions happen in areas like urban canyons or tunnels. The library maintains the application of the most current valid corrections throughout GNSS observation interruptions. The corrections obtained from the library are provided to PPP processing engines like RTKLib or YorkPPP for integration with GNSS observations to produce accurate positioning solutions.

The SPARTN format provides security benefits in addition to its efficiency and accuracy capabilities. The new format enables digital signatures and key management functions to verify message integrity, while RTCM does not provide these security features. The secure modular design enables both real-time positioning at the centimetre level and provides a solid basis for future advanced GNSS applications such as autonomous navigation and safety-critical systems.

3.4.2 Correction Implementations in RTKLib

The implementation of corrections in RTKLib uses the State Space Representation (SSR) correction capabilities from RTKLib to process SPARTN data while maintaining RTKLib positioning workflows. The SPARTN decoder starts by processing the binary SPARTN stream through frame synchronisation followed by CRC checking and optional decryption for secure services. The decoder retrieves correction data from specific SPARTN messages such as Orbit and Clock Bias (OCB), High-Precision Atmospheric Correction (HPAC), Geographic Area Definition (GAD), and Bias and Phase Correction (BPAC) according to the SPARTN Interface Control Document (ICD). RTKLib stores the

decoded values in its internal ssr_t data structure that already contains orbit, clock, code bias, phase bias and atmospheric correction terms.

Figure 3.6 shows how the *satpos* function in RTKLib decides how to calculate satellite positions (*rs*) and clock corrections (*dts*), depending on the selected ephemeris and correction type, controlled by the *opt.sateph* parameter. The system selects *EPHOPT_BRDC* for standard broadcast ephemeris processing, which executes the *ephpos* function to obtain orbit and clock corrections from the navigation message. The system uses *satpos_sbas* to retrieve corrections from SBAS systems, WAAS and EGNOS when EPHOPT_SBAS is selected. These corrections enhance satellite orbit and clock precision for SBAS-compatible receivers.

RTKLib implements SSR corrections referenced to the satellite antenna phase centre through the option *EPHOPT_SSRAPC*. The *satpos_ssr* function receives execution after the *satpos_ssr* is invoked to apply SSR-based orbit and clock corrections. The *EPHOPT_SSRCOM* option follows the same method as *EPHOPT_SSRAPC* to use *satpos_ssr* with satellite centre of mass corrections. SSR data paths generate precise data, yet their reference point definitions affect the final positioning precision in critical applications.

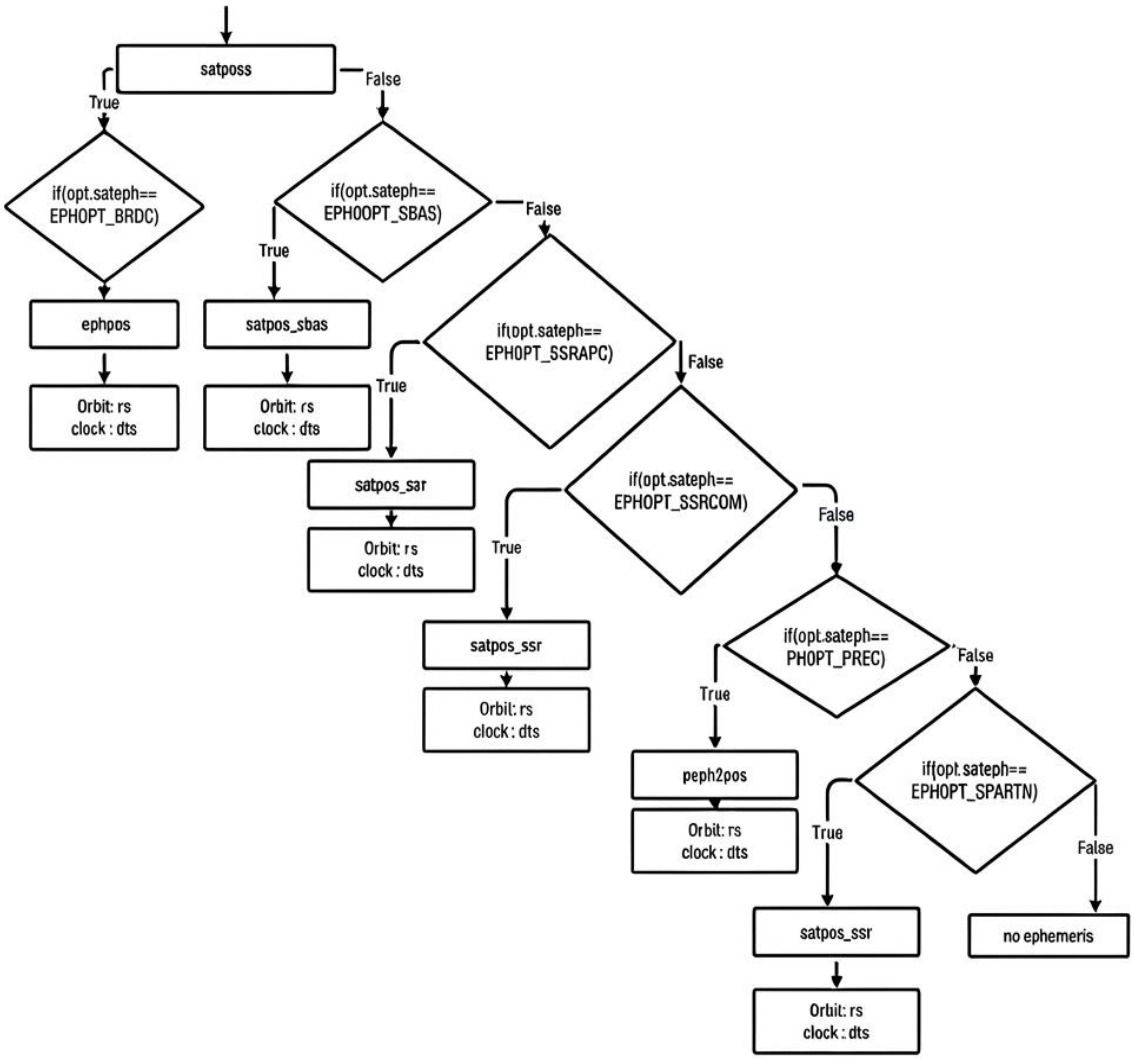


Figure 3.6: Ephemeris selection and orbit/clock correction logic in RTKLib, including SPARTN path.

The function *peph2pos* retrieves satellite positions and clock offsets from precise products after the user chooses *EPHOPT_PREC,* which represents IGS ultra-rapid or final SP3 data. The path functions for high-precision static and kinematic post-processing operations. RTKLib added the ability to process SPARTN correction data through its *EPHOPT_SPARTN* functionality. The *satpos_ssr* function receives activation from RTKLib for SPARTN-based satellite orbit and clock corrections when this option is chosen. The *corr_meas* routine handles bias corrections of code and phase biases for

SPARTN separately because these need proper application during measurement correction.

The system defaults to a "no ephemeris" state when it fails to detect the specified *opt.sateph* values. RTKLib uses its structured method to support multiple correction sources from traditional broadcast to advanced real-time SSR services, and it includes future standards like SPARTN. The *satpos* framework operates with a modular design which lets developers extend support for upcoming correction services while preserving the core logic functionality.

The correction modules are implemented inside the positioning engine as shown in the architectural flowchart in Figure 3.7. The logical flowchart in the rover configuration determines which of the correction parameters in the observation equations to apply. Even though SPARTN supports APC correction as well as phase windup, these can be disabled if the same effect has already been included in the broadcast SSR clock or in the bias corrections of the SSR of the service provider. Redundant corrections have a negative effect on the positioning accuracy as they cause the same geometric effect to be applied several times. This already is detrimental to the carrier-phase residual and the corresponding positioning accuracy.

When SPARTN corrections are enabled, the phase and code bias information from the messages is applied by using the *fPhaseBiasCorr_m* and *fCodeBiasCorr_m* parameters in the observation equations. If no SPARTN corrections are available or not selected to be used by the rover, the framework reverts to the conventional Differential Code Bias (DCB) correction models such as P1-C1 and P2-C2, which account for signal delays in the receiver’s hardware. In this case, the framework functions as a normal observation-space based positioning system as opposed to using State Space Representation (SSR) based

corrections as provided by the SPARTN service protocol.

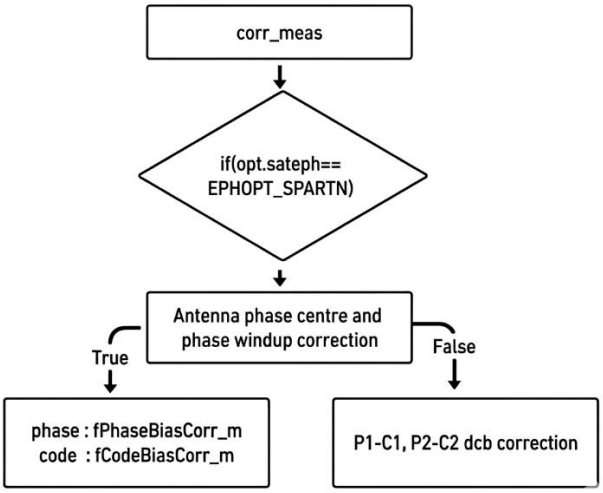


Figure 3.7: Measurement correction flow including SPARTN phase and code bias application.

The atmospheric correction process functions independently but maintains unified operations throughout the entire SPARTN correction pipeline. The ionospheric correction flowchart, as shown in Figure 3.8, demonstrates how the system applies *ComputeSatIonoSlantDela*y to calculate slant ionospheric delay when ion is set to *IONOOPT_SPARTN,* and the Geographic Area Definition (GAD) defined area remains valid. The positioning model utilises the ionospheric delay calculated as *dionoSDCorr_tecu*, which gets converted to metres into dion. The positioning model uses TEC maps, or Klobuchar model or SBAS ion as alternative models when SPARTN is not selected. The processing of tropospheric corrections involves running *ComputeSatTropoSlantDelay* when tropopt equals *TROPOPT_SPARTN* and the GAD area is valid; otherwise, RTKLib uses standard models (SBAS, SAAS or estimated models).

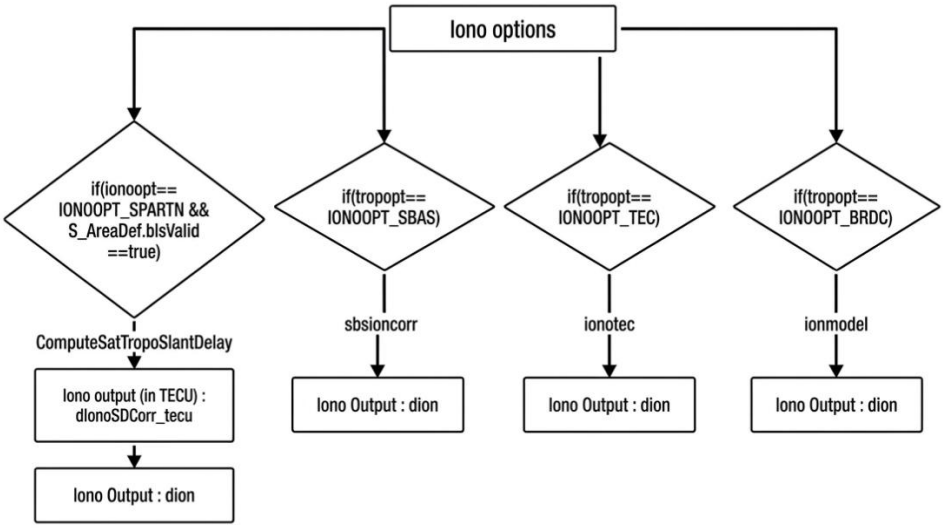


Figure 3.8: Ionospheric correction option flow including SPARTN, SBAS, TEC, and broadcast models.

Figure 3.9 illustrates the logic flow for tropospheric correction options within the GNSS positioning algorithm. Depending on the selected tropopt parameter, the system applies different models, such as SPARTN-based slant delay, SAAS, SBAS corrections, or estimation-based models, before producing the final tropospheric delay output (dtrp). The entire process pays specific attention to both the validity and the application scope of the corrections. RTKLib checks the user's location against Geographic Area Definition (GAD) messages from SPARTN to determine if atmospheric corrections based on High Precision Atmospheric Correction (HPAC) should be applied. RTKLib needs to handle Earth tides and phase wind-up according to SPARTN conventions, these require special care to maintain compatibility with RTKLib core processing. The system applies necessary modifications to either the *ssr_t* structure mapping or correction application routines to maintain model consistency with SPARTN-specific models.

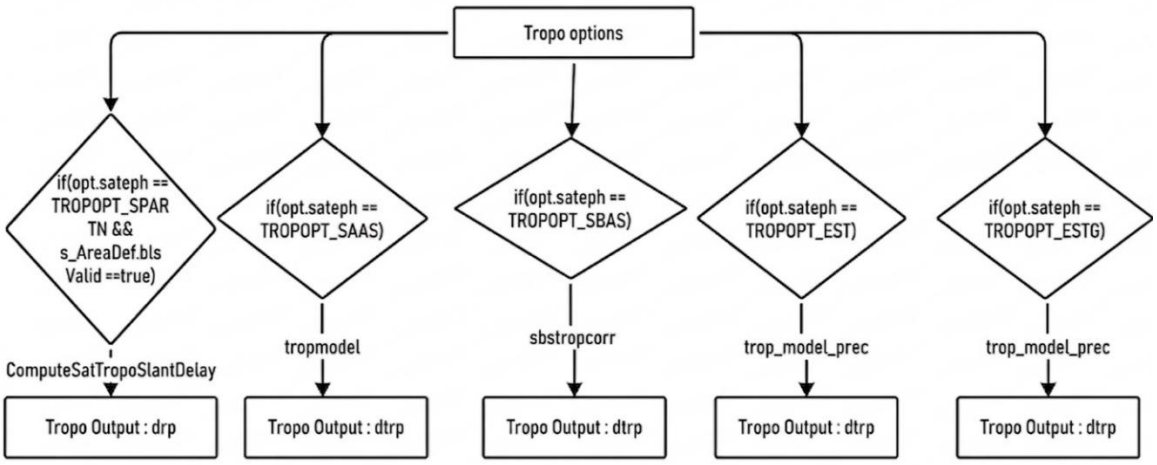


Figure 3.9: Tropospheric correction option flow including SPARTN, SBAS, SAAS, and estimated models.

The integration of SPARTN within RTKLib makes use of the library's modular SSR infrastructure design. The decoder interfaces with the satpos_ssr function to get the SSR time information, the corr_meas function to process the correction measurements, and the atmospheric correction functions to utilise the precise corrections in RTKLib's internal positioning algorithms. This implementation maintains RTKLib's adaptability and scalability capabilities by fully utilising SPARTN's bandwidth-efficient and precise correction signals.

3.4.3 Correction Implementations in YorkPPP

SPARTN corrections integrated into the YorkPPP engine require systematic modification of both input parsing systems and core correction algorithms to achieve precise real-time and post-processed GNSS positioning accuracy. York University’s GNSS laboratory developed YorkPPP, which functions as a precise point positioning engine to achieve high accuracy ambiguity resolution. The engine needs to expand its file reading process and modify its calculation process to handle SPARTN models, while ensuring

compatibility with the distinctive SPARTN format structure. Figure 3.10 illustrates how SPARTN corrections receive similar processing as other SSR-based formats like HAS and PPPwiz. The *readSPARTNheader()* and *readSPARTNcorrection ()* functions process these corrections after reading the SP3 and broadcast navigation files. The *readSPARTNheader ()* function deals with metadata parsing before the correction loop calls *readSPARTNcorrection ()* to process GNSS observation data alongside SINEX biases and auxiliary corrections.

In illustrated in Figure 3.10, the input data streams are first decoded and corrected. They are then input into the Precise Point Positioning (PPP) estimation engine. The standard broadcast ephemeris and clock data are corrected using State Space Representation (SSR) correction streams. Such corrections enhance the positioning accuracy, solution reliability and convergence performance of the positioning system. For high-precision positioning and ambiguity resolution, State Space Representation (SSR) is used for the orbit and clock as well as for code and carrier-phase bias correction, the latter modelling signal-dependent hardware delays. In addition, regional atmospheric corrections are provided and applied within the observation modelling step, such as the High Precision Atmospheric Corrections (HPAC) for ionospheric and tropospheric delay. Throughout the implementation, standardized SSR terminology as well as SPARTN terminology is used, corresponding to the widely accepted GNSS correction nomenclature and open formats.

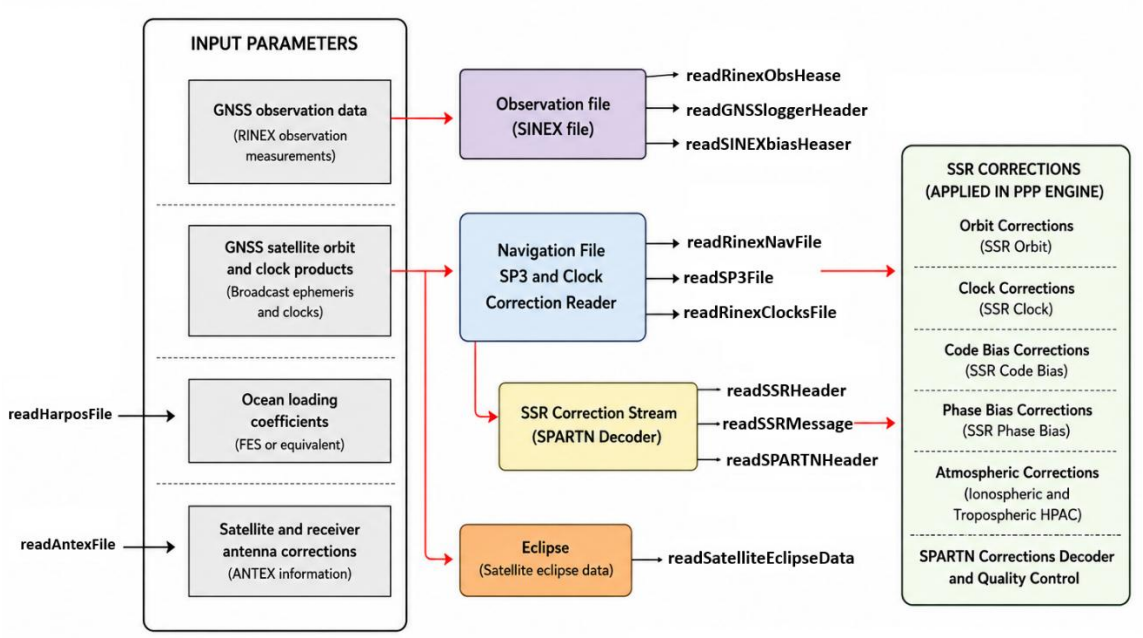


Figure 3.10: Correction data flow in the YORKPPP software. Multiple correction sources (orbit, clock, biases, antenna, and atmospheric) are integrated through dedicated input modules to support precise positioning.

The decoder needs to read every SPARTN message type, such as Orbit, Clock, and Bias (OCB), which contains orbit and clock and bias information and High Precision Atmospheric Correction (HPAC) for high precision atmospheric corrections and Geographic Area Definition (GAD) for grid area definition. The transport layer undergoes processing through frame boundary detection, along with CRC validation and active encryption decryption. After validation, the decoder employs bitwise decoding as described in the SPARTN Interface Control Document (ICD) to retrieve satellite specific information such as extract satellite-specific orbit deltas (radial, along-track, cross-track), precise clock offsets, and code/phase signal biases from validated messages. All extracted parameters are stored into an SSR like data structure time tagged to the time of decoding, in the same manner as received messages.

The processing architecture for position estimation is based on a bidirectional processing approach, denoted as forward and backward processing, as illustrated in Figure 3.11. Forward processing is like real-time processing in which observations, including corrected GNSS signals using SPARTN corrections, are processed in a order to estimate the receiver state at each processing epoch. In backward processing or post-processing smoothing, the data is processed in reverse chronological order to smooth the previously estimated states and to improve the accuracy of the trajectory solution. The forward processing using SPARTN corrections is a real-time application, whereas the backward smoothing pass can be used to compute the maximum possible positioning accuracy and to verify the consistency of estimated states computed during forward processing.

Process noise is introduced into the processing model at the prediction step for each state, prior to the sequential least-squares update. This allows for the modelling of temporal changes in the dynamic parameters of interest, such as the receiver clock, as well as the variability in the atmospheric signals. Introducing process noise at the prediction step rather than at the update step, for example as is typically done in Geodetic quality positioning using GNSS only, prevents the filter from becoming over-constrained by the information from previous updates, thereby ensuring that the filter remains adaptive and responsive to the quality and quantity of available information. In this regard, the stochastic modelling component of the filter architecture plays a critical role in the overall estimation accuracy and robustness of the solution.

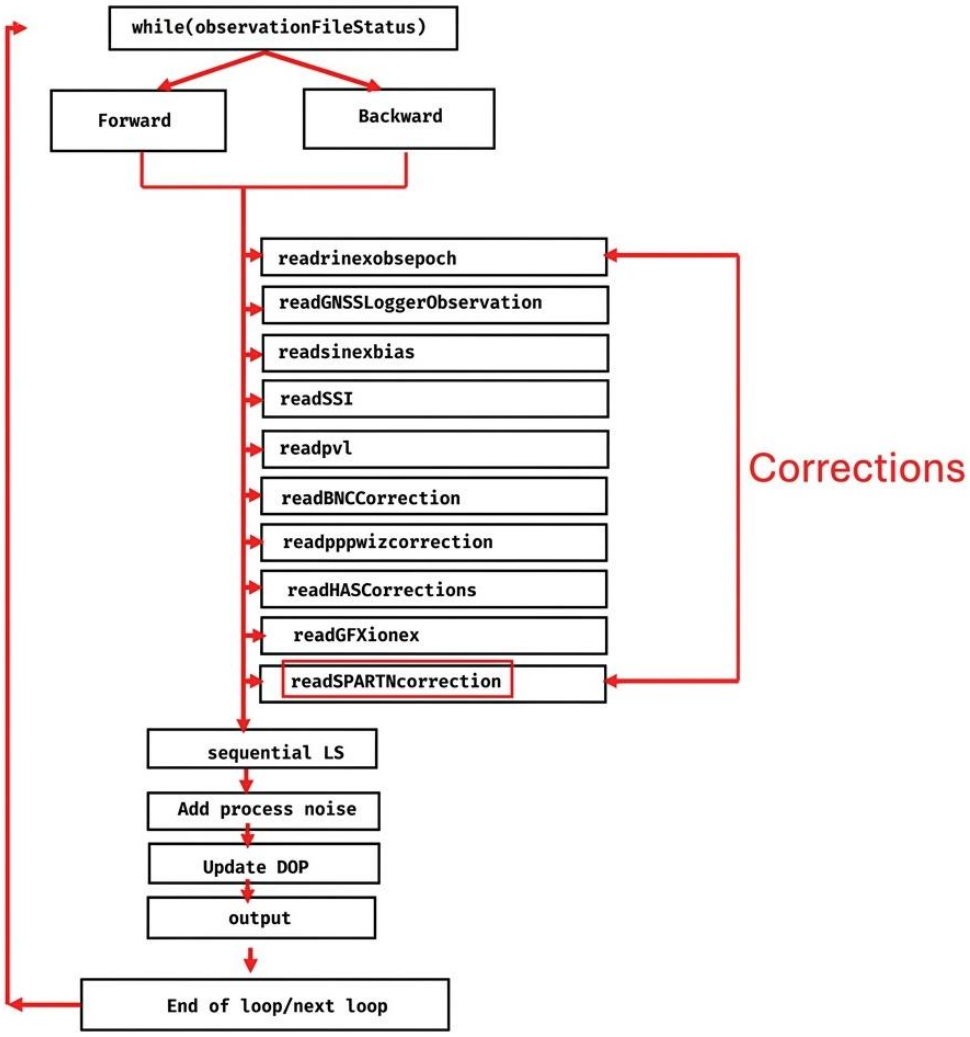


Figure 3.11: Correction application loop in the YORKPPP engine. Multiple correction sources are integrated within the forward and backwards processing loop to support sequential least-squares positioning.

SPARTN-derived ionospheric and tropospheric corrections function as pseudo-observations for atmospheric modelling. The ionospheric correction must receive weighting between pseudorange and carrier-phase measurement levels since it constrains the model's ionospheric state. The estimation of differential code biases (DCB) at the receiver must be done carefully to prevent systematic offset creation from ionospheric

constraints. The implementation of tropospheric delays either uses them to directly substitute the estimated state vector parameter or to constrain state vector estimation through residual modelling. The system follows Grid Area Definition (GAD) message-defined spatial validity rules, which determine when corrections should be applied to valid grid areas. Figure 3.12 illustrates how YorkPPP integrates SPARTN corrections through its error correction modules.

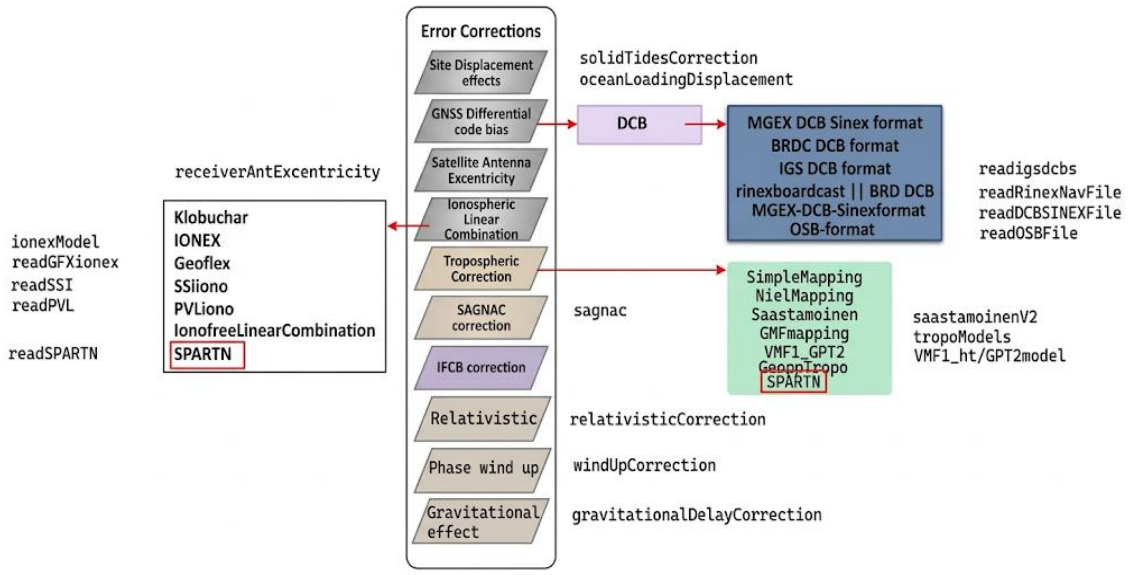


Figure 3.12: Implementation of additional error corrections in the YORKPPP engine. SPARTN-based ionospheric and tropospheric models are integrated alongside existing models to enhance positioning accuracy.

Special consideration is required for model compatibility. The conventions used by SPARTN in its operations differ from standard PPP practices because of differences in reference frames (e.g., SF009 field), Earth tide modelling, satellite yaw, and phase wind-up correction methods. The SPARTN correction uses a zero-yaw wind-up correction approach, which diverges from conventional practices that use explicit satellite attitude modelling. YorkPPP needs to modify its phase wind-up and tidal displacement models to

prevent positioning errors from occurring. The adjustments are added to either the preprocessing step or to the estimation models when SPARTN stands as the identified correction source.

The YorkPPP engine uses its Decoupled Clock Model (DCM) together with its ambiguity resolution framework, which makes it suitable for SPARTN integration. The DCM produces single-differenced ambiguities that contain minimal biases, while the modified mLAMBDA algorithm of YorkPPP maintains effective ambiguity resolution capabilities when SPARTN biases are applied. The tuning of thresholds and quality control metrics, such as ambiguity validation ratios and continuity checks, might require adjustment to handle SPARTN's varied quality indicators and update periods.

YorkPPP maintains its core abilities to process dual-frequency GPS and Galileo signals while applying necessary relativistic and Sagnac corrections, together with wind-up and gravitational corrections and using elevation-weighted least squares estimation. Figure 3.12 demonstrates that SPARTN-based models work in parallel with existing models, including Klobuchar and IONEX and Geoflex through runtime selection logic (e.g., readSPARTN).

Finally, comprehensive validation is essential. The implemented corrections, along with models, require testing against accurate high-precision reference solutions, while diagnostic analysis of residuals will confirm SPARTN's corrections properly match measured observations. The optimal model behaviour and weighting can be verified through sensitivity tests, which involve enabling and disabling ionospheric pseudo-measurements.

The current infrastructure at YorkPPP will support all modern SSR-based corrections

through the integration of SPARTN decoding and correction models. The integration will enhance the ability of YorkPPP to provide real-time, high-accuracy positioning in bandwidth constrained or encrypted environments.

3.4.4 Data used

In this research, SPARTN corrections were evaluated using two different positioning engines: the popular open source RTKLib engine, and the research grade YorkPPP engine. In addition, PPP corrections were established using Centre National d'Études Spatiales (CNES) ultra-rapid products to serve as a baseline for comparison against the SPARTN corrected data.

The RTKLib engine was set up to retrieve SPARTN corrections using the secure STRSTR function supplied by Thingstream to handle authentication and streaming of the real time corrections from the server. The correction stream was recorded for later reference. The same data stream was then input into YorkPPP and a fair comparison made between the two software packages.

The SPARTN stream delivers standardized, precise orbit and clock corrections, signal biases, and high-resolution atmospheric data. The SAPALIB library is utilised to extract these corrections from the binary messages and convert them into RTKLib's internal SSR (State Space Representation) structures for positioning calculations.

The performance evaluation presented here targets some of the stations in the North American coverage of the SPARTN service. The evaluations follow the SPARTN ICD models and specifically focus on the performance with respect to reference frame modelling and atmospheric modelling.

SPARTN users undergo user-side processing utilising dual-frequency GNSS data

(L1/L2) from all operational constellations (GPS, Galileo, GLONASS, BeiDou) for comparison. All testing utilises IGS tracking data, all processing undertaken with a constant elevation angle cut-off and recovered data utilised under the exact same conditions. This ensures for a fair and definitive comparison of SPARTN corrections against alternative PPP correction sources.

The hardware configurations used throughout this research are summarized in Table 3.1. Detailed descriptions of the rooftop, IGS, and kinematic experimental setups are additionally provided in the corresponding sections of Chapters 4 and 5, along with the associated figures and data collection descriptions.

Table 3.1: Horizontal and vertical positioning error statistics for SPARTN and CNES corrections during the kinematic GNSS test.

Test Configuration	**Hardware / Platform**
Rooftop Static Test at York University	NovAtel geodetic antenna, NovAtel SPAN (OEM7) receiver, u-blox F9P antenna, and u-blox Spark Fun receiver
QUIN IGS Static Test	QUIN IGS reference station equipped with ASH701945E_M antenna and geodetic-grade receiver infrastructure
Kinematic Vehicle Test	Vehicle-mounted NovAtel antenna, u-blox F9P antenna, NovAtel OEM7 receiver, and integrated IMU system and u-blox Spark Fun receiver

4.Experiments and Analysis from RTKLib

To assess the effectiveness of applying SPARTN corrections in RTKLib processing software, two data collection scenarios were used. The first scenario involved a static setup, where data were collected using a geodetic receiver, which is placed on a rooftop for approximately 8 hours a day over 5 days in August 2024. Figure 4.1(a) shows the placement of a geodetic NovAtel antenna on the rooftop for the experiment. The PPP static scenario also involved processing data from 4 different IGS stations over 24 hours for 5 days in August 2024.

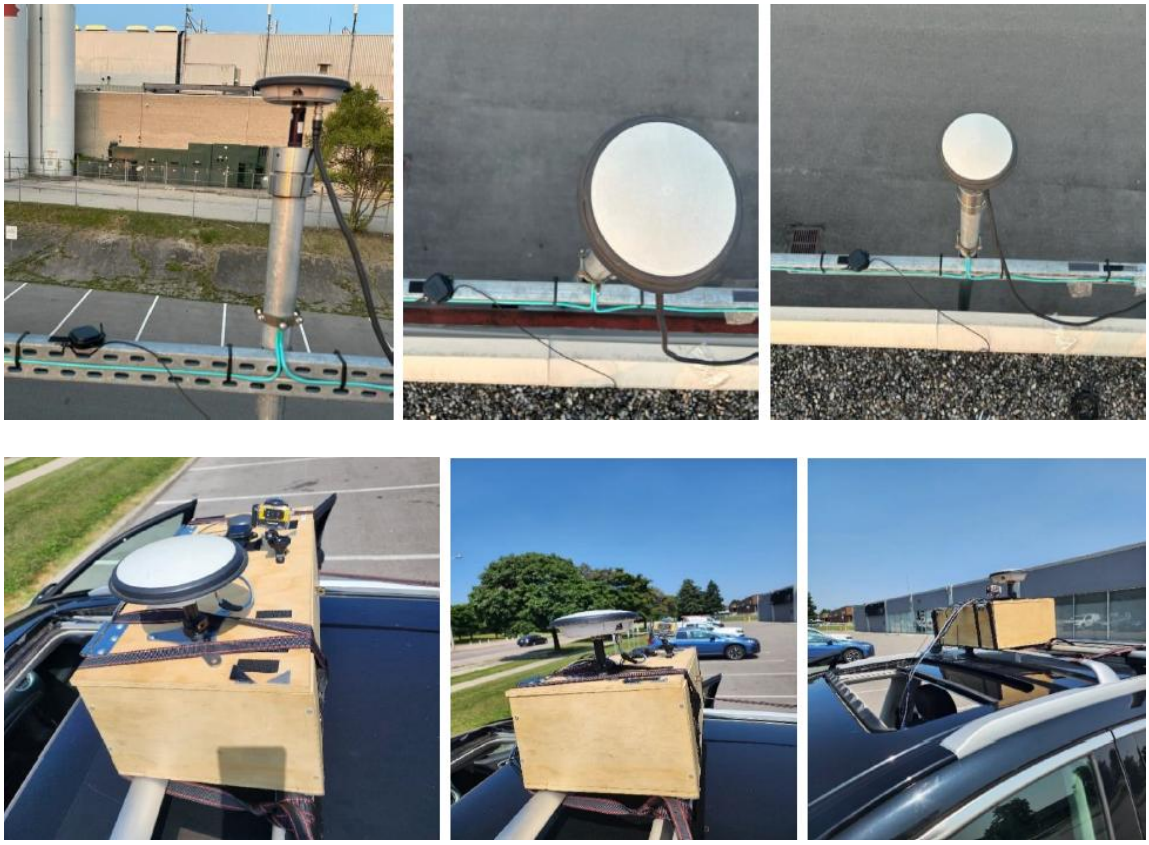


Figure 4.1: GNSS data collection setups used in this study. (a) A reference station installed on the rooftop of 4751 Keele St, York University, providing high-quality static

observations for reference trajectory generation. (b) Kinematic test platform mounted on a vehicle roof, used to collect GNSS data for evaluating positioning performance under dynamic conditions.

The second scenario consisted of four dynamic vehicle tests conducted in the vicinity of York University in Toronto, Canada. These data collections were performed intermittently throughout August and September 2024 to evaluate and compare positioning performance in kinematic mode. For these experiments, the test vehicle was equipped with a NovAtel SPAN (OEM7 + IMU) system integrated with a geodetic-grade antenna. The antenna was roof-mounted to serve as the rover, as illustrated in Figure 4.1(b). To provide a representative example of the operational environment, Figure 4.2 displays the trajectory from the kinematic GNSS test conducted on September 9, 2024 (DOY 253), highlighting the diverse signal conditions encountered around York University.

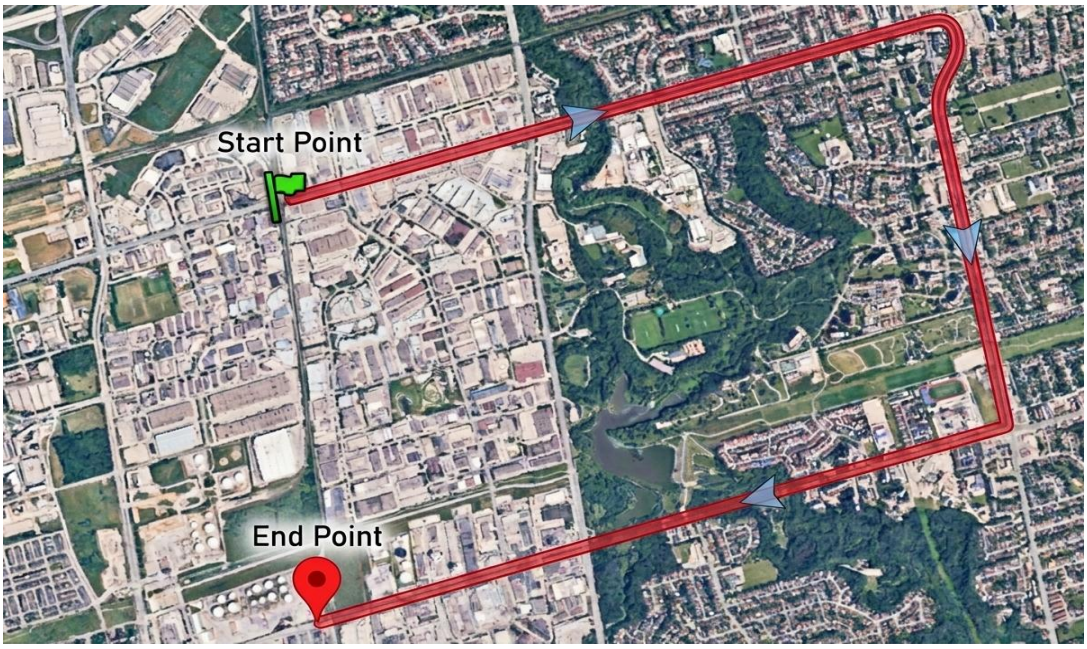


Figure 4.2: Kinematic GNSS test trajectory conducted around York University campus and surrounding area. The vehicle followed the indicated loop route, starting and ending at

designated points, to evaluate positioning performance.

In the experimental validation of SPARTN correction performance within different application environments, the rooftop static test was designed to test the robustness, reliability and consistency of correction in favorable GNSS observation conditions. To test the convergence behaviour, the positioning accuracy, the type of ambiguity resolution and the performance differences of low-cost receivers in comparison to survey-grade receivers, the test was carried out on a rooftop in open-sky conditions with minimal signal blockage and multipath interference, by using both low-cost and high-grade GNSS receivers.

For the QUIN IGS station experiment, a geodetic reference frame of highest quality using the high precision continuously operating reference stations (CORS) of the IGS was established. By this, the spatial and temporal behaviour of the corrections as well as the performance of the atmospheric modelling can be checked against a well established reference. In contrast to this, the kinematic vehicle experiment simulated a dynamic urban navigation environment with signals being blocked by buildings, with multipath, with a highly variable satellite constellation and with cycle slips that occur in practically used systems.

By demonstrating consistent positioning performance trends across static, geodetic reference, and dynamic urban environments, the experimental results provide strong evidence that the proposed SPARTN integration framework is robust, reliable, and suitable for deployment across diverse operational conditions.

4.1 PPP-Static Performance Analysis: York University

GNSS positioning accuracy tests using SPARTN correction service were performed to evaluate baseline performance against CNES precise products data on DOY 223, 2024

(August 10, 2024). The aim of this test was to evaluate differences in correction performance before ambiguity resolution i.e. using float solution. GNSS receiver tracking GPS, GLONASS, Galileo and BeiDou signals on L1/E1/B1 and L2/E5b/B2 bands operated continuously on the rooftop of York University during the test period.

4.1.1 Empirical Validation of Geodetic-Grade Hardware Performance

The signal quality analysis showed that all satellite signals maintained reliable tracking performance with C/N_0 measurements between 45 to 55 dBHz, especially for satellites that had high elevation angles and decrease due to interference from atmosphere and multipath at low elevations. To assess the quality of received GNSS signals during the observation period, the signal-to-noise ratio (SNR) values were analysed. Figure 4.3 presents the SNR variation over time for different satellite signals, highlighting fluctuations due to environmental obstructions, multipath effects, or atmospheric conditions. Variation in SNR for GLONASS signals was found to be more critical mainly due to lower signal intensity and more fluctuations as compared to signals from GPS and Galileo constellation specifically on L2/E5b/B2 frequency band.

The data shows a tracking threshold which is implemented in a mask at around 15° to prevent data issues caused by extreme multipath and atmospheric noise. As can be seen by the correlation between the two plots, the satellites reaching 'near-zenith' (80° - 90°) have the highest signal quality. As the satellites drop in elevation toward the 15° limit of the rooftop, the SNR values drop in a manner consistent with expectations based upon standard atmospheric absorption and the geometry of the pass rather than any significant local structures obstructing the antenna view.

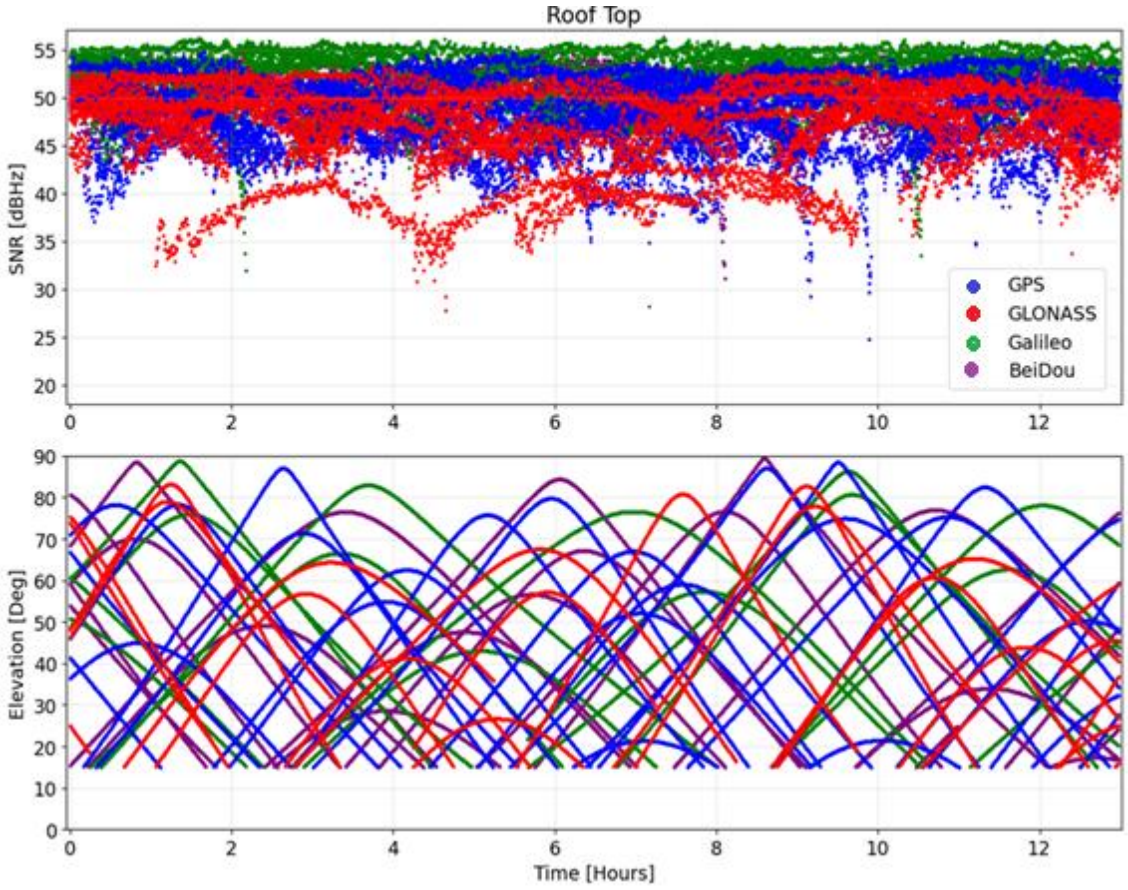


Figure 4.3: Signal-to-noise ratio (SNR) variation over time for GNSS observations. The different colours represent signals from various constellations, showing relative signal strength and elevation throughout the observation session on DOY 223, 2024.

For static test session on DOY 223, 2024., the satellite skyplot in Figure 4.4 displays the GNSS signal coverage overtime. The entire observation period is shown through coloured arcs, which represent GPS (blue), GLONASS (green), Galileo (pink) and BeiDou (purple) satellite tracks. The receiver tracks individual satellites through their sky movements relative to its position.

The receiver obtained outstanding multi-constellation visibility through its wide distribution of satellites, which covered all azimuth directions and elevation levels. The combination of high- and low-elevation satellites enhances satellite geometry, which leads

to better positioning accuracy by reducing DOP values, a dimensionless factor that describes the geometric strength of the satellite configuration. According to Misra and Enge (2011), DOP acts as a "magnifier" of underlying measurement errors ($Error = DOP\ x\ \sigma_{UERE}$).

Good geometry helps the PPP filter more accurately estimate position, tropospheric delay, and ambiguities. The diverse satellite geometry plays a crucial role PPP because it allows the PPP filter to solve ambiguities and determine atmospheric delays effectively. The satellite geometry observed during the test period enabled a robust PPP solution performance, which resulted in the high positioning accuracy achieved during this test.

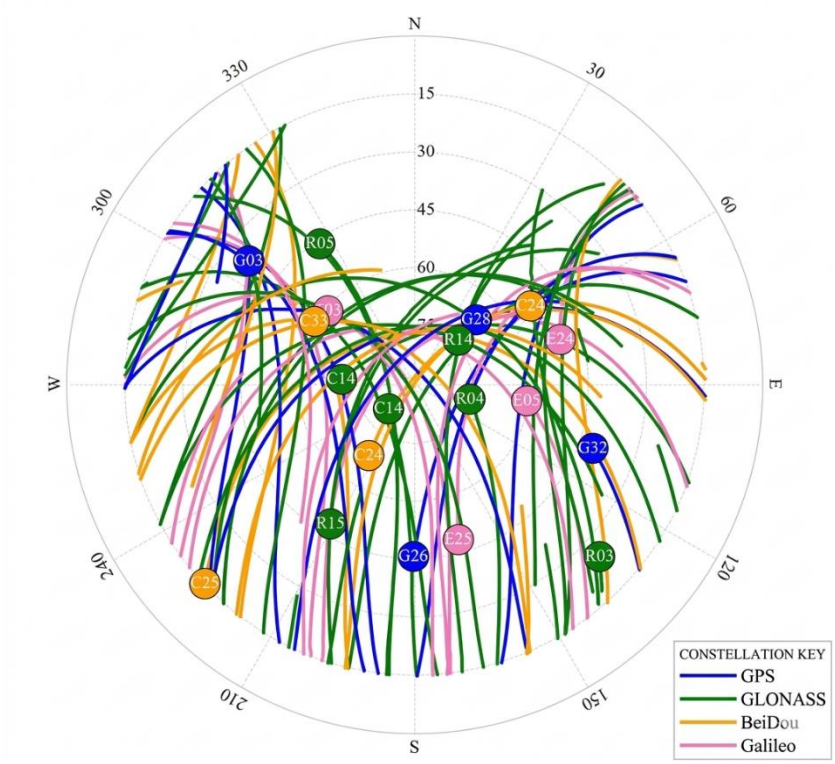


Figure 4.4: Skyplot of GPS (blue), GLONASS (green), Galileo (pink), and BeiDou (orange) satellite tracks during the static test on DOY 223, 2024, showing strong multi-constellation visibility and favourable geometric coverage.

The comparison of positional accuracy from using CNES and SPARTN corrections is

shown in Figure 4.5. The solution based on CNES data achieved faster convergence while maintaining better long-term stability for both horizontal and vertical position measurements. The position accuracy of the CNES corrections reached 0.09 metres RMS for horizontal and 0.06 metres RMS for vertical positioning, with 97% of position data within the 10-centimetre threshold. The horizontal RMS error of SPARTN corrections measured at 0.13 metres, and vertical RMS error reached 0.25 metres while position accuracy below 10 centimetres was achieved for 90% horizontal and 72% vertical epochs. The PPP processing revealed standard convergence patterns which demanded 30 to 60 minutes of float ambiguity resolution and atmospheric delay modelling before achieving accurate results. The CNES solution maintained faster convergence rates, while displaying lower variability than the entire test period. The vertical positioning accuracy maintained consistently worse results than horizontal accuracy for both correction services because GNSS satellite constellations inherently suffer from higher vertical dilution of precision.

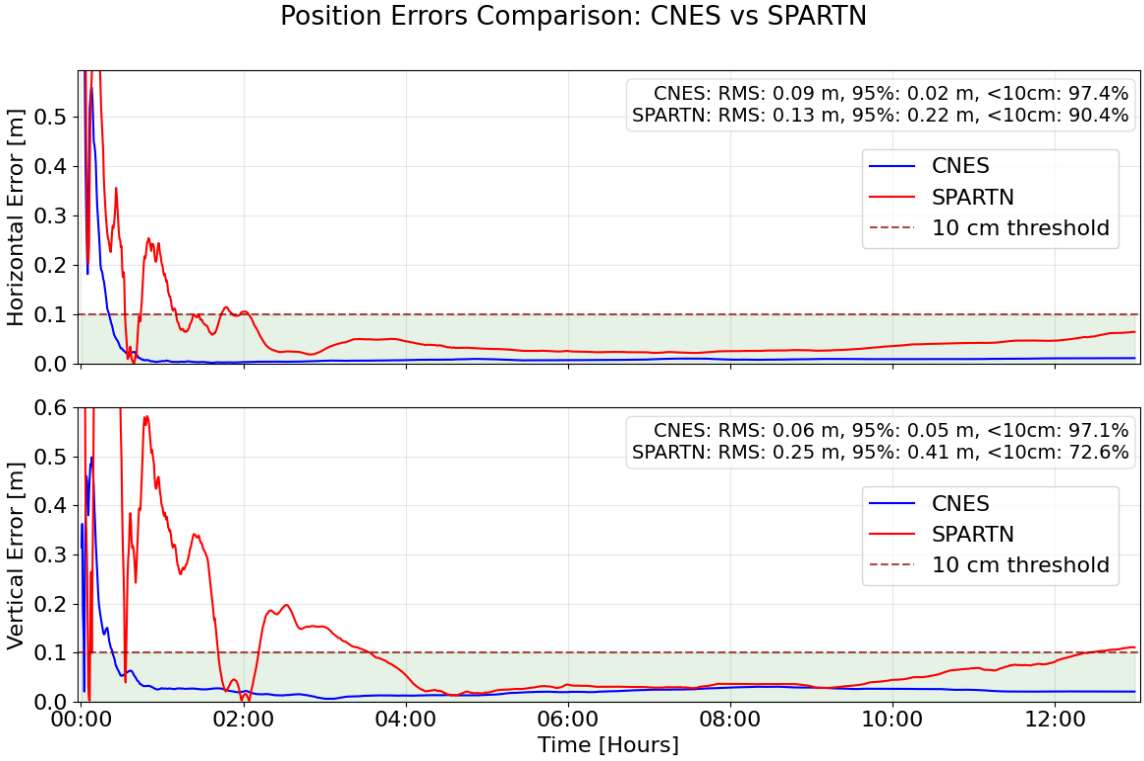


Figure 4.5: Horizontal and vertical position error comparison between CNES and SPARTN corrections in RTKLib float solution on DOY 223, 2024.

The ENU coordinate analysis depicted in Figure 4.6 demonstrates how these performance differences manifest. The CNES correction data have an RMS error of 0.08 m east and 0.03 m north and 0.06 m up. More than 97% of all epochs achieved better than 10-cm three-dimensional positioning. For the SPARTN solution, the east component is best at 0.08 m RMS, the north component is fair at 0.10 m RMS, and the up component is poor at 0.25 m RMS. Note that less than 72% of all epochs reached sub-decimetre three-dimensional positioning. These results indicate that SPARTN positioning performance equals that of the CNES data in competitive scenarios that feature adequate satellite visibility and good atmospheric modelling performance. However, the vertical component of static solution performance is much worse than CNES. The main reason for this is that CNES uses its global tracking network to achieve high quality, long arc orbit solution determination, in addition to its accurate tropospheric modelling performance. In contrast, the regional approach used by SPARTN to process the large amount of SSR data requires the use of reduced data streams and simpler regional grids to achieve real-time processing performance objectives. These data reduction schemes introduce greater-than-average modelling residuals and vertical dilution of precision (VDOP) performance amplification into the SPARTN solution.

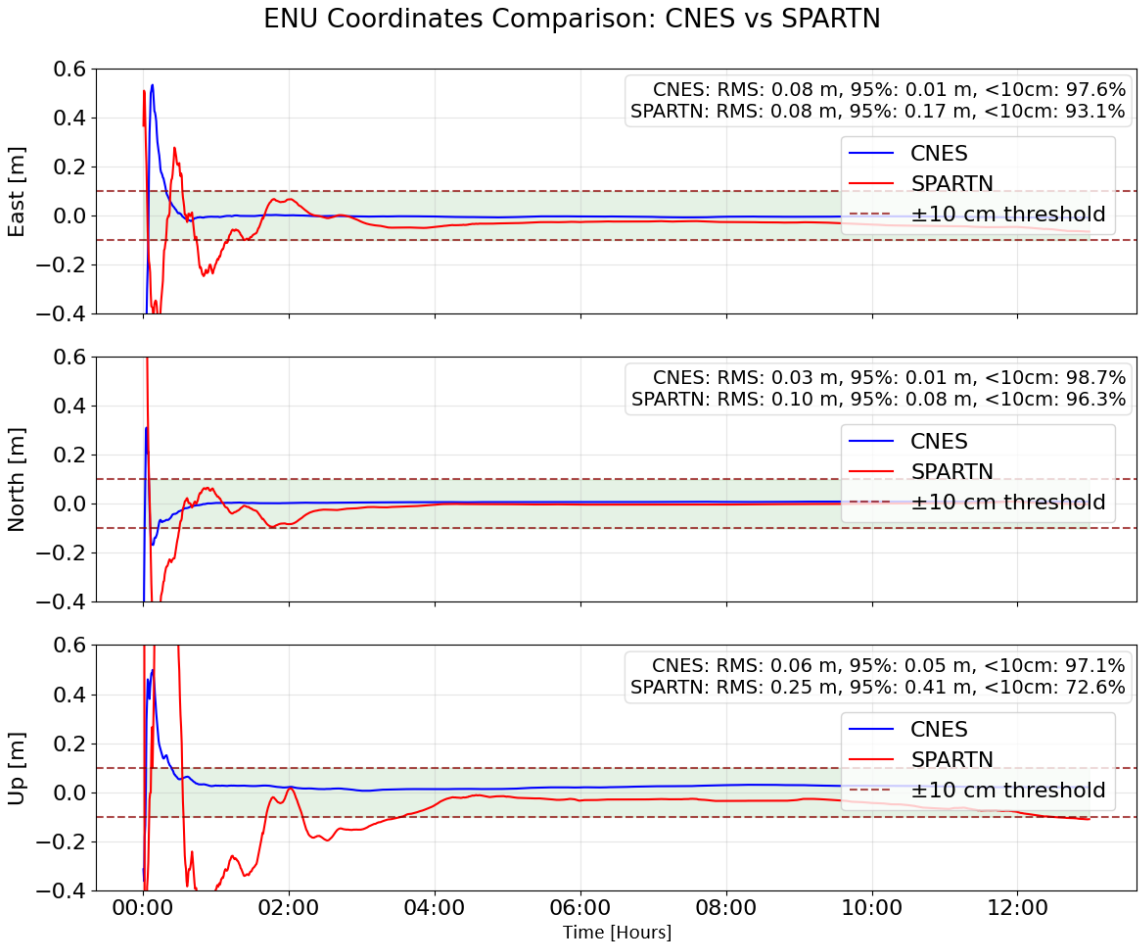


Figure 4.6: Time series of east-west, north-south, and up-down position errors during the static GNSS test conducted on DOY 223, 2024. The blue line represents the solution using CNES corrections, while the light red line corresponds to the solution using SPARTN corrections on DOY 223, 2024.

For the SPARTN float solution, there is significant asynchrony between the Orbit, Clock, and Bias (OCB) message availability and the High Precision Atmospheric Correction (HPAC) message availability. For the tracked constellations, the OCB corrections are available for most of them, but the HPAC messages are available for only a smaller subset of satellites within the local Geographic Area Definition (GAD) grid for the current float solution. This results in many healthy satellites not being included in the

PPP filter to utilise the most recent atmospheric data. As a result, poor satellite geometry (high DOP) is achieved and there are large switches in the number of satellites in the lock for the different constellations. As a result, the overall PPP performance is only 0.25 m RMS for the up component and is quite unstable in this direction in contrast to more global CNES results that include a larger number of satellites in their solution.

It is common practice to correct for a number of the "invalid" corrections for the many definitions of the visible constellation of satellites used by the PPP system. As a result, the PPP solution frequently switches between different groups of satellites in view. This rapid switching produces two sources of degradation in the SPARTN solution. Firstly, every satellite that goes from "visible" to "not visible", or from "not visible" to "visible", transits from being tracked continuously by the receiver and thus receives a "jump" in the Kalman filter state as the DOP rapidly changes. Additionally, the filter must resort to poorer quality fallback models (e.g. Klobuchar) for satellites that remain in view but do not have an available High Precision Atmospheric Correction (HPAC) for the current location, resulting in greatly increased errors for atmospheric propagation. Together, these effects preclude the SPARTN solution from obtaining the same geodetic stability as the global CNES baseline. The resulting ENU time series display pronounced oscillations. Performance in vertical position is mainly limited by differences in how atmospheric delay is modelled between SPARTN and CNES. Note that SPARTN uses regional atmospheric corrections based on the ionospheric and tropospheric models (contained within HPAC messages) therefore some regional grids will have no data or be flagged as bad data. Although data may be available globally, the SPARTN solution will not be as continuous as the CNES solution therefore VDOP will be higher than CNES and the filter will not

decouple station height from the other atmospheric parameters. The float solution has a vertical RMS of only 0.25 m and is rather unstable. SPARTN-aid solution displays "pockets" of some fragmentation in elevation arcs, but generally good performance.

Figure 4.7 shows the reason for some of the "pockets" of poor performance is lack of correction data and not physical signal blocking. SPARTN requires two conditions to be simultaneously true: (1) Orbit, Clock, and Bias (OCB) global corrections are valid, and (2) High Precision Atmospheric Correction (HPAC) regional messages are valid. Regional atmospheric modelling for a particular Geographic Area Definition (GAD) grid fails to meet the specified confidence for a satellite and is marked as "invalid". This frequent change in satellite subset for a given area can cause jumps in the filter state leading to vertical instability (Misra & Enge, 2011). The elevation plot is currently missing BeiDou constellations. This is due to BeiDou related messages being flagged as invalid within the SPARTN correction stream, preventing the receiver from processing the satellite data.

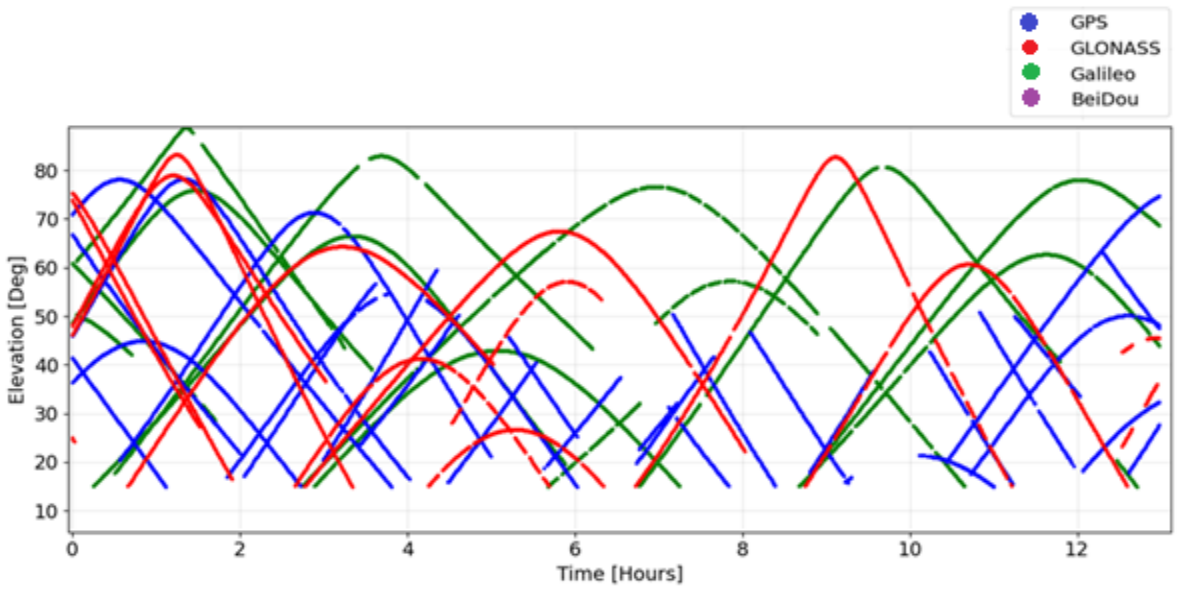


Figure 4.7: Satellite elevation angles over time for Global Positioning System (blue),

GLONASS (red), Galileo (green), and BeiDou Navigation Satellite System (purple) signals during the static GNSS test conducted on DOY 223, 2024.

Unlike the previous plot, Figure 4.8 shows the system state when correction data is invalid or missing. The sparse tracks for BeiDou and Galileo illustrate that while the satellites are geometrically visible, they are functionally unavailable. SPARTN stream flagged these constellations as invalid as the HPAC regional messages failed to meet the specified confidence for the current Geographic Area Definition (GAD) grid. This frequent and abrupt change in the usable satellite subset is a primary driver of filter instability and degraded positioning accuracy.

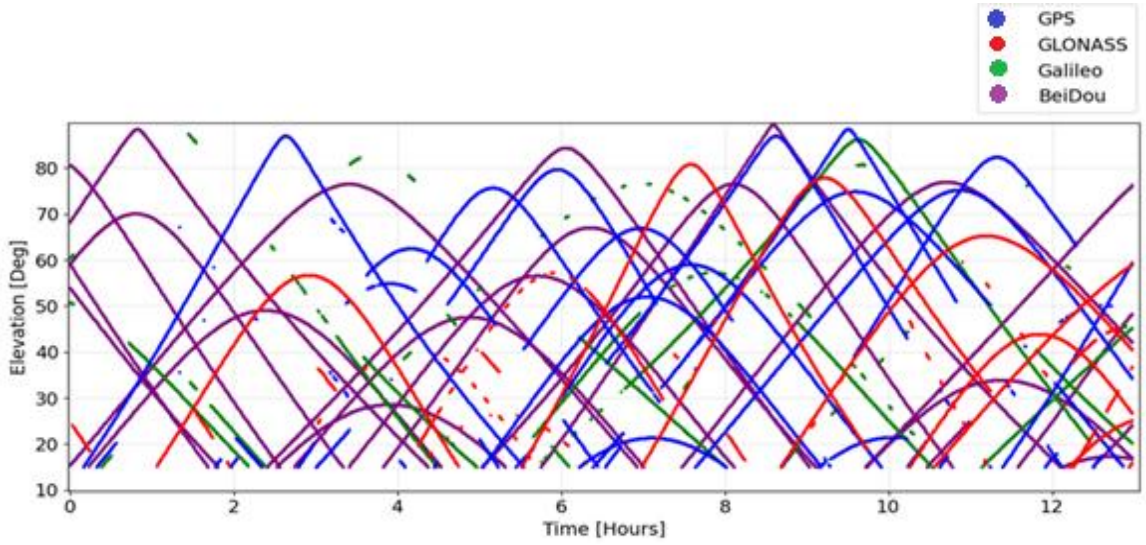


Figure 4.8: Elevation plot illustrating fragmented satellite visibility tracks caused by periods of invalid SPARTN corrections during the static GNSS test conducted on DOY 223, 2024.

The signal quality analysis in Figures 4.9 and 4.10 demonstrates the expected elevation-dependent SNR patterns, where signal strength increases as satellites move toward the zenith. The plots show an elevation-dependent SNR, increasing for satellites ascending towards the zenith. All systems show good signal quality with high stability and

high-power levels at high elevation angles, ranging from 45 to 55 dBHz. However, the SNR of GLONASS signals (red dots) is generally lower and shows higher scatter than for GPS and Galileo, especially at low elevation angles. This is due to the higher noise floor and inter-frequency biases introduced by the GLONASS Frequency Division Multiple Access (FDMA) architecture as described in Hofmann-Wellenhof et al. (2008). The increased noise at low elevation angles in conjunction with the 'invalid' atmospheric correction gaps shown in Figure 4.10 makes it difficult for the filter to maintain a weight for these satellites. This lower SNR for GLONASS, particularly for the L2/E5b/B2 band, then further decreases the vertical stability of the SPARTN solution as the filter must rely on noisier measurements for satellites that already experience outages for regional atmospheric modelling.

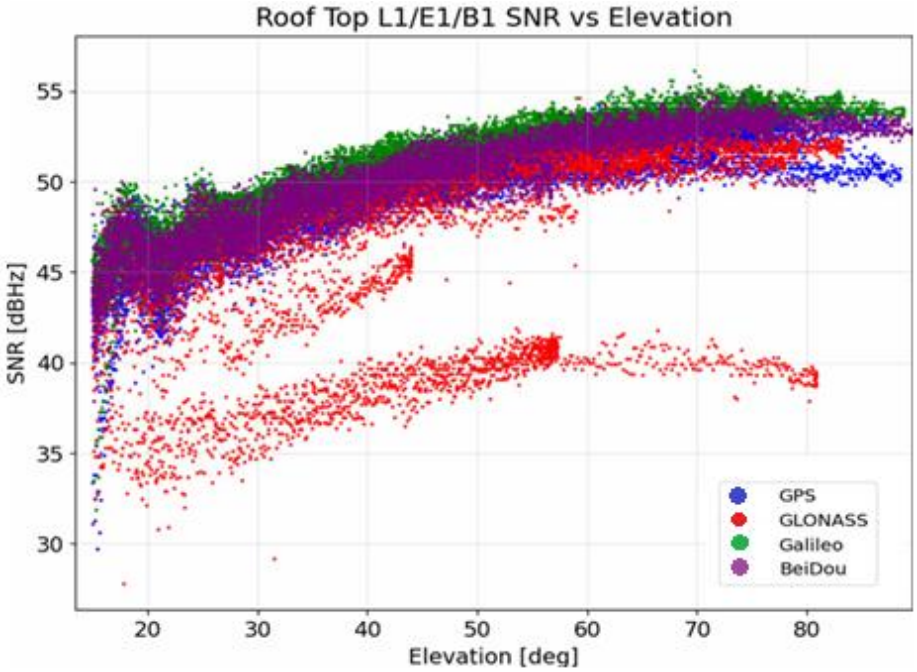


Figure 4.9: Signal-to-noise ratio (SNR) versus elevation angle at the York University Rooftop for L1/E1/B1 frequencies. SNR variations for GPS (blue), GLONASS (red),

Galileo (green) and BeiDou (purple) satellites reflect differences in signal strength and propagation conditions on DOY 223, 2024.

The different correction performance between SPARTN and CNES stems from their processing systems and operational goals. The CNES precise products use a worldwide tracking station network combined with multiple-day arc orbit determination and sophisticated post-processing models to provide precise orbit correction and accurate clock and atmospheric correction. This method allows for sub-decimetre and centimetre-level positioning accuracy, especially when used in static applications. SPARTN provides real-time positioning through regional networks. Real-time requires specific accuracy-latency compromises and basic atmospheric modelling and these are revealed within the test results, particularly within the vertical positioning and long-term stability performance measurements.

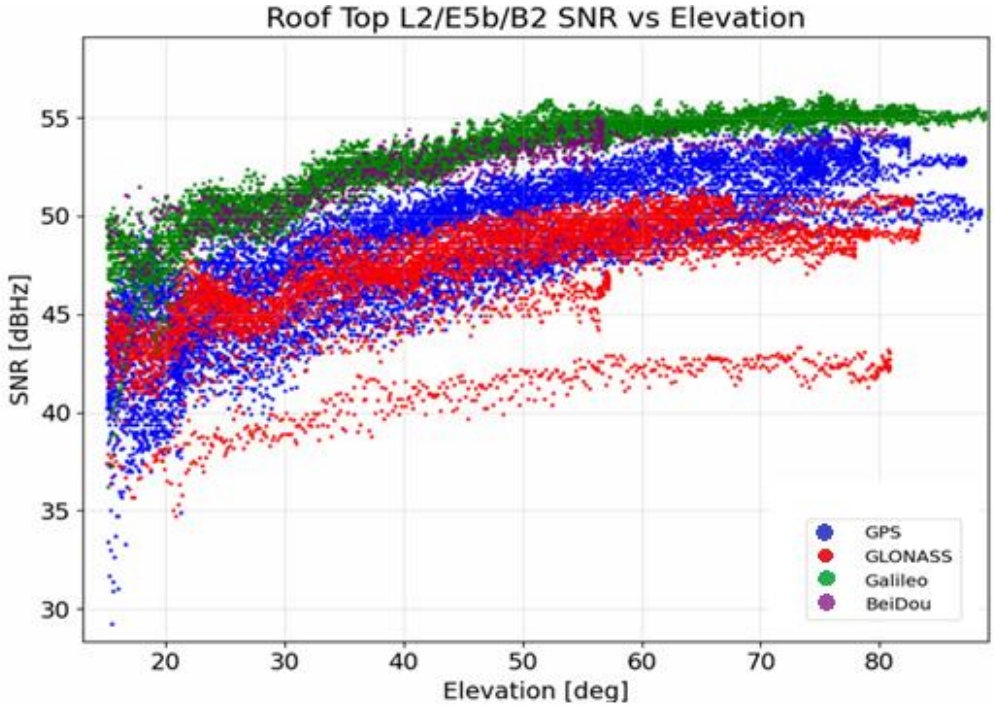


Figure 4.10: Signal-to-noise ratio (SNR) versus elevation angle at the York University

Rooftop for L2/E5b/B2 frequencies. GPS (blue), GLONASS (red), Galileo (green) and BeiDou (purple) signals exhibit expected SNR patterns across elevation angles, with generally higher SNR at higher elevations on DOY 223, 2024.

Based on this analysis, float solution performance metrics were determined to set a benchmark against which the effect of ambiguity resolution on YorkPPP processing can be measured. Use of fixed ambiguity resolution results in very high accuracy performance of 5–10 cm RMS positioning error, with solution convergence time of 10–15 minutes. Both correction services are likely to benefit from PPP-AR, but CNES products will probably continue to have a performance advantage because of the higher quality of their orbit and clock models. As a result, SPARTN will still provide useful real-time information for urgent situations and broad coverage over the globe.

4.1.2 Empirical Validation of Low-Cost Hardware Performance

To test the performance of SPARTN corrections using mass-market GNSS receivers a test was conducted using a low-cost GNSS receiver board, a SparkFun GNSS board, equipped with a u-blox ZED-F9P multi-frequency GNSS chipset and a low-cost patch antenna. The test data was collected at the York University rooftop patch pool on the 10th of August 2024. The test data was then processed offline using a modified version of the RTKLIB engine, the two SSR correction streams, CNES ultra-rapid precise products and the SPARTN correction service, were processed independently. The solutions generated by the RTKLIB engine were restricted to float PPP type solutions as the RTKLIB engine does not natively support SSR ambiguity resolution (SSR-AR). By using a low-cost receiver and patch antenna the test data includes realistic levels of measurement noise, antenna phase-center instability and multipath. This allows for a realistic test of the

correction-service under low-cost navigation conditions.

Figure 4.11 shows the east, north and up coordinate comparison between CNES and SPARTN correction streams for the same session. As seen, the performance of the two solutions is quite different. After the convergence of the solution, the horizontal components of the trajectory of CNES solution remained close to the reference, for most of the session, with east and north components being within the ±10 cm limit. This is expected given that a float PPP solution with low-cost antenna has limitations and, horizontally, the solution is expected to behave reasonably well most of the time. However, the up component showed a large variability with a positive bias of about 0.25 m in the mid session that decreased as the session proceeded to converge to the reference values. The reason for such behaviour is well known and consists of the sensitivity of the float PPP height solution to uncorrected atmospheric model errors as well as to unresolved carrier phase measurement ambiguities.

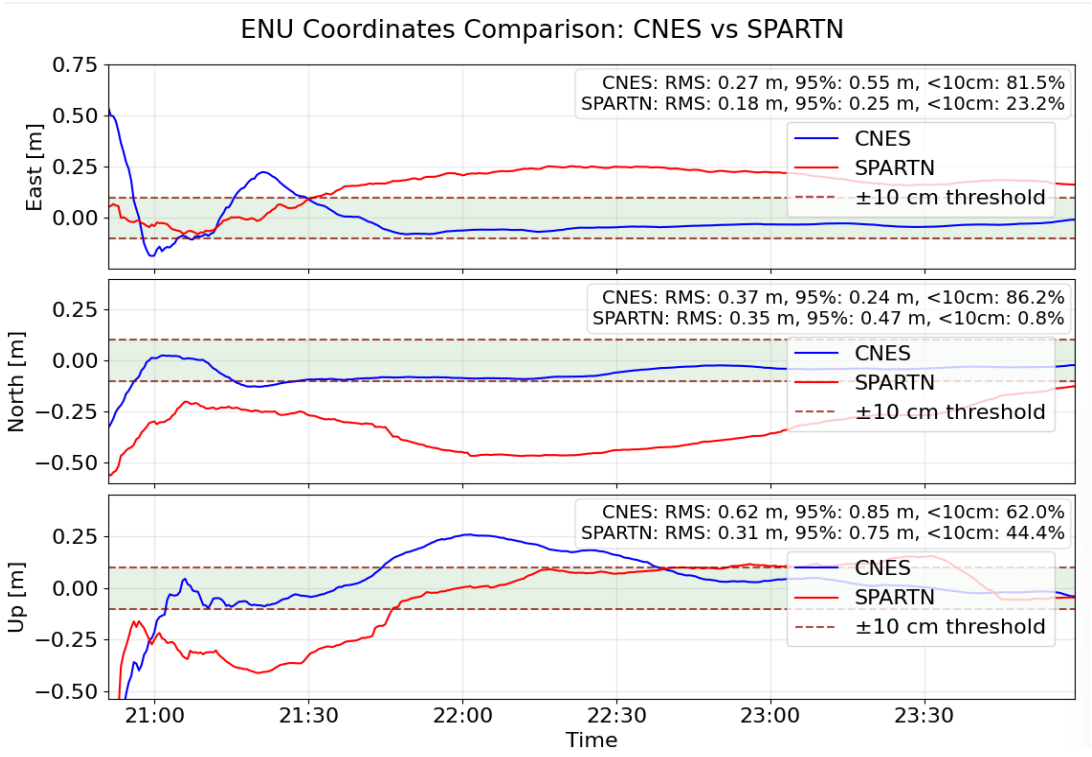


Figure 4.11: ENU position error comparison between CNES and SPARTN corrections using low-cost GNSS hardware on DOY 223, 2024.

In contrast, the solution provided by the SPARTN showed a distinctly different positioning behaviour. While the vertical component was generally smooth and stable, large systematic errors were present in the horizontal components. north errors of up to approximately 0.5 m as well as a constant positive error in the east direction were found for parts of the SPARTN trajectory. The horizontal part of the SPARTN trajectory was generally smooth, so that sub-decimetre positioning was available for most parts of the trajectory available. However, the error was consistent on the horizontal part of the solution which was shifted from the reference-trajectory. The improved stability of the vertical component suggests that the localized modelling of the atmosphere within the SPARTN HPAC corrections can be efficient in reducing residual errors of the vertical atmospheric motion, when operating with low-cost hardware.

Figure 4.12 present a comparison of the position errors as well as of the position error statistics for both correction services. In terms of horizontal accuracy, the analysis clearly shows that the CNES correction service converges much faster and therefore that the position errors remain always close to the ±10 cm threshold after a while. In terms of statistics, the RMS value of the horizontal errors is equal to 0.46 m for the CNES correction service whereas the 95th percentile value is equal to 0.64 m. In addition, the percentage of the number of epochs for which the error is lower than 10cm is equal to 61.5% for this float PPP service generated with a low cost GNSS receiver. Therefore, a sub-decimetre and even decimetre horizontal accuracy is reached for most of the time by this float PPP service.

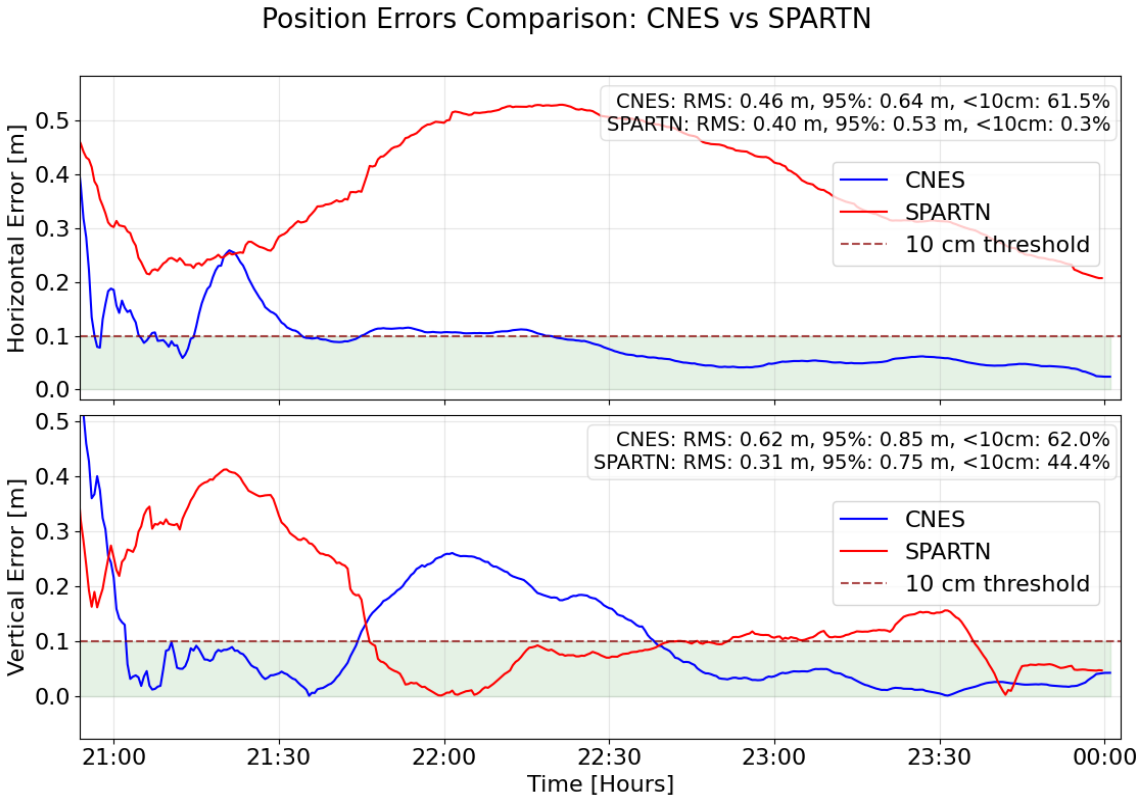


Figure 4.12: Horizontal and vertical positioning error comparison between CNES and SPARTN corrections using low-cost GNSS hardware on DOY 223, 2024.

The SPARTN solution has a slightly lower horizontal RMS error of about 0.40m and a 95th percentile error of about 0.53m. However, only 0.3% of the epochs have an error below 10cm. This is due to the horizontal bias that is still present in most of the epochs of the SPARTN solution. The lower RMS error therefore is due to a smoother but biased solution. The solution therefore is competitive in terms of horizontal RMS error but has a much worse horizontal consistency than the CNES solution compared to the ground truth reference.

In the vertical component, SPARTN performed better than CNES. The vertical RMS error of the SPARTN stream was around 0.31m whereas that of the CNES stream was around 0.62m and showed much smoother behaviour than the CNES stream. The

experiment shows that SSR correction services can bring low-cost receivers to decimetre level positioning performance. CNES brings more horizontal consistency whereas SPARTN brings better vertical error mitigation for some low-cost receiver configurations.

This experiment confirmed that SSR correction services can bring a low-cost mass-market GNSS receiver to decimetre accuracy positioning, within a float PPP environment. While CNES solution achieves better accuracy in terms of horizontal consistency and decimetre availability, SPARTN solution achieves better vertical accuracy and smaller vertical RMS error. This experiment demonstrates that new SSR correction services now available, can increase significantly the accuracy of positioning of mass-market GNSS receivers, enabling the implementation of lane-level navigation, without requiring geodetic-grade GNSS receiver.

4.2 PPP-Static Performance Analysis with IGS station

The validation test was carried out for four IGS tracking sites: ALGO in Canada and PIE1, QUIN and NRC1 in the USA. To compare the results the position data of four stations were processed and compared using standard statistical parameters, whereas detailed results were given for one station: QUIN00USA.

The QUIN geodetic monitoring station is located at Quincy, California (39.975° N latitude, 120.944° W longitude, 1105.7651 m Elevation). It is managed by Jet Propulsion Laboratory (JPL) and is in a site deemed suitable for establishing a reliable reference point for the terrestrial reference frame as well as for tectonic monitoring in highly seismically active region of California. The station is a DOMES 40433M004, and the field equipment consist of JAVAD TRE_3 DELTA receiver (firmware 4.3.00) and ASH701945E_M antenna under radome (Figure 4.13).

This geodetic-grade solution enables the reception of signals from multiple constellations (GPS, GLONASS, Galileo, BeiDou and QZSS) and is fitted with a calibration for the ROBOT antenna. The data deliver long term stability and highly precise RINEX observations and thus serve as a robust basis for the comparison between a real-time regional SSR correction (SPARTN) and a high-fidelity global SSR product (CNES).



Figure 4.13: JPL-managed ASH701945E_M antenna with radome at the QUIN IGS station, supporting geodetic and atmospheric monitoring (Adapted from International GNSS Service, 2024).

The east, north and up coordinate comparison shows how CNES and SPARTN processing methods produce different results at the QUIN IGS station. Both solutions show major initial deviations during their first 60-90 minutes of operation, which is typical for PPP convergence processes, as shown in Figure 4.14. The east component stability of the CNES solution shows better performance with 0.05 m RMS and 95% confidence bounds

at 0.05 m, while maintaining 97.6% of observations within the ±10 cm threshold. The SPARTN solution achieves the same 0.05 m RMS value, but its confidence bounds extend to 0.09 m, and its threshold compliance rate reaches 96.1%, which indicates occasional errors exceeding the primary error boundary.

The systematic differences visible in the horizontal and vertical components of the SPARTN and CNES solutions in Figure 4.14 can be due to errors in the atmospheric model, multipath, antenna phase center errors, or differences in the reference solution. The solutions were generated using the float PPP option in RTKLIB, which does not implement PPP ambiguity resolution (PPP-AR) for this workflow. Therefore, remaining biases, slower convergence and a larger variance for the coordinates in the horizontal as well as in the vertical direction are to be expected, particularly during periods of degraded satellite geometry or correction interruptions.

The north component shows similar differences between the two solutions, where CNES achieves similar RMS performance (0.07 m vs 0.07 m) and narrower 95% confidence intervals (0.04 m vs 0.03 m). The solutions maintain excellent threshold compliance at 98.6%, but SPARTN shows greater short-period oscillations between hours 3-6. This suggests that as satellites move across regional Geographic Area Definition (GAD) boundaries, the regional atmospheric corrections experience small re-initialization jumps that are not present in the global CNES model.

The up-component analysis shows the largest differences between the two solutions. The RMS values of CNES reach 0.15 m, and its 95% confidence intervals extend to 0.20 m, while the first 3 hours show extended convergence behaviour with oscillatory stabilization. SPARTN demonstrates rapid vertical convergence because it reaches stable

performance in about 90 minutes and keeps vertical errors below 0.10 m throughout most of the 24 hours. Vertical errors with SPARTN were reduced by half compared to CNES, which provides a significant benefit for applications that require height accuracy. Such superior performance at the QUIN station suggests an exceptionally high density in the local SPARTN reference network. This infrastructure provides the High-Precision Atmosphere Corrections (HPAC) necessary to decouple vertical position from atmospheric delay more effectively than global products, which must average atmospheric conditions over a much larger planetary scale.

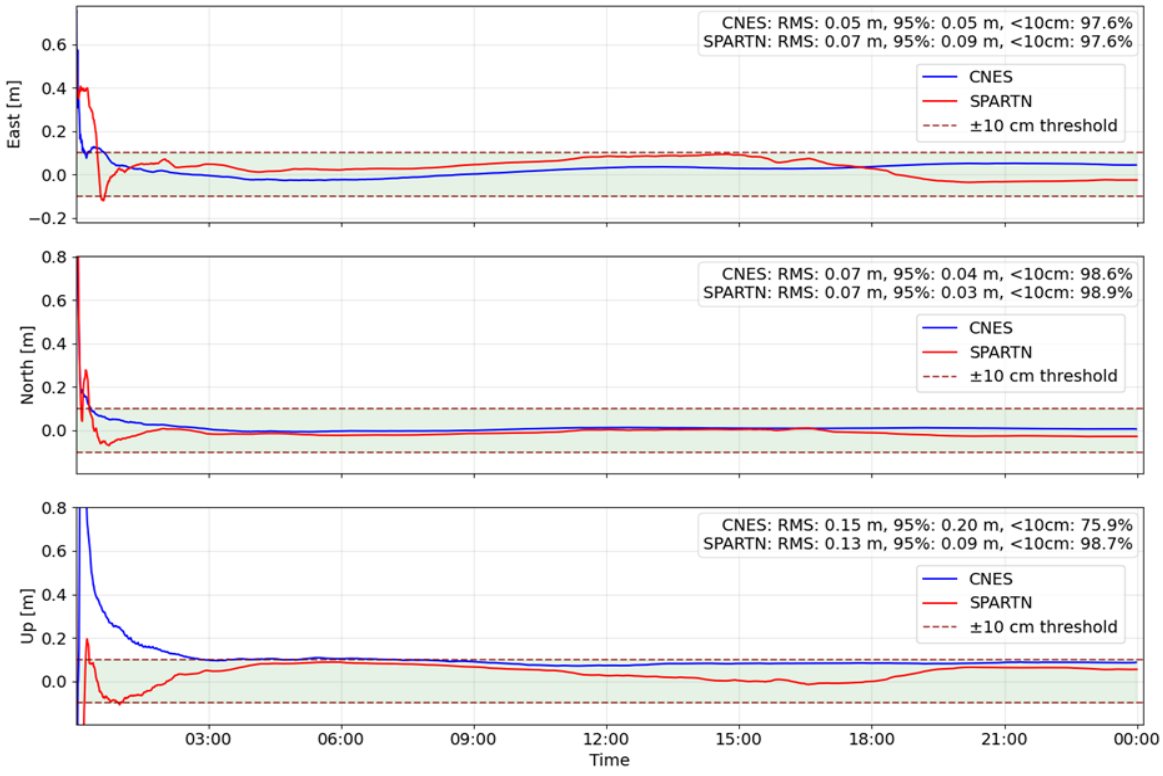


Figure 4.14: Comparison of east, north, and up coordinate errors at the QUIN reference station on DOY 222, 2024, using CNES (blue) and SPARTN (red) corrections.

Horizontal error characteristics offer additional information about solution quality. The horizontal errors of CNES remain stable between 0.02-0.04 m throughout hours 3:00-21:00

before showing a slight increase to 0.05 m at the end of the observation period, which is shown in Figure 4.15. The horizontal error measurements of SPARTN show periodic increases to 0.08-0.10 m, which becomes most noticeable between hours 12:00-15:00 and 18:00-21:00. These fluctuations in SPARTN are likely due to the transitions of satellites across regional Geographic Area Definition (GAD) boundaries, which can cause small re-initialization jumps in the filter that are not present in the global CNES model. Vertical error measurements appear to oscillate periodically and correlate to changes in satellite geometry visible in the elevation plot, possibly related to variations in DOP or multipath effects.

The vertical error analysis indicates some marked differences between the vertical component estimation strategies implemented by CNES and SPARTN. The vertical component estimation performed by CNES steadily converges and displays a bias of 0.09-0.10 m for most of the pass. Conversely, the vertical error of SPARTN reaches near-zero for hours 12:00 – 18:00. The superior vertical performance at QUIN is primarily due to the high density of the local SPARTN reference network providing localized High-Precision Atmosphere Corrections (HPAC) specific to the station's location. Global products such as CNES average the station height estimation and the delay due to the atmosphere (ionospheric and tropospheric) over a large planetary area, as opposed to the filter utilising the SPARTN reference network to decouple these parameters more effectively at the local station scale. Additionally, SPARTN operates with 25–30% fewer satellites as it selectively includes satellites with valid regional messages within the pass. The quality of the localized corrections permits SPARTN to attain increased vertical precision during periods of stable tracking at the station.

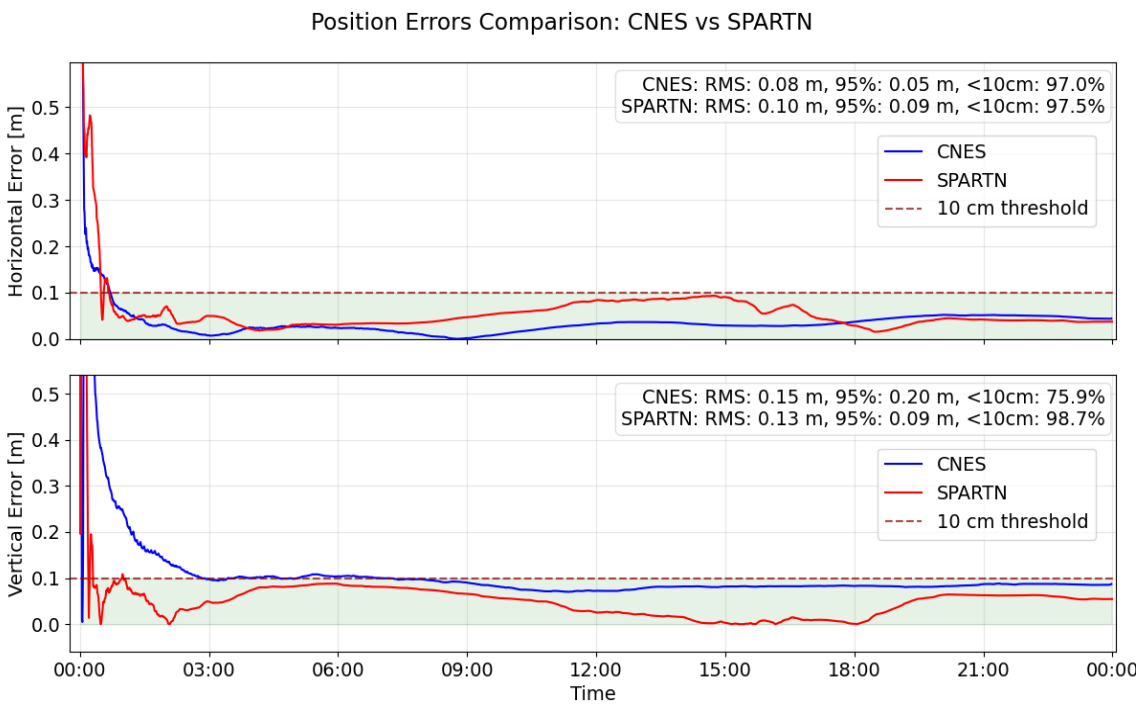


Figure 4.15: Comparison of horizontal and vertical positioning errors at the QUIN reference station on DOY 222, 2024, using CNES (blue) and SPARTN (red) corrections.

A small systematic vertical offset is visible in both the CNES and SPARTN solutions. Since the bias is present in both correction streams, it is unlikely to be introduced by the SPARTN correction implementation. It is likely to be due to some remaining tropospheric modelling error, some error in the antenna phase center model, or some error in the reference coordinates in the PPP solution. The vertical component is more sensitive than the horizontal components to such errors, and to errors in the PPP solution reference coordinates, than the horizontal components, which explains the presence of a small vertical bias despite otherwise stable positioning performance.

4.2.1 Satellite Visibility and Correction Availability Analysis

The QUIN station shows outstanding multi-constellation tracking abilities through its SNR and elevation plots, as shown in Figure 4.16. The station tracks 30 to 55 satellites and

received the signals with signal to noise ratio (SNR) of 35-50 dB with some occasional spikes up to 55 dBHz. As expected, Galileo (green) and BeiDou(purple) signals have higher SNR comparing to GPS (blue) and GLONASS (red) mainly because of the modernized signals on the new constellation. The wide scatter on GPS and GLONASS at lower elevation angles is a result of both ionospheric and tropospheric attenuation/signal to noise degradation as signal travels a greater path length through these layers.

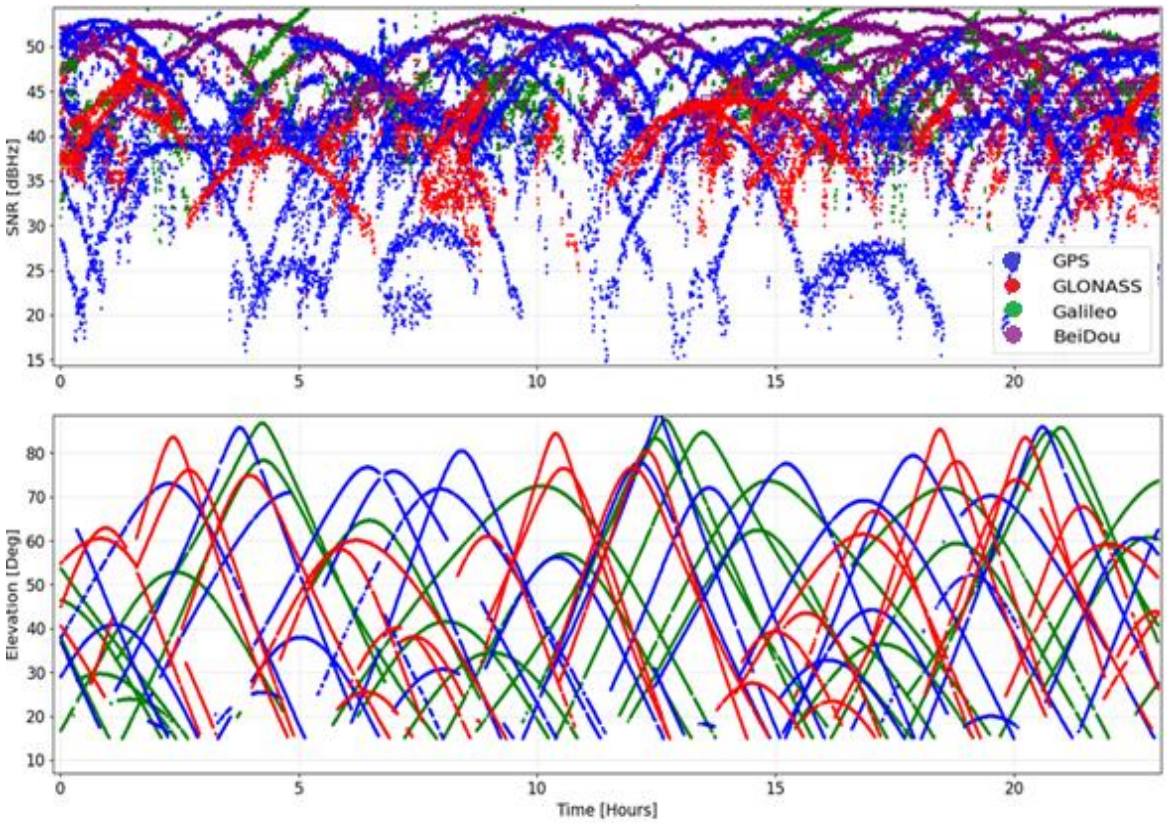


Figure 4.16: Signal-to-noise ratio (SNR) and satellite elevation angles observed at the QUIN IGS station on DOY 222, 2024, during a 24-hour static test.

The elevation plot shows multiple periods of satellite tracking interruptions, which become most noticeable during hours 3, 8, 13 and 20. These gaps in correction data availability are not caused by physical obstructions at the station site, but rather by regional

modelling limitations in the SPARTN correction stream. Specifically, these gaps occur when a satellite's ionospheric pierce point (IPP) falls outside the active Geographic Area Definition (GAD) grid or when the atmospheric modelling confidence fails to meet the required threshold for centimetre-level accuracy. The periods without correction data match the time when both processing strategies show their worst performance, especially the SPARTN solution, which shows larger error values after these gaps. Real-time PPP solutions heavily depend on continuous correction streams because brief interruptions in correction streams can negatively affect their performance.

In the current implementation, satellites without valid HPAC corrections are not included in the SPARTN atmospheric correction processing. However, for the RTKLib processing, as with all other cases, satellites without HPAC corrections are processed using fallback atmospheric models such as the broadcast ionospheric model and the standard tropospheric model. Thus, the exclusion of satellites without valid HPAC corrections is specific to the SPARTN atmospheric correction processing and does not affect the rest of the positioning filter processing.

The satellite elevation distribution presents clear geometric patterns because satellites occupy elevation angles ranging from 10° at the horizon to 90° at the zenith. The multi-coloured traces show different GNSS constellations which provide the necessary geometric diversity needed for strong positioning solutions. The consistent elevation patterns indicate stable constellation geometry; however, the abrupt "cutting" of traces, where satellites are visible but not processed, proves that continuous regional atmospheric corrections are the primary constraint on SPARTN's solution availability, even when the physical satellite geometry is ideal. Figure 4.17 shows the visibility of BeiDou and Galileo satellites masked

due to unavailability of SPARTN correction data. These satellites are in view but are not tracked due to BeiDou messages being flagged as invalid and the inability of the filter to support the latest Galileo signals, contributing to the instability observed at the navigation solution filter and the vertical “jumps”.

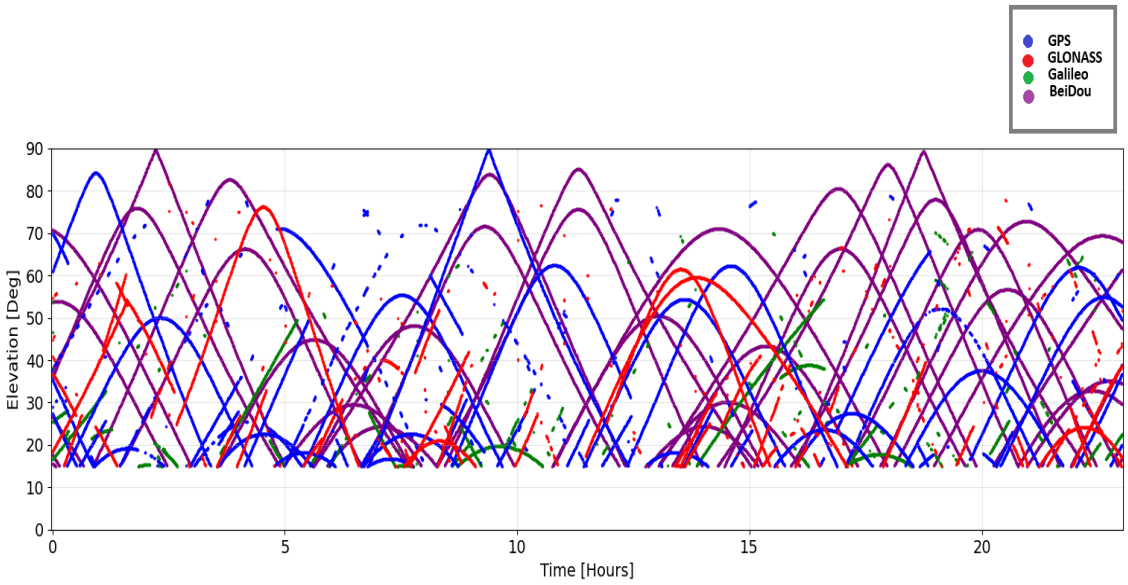


Figure 4.17: Elevation plot showing satellite exclusion due to SPARTN correction unavailability at the QUIN IGS station on DOY 222, 2024.

4.2.2 Multipath and Residual Analysis

The QUIN IGS station displays good multipath site conditions in Figure 4.18. The multipath values show a ±1 metre range distribution throughout the 24 hours of data, with a near zero average value of 0.001 m. There is no pronounced periodic structure or large number of outliers for either time or baseline. The average multipath of 0.001 m is close to zero meaning that there is no dominant, stationary multipath producing surfaces, such as nearby metal, large walls or windows. The RMS value of 0.330 m displays the high frequency “noise” that exists at a geodetic grade static processing position due to ground

reflections and low elevation angle measurements. The design of the station position is very good presumably due to the high quality ASH701945E_M antenna and radome combination. The bottom of the radome does present a rather steep angle that might cause some concern for future antenna systems. As expected, there are no large variations in the multipath values throughout the day and there are no significant outliers or large “waves” in the plot that would indicate poor control of the site surroundings. Hence, any differences in range correction accuracy between the SPARTN and CNES processing strategies should be evident in the performance of the resulting time series and not because of site-to-site performance differences.

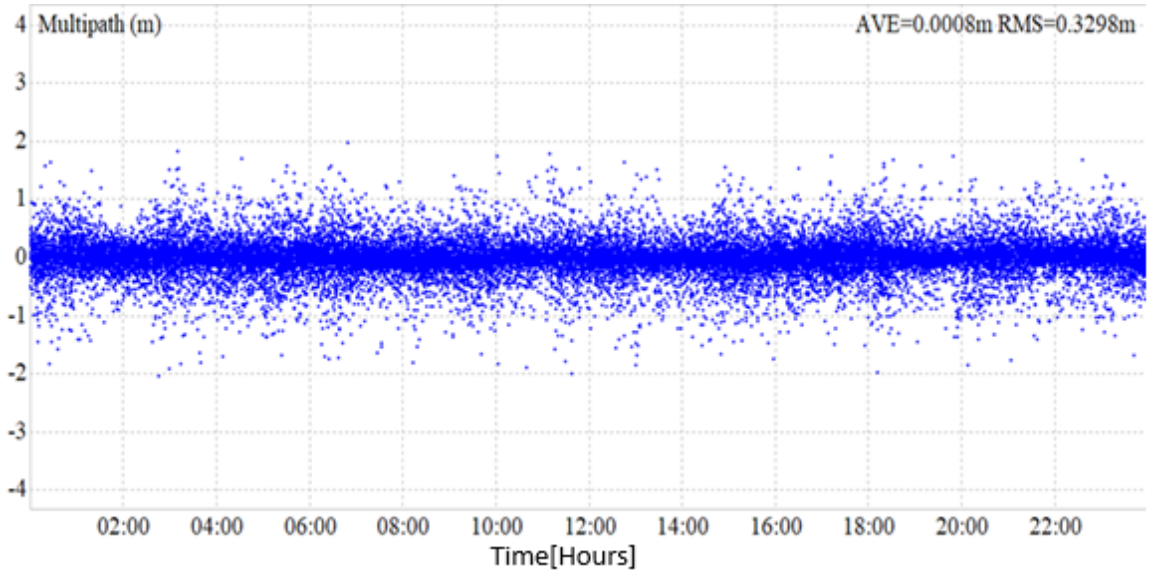


Figure 4.18: Estimated multipath error for GNSS observations at the QUIN IGS station on DOY 222, 2024, during a 24-hour static test.

The pseudorange and carrier-phase residuals give an indication of the quality of the measurements and the performance of the processing (see Figure 4.19). The pseudorange residual range between ±7.5m with different colour patterns for the different constellations. The pseudorange residuals include the unmodelled remaining atmospheric effects plus the

code noise and code multipath effects remaining after atmospheric correction. The tighter, more regular pattern for some constellations (notably Galileo) is due to the higher chip rate and modernised modulation (BOC) compared to older signals.

As shown in the left panel of Figure 4.19, the stratification seen at approximately ±2.5 m intervals for different receiver corresponds to receiver-specific correlator characteristics or biases in the code that are not perfectly stratified. Each satellite, therefore, has a systematic offset to its errors that the PPP filter must average in the time needed to converge to initial fixation. Note that the error distribution is cantered at zero. One approach that could reduce the effect of these site reflections, which recur as a function of satellite sky position, would be to implement stochastic weighting of the measurements.

The residual of the carrier-phase, shown in the right panel, it has a centimetric dispersion with most values between ± 0.2 m, showing a very stable distribution around zero, without significant "drifts" with time. This stable behaviour is what transfers to the east, north and up solution, in the sense that it remains very stable as well. Most of the values are cantered around zero and show little dispersion. The ambiguity residual (or float) is also very stable, not showing large deviations at any time. The absence of outliers also indicates good performance of the processor in the detection and repair of cycle slips, even when bad weather conditions, such as that with turbulence seen on the radar image shown above, are present. Such high-quality phase data is responsible for the sub-decimetre solution performance achieved in this test over a 24-hour interval.

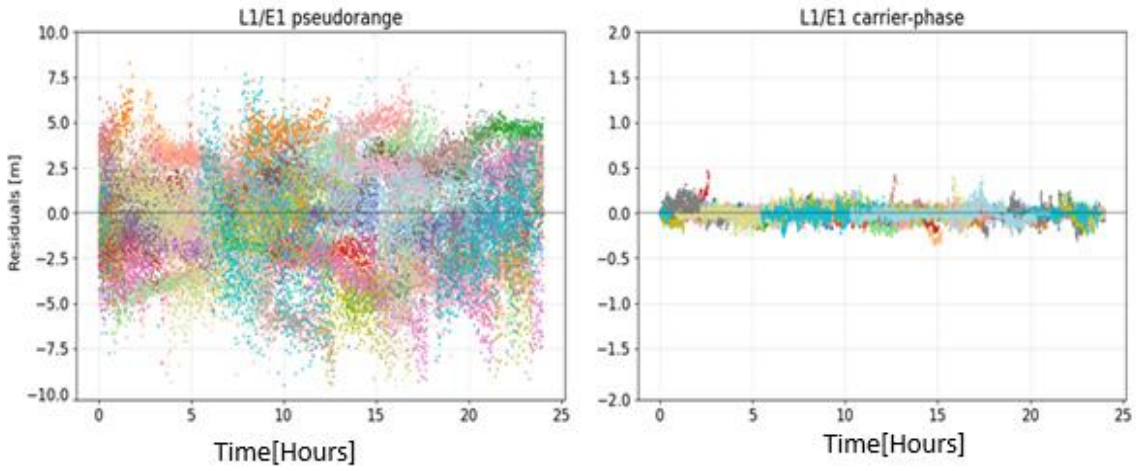


Figure 4.19: Residuals of L1/E1 pseudorange (left) and carrier-phase (right) measurements at the QUIN IGS station on DOY 222, 2024, during a 24-hour static test.

It is important to note that the results presented for both CNES and SPARTN are float PPP solutions, as the RTKLIB processing engine does not currently support Ambiguity Resolution (AR) for these specific SSR correction streams. In float solutions, phase ambiguities are treated as continuous real numbers. This leads to longer convergence time on the order of 60–90 minutes, as indicated by the east, north and up plots above. In addition, the horizontal "weaving" of approximately 0.05 m to 0.10 m seen in the SPARTN float solution tracks is typically caused by slowly drifting or oscillating ambiguities or some other change in satellite geometry and regional atmospheric modelling (HPAC/GAD) that the float solution is responding to, as opposed to the stability associated with an integer fix.

The comparative analysis clearly demonstrated a vertical bias in the CNES solutions which is likely to be caused by several technical reasons typical for global PPP correction services. Firstly, the vertical (up) component is highly sensitive to the tropospheric delay modelling, which is generally done by global atmospheric models. Even small residual

errors in these models can cause systematic offsets in the height component of the measured position. Secondly there are errors caused by inconsistencies between the PCO and PCV models used in the CNES correction products, and the ones used in the local receiver antenna models. These errors are mostly absorbed in the vertical component of the measured position.

Another consideration is the reference frame. To compare NAD83(CSRS) ground truth coordinates with IGS20 CNES corrections, appropriate transformation of the ground truth coordinates to the IGS20 reference frame as well as alignment of the CNES correction epochs to the same epoch as the corresponding receiver position must be undertaken. Although the differences between the NAD83(CSRS) and IGS20 reference frames are small, they can become apparent as systematic biases in high-precision PPP analysis, particularly in the vertical component. Care must therefore be taken to accurately transform the ground truth coordinates as well as to accurately align the reference frames to segregate any analysis errors from frame errors (Reid et al., 2023).

4.2.3 Frequency-Specific SNR-Elevation Relationships

The SNR-versus-elevation analysis reveals distinct performance variations across the primary GNSS frequency bands. For the L1/E1/B1 band (Figure 4.20), Galileo and BeiDou signals demonstrate the most stable behaviour, characterized by tightly clustered observations around the mean trend and peak SNR values approaching 52 dBHz. In comparison, GPS L1 observations exhibit noticeably greater variability and scatter across the elevation range. Meanwhile, the GLONASS L1 signals display a distinct performance pattern in which a subset of satellites consistently operates approximately 5–7 dBHz below the overall constellation average. This behaviour is likely related to receiver-side filter

attenuation effects associated with the GLONASS FDMA signal structure, as well as performance differences linked to older satellite hardware generations.

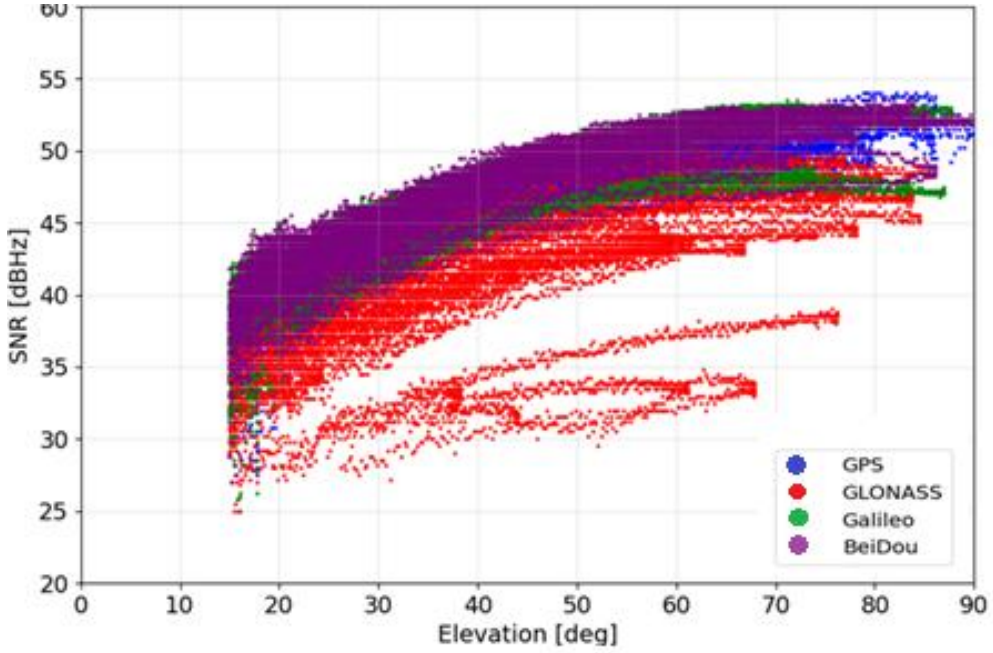


Figure 4.20: Signal-to-noise ratio (SNR) versus elevation angle at the QUIN IGS station on DOY 222, 2024, for L1/E1/B1 frequencies.

The differences in performance become more pronounced at the L2/E5b/B2 frequency band (see Figure 4.21). Galileo E5b and BeiDou B2 signals have the strongest and most stable signal tracking performance. Their signal to noise ratio (SNR) values are around 57 dBHz. As opposed to the signals from the other two systems, the GPS L2 observations have a bifurcation at lower elevation angles. The reason for this bifurcation is the large difference in performance between the legacy GPS satellites broadcasting encrypted P(Y)-signals on the L2-frequency and the modernized GPS satellites broadcasting L2C-signals. The semi-codeless tracking of the L2 P(Y)-signals results in a loss of 3–6 dBHz in effective SNR, whereas the L2C-signal is tracked with stronger and more stable signal tracking performance.

These lower-SNR observations pose problems for the processing within the SPARTN framework. The current implementation does not contain a fallback strategy for such observations, which are excluded from the SPARTN atmospheric correction modelling after failing to fulfill the strict “High-Precision” confidence threshold. The thus rejected signals directly cause the already mentioned problems for the satellite tracking, which manifests itself in a fragmented manner and leads to periodic availability gaps. This in turn affects the obtained positioning results in a negative way.

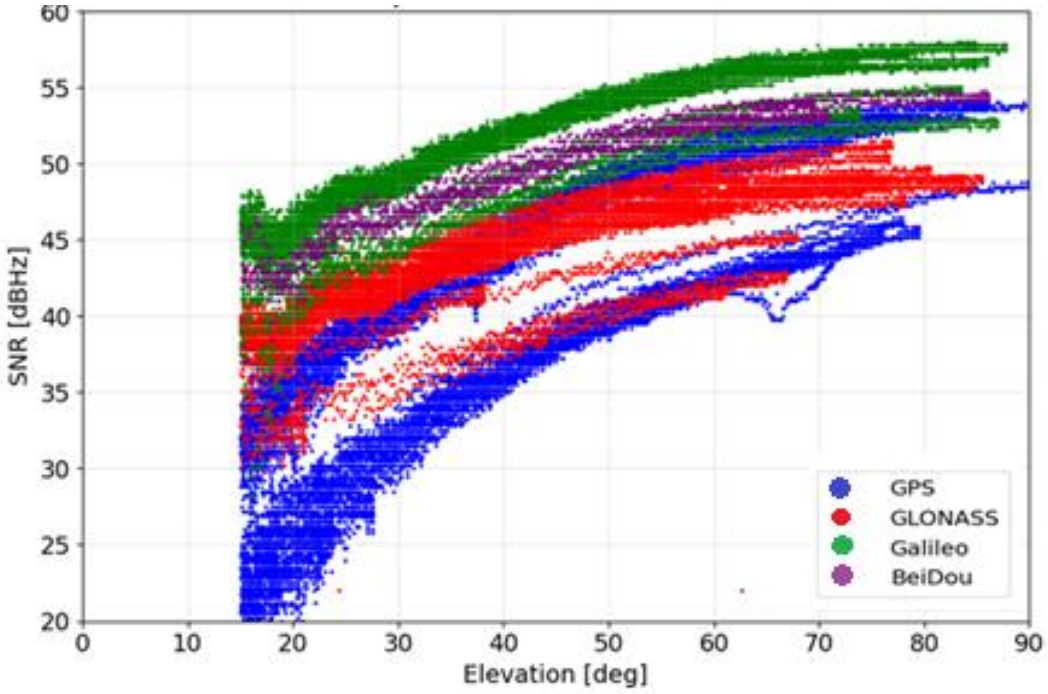


Figure 4.21: Signal-to-noise ratio (SNR) versus elevation angle at the QUIN IGS station on DOY 222, 2024, for L2/E5b/B2 frequencies.

4.2.4 Satellite Availability and Correction Limitations

The satellite availability plot (Figure 4.22) shows a significant operational difference between the CNES and SPARTN solutions. The CNES solution (blue) has an average of 22 satellites in view. The SPARTN solution (red) has an average of 11-15 satellites in view.

Both solutions are Float PPP solutions, i.e. RTKLIB does not support Ambiguity Resolution (AR) for these SSR streams, therefore the phase ambiguities are solved as continuous real numbers.

During the comparative analysis it was noticed that there were fewer satellites tracked in the SPARTN solution than in the precise products provided by CNES. The stream of corrections for the SPARTN solution contained irregularities of the tracking of satellites and missing observations. This is due to the bandwidth-optimised design of the SPARTN architecture, which uses very aggressive compression and, in addition, integrity and quality masking.

The SPARTN system is designed as a safety-critical system for autonomous navigation. For this reason, satellites which do not fulfill several predefined quality measures, or which are not sufficiently supported by the regional correction network are not included in the correction stream that is broadcast to the users. The effect of this selective correction is that the number of usable satellites is reduced. This in turn can cause a loss of satellite geometry and an increase of the Position Dilution of Precision (PDOP) as compared with a globally distributed geodetic correction, as is used by the CNES precise products for example.

This technical subtlety results in a reduction of the satellite constellations tracked by SPARTN of 25–30%. We also note that at the QUIN station, many satellites are excluded from the filter because their Ionospheric Pierce Points (IPPs) are not within the modelled regional Geographic Area Definition (GAD) grid. This exclusion is particularly costly for the float-only solution, as the filter must re-estimate the float ambiguity for any satellite that is excluded and later re-included in the solution. The solution never reaches the integer-

fixed state it would have the satellite been included in a single pass, and as a result, exhibits 60–90 minute convergence times, and horizontal "weaving" of several minutes.

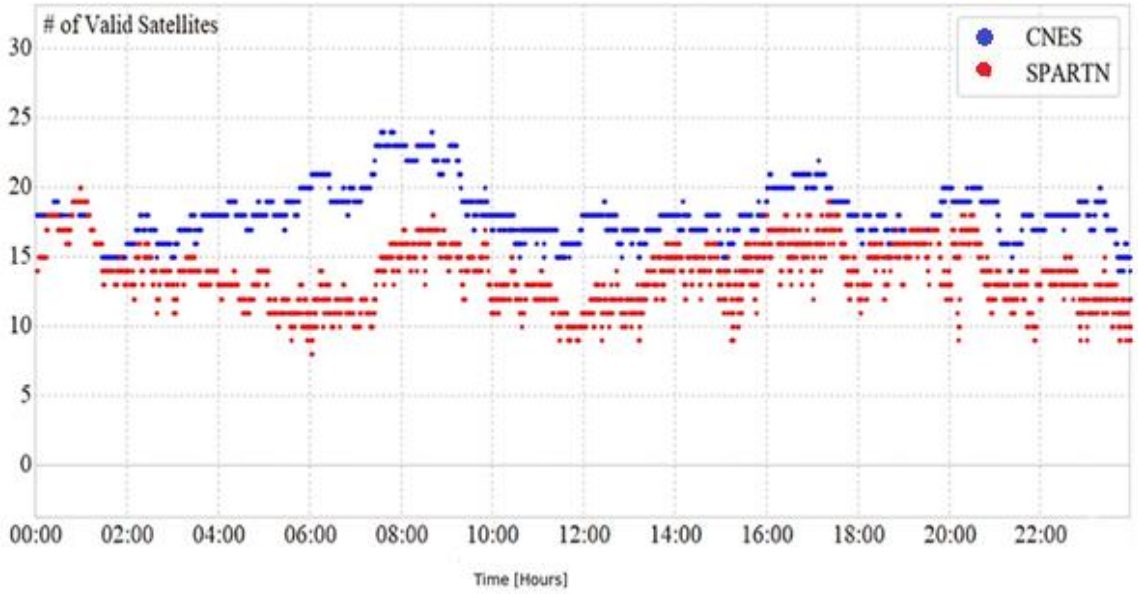


Figure 4.22: Number of valid satellites used in CNES (blue) and SPARTN (red) solutions during static testing at the QUIN IGS station on DOY 222, 2024.

Because SPARTN was designed to be very fast at achieving a PPP-RTK solution, the code rejects satellites for which there is no current atmospheric data to avoid polluting the float filter with unmodelled ionospheric residuals. While discarding some satellites results in less than optimal geometry and therefore higher than optimal VDOP, the retained satellites provide extremely high-quality corrections that are sufficient to maintain the float vertical error at decimetre level. Without the benefit of AR to "lock" the position, the SPARTN solution relies entirely on the quality of these regional atmospheric corrections to maintain its edge over the CNES global baseline.

4.3 PPP-Kinematic with Test Vehicle

A performance evaluation of the SPARTN and CNES correction systems was conducted using vehicle-based kinematic measurements recorded at York University on August 8, 2024 (GPS Week 2326, DOY 221). The analysis utilises a rigorous statistical framework to evaluate positioning precision and temporal stability across the east-north-up coordinate dimensions.

4.3.1 SPARTN Correction Service Performance Evaluation

The SPARTN-based positioning errors versus the reference trajectory are presented in the east, north and up coordinate frame in Figure 4.23. The horizontal performance is on the lane-level, with east RMS 0.399 m and north RMS 0.319 m. While the north error is generally zero cantered with Mean of 0.076 m, there is a persistent systematic bias in the east error with mean of -0.347 m, which could be related to the coordinate transformation error or misalignment of local reference frames in the SPARTN data.

The main technical issue appears to be vertical positioning with an average up RMS of 0.521m and a consistent bias of -0.511m on average. The solution has a high susceptibility to vertical instability with errors consistently above the 0.5m threshold limit. The recorded trajectory shows a significant transient spike at 20:24 due to physical blockage of the signals during an underpass. This event forces the filter to re-converge as satellites are regained, a process further complicated by the exclusion of the BeiDou and Galileo signals. To mitigate these excursions and bridge signal outages during underpasses, future implementations should incorporate IMU fusion and more granular regional atmospheric models to decouple receiver height from atmospheric residuals.

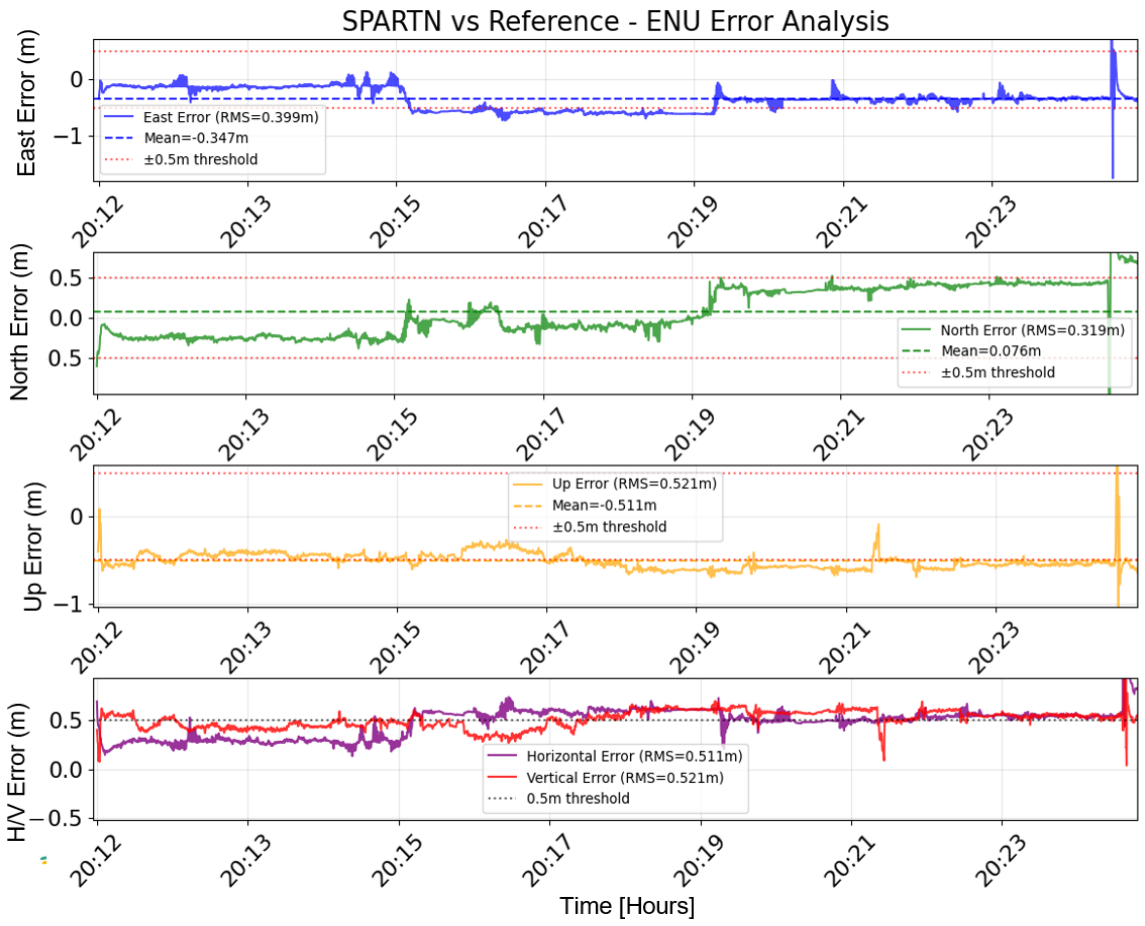


Figure 4.23: Position errors of the SPARTN solution relative to the reference trajectory during the kinematic GNSS test on DOY 221, 2024. RMS errors and the 0.5 m threshold are shown for the east, north, and up components.

4.3.2 CNES Correction Service Performance Assessment

As illustrated in Figure 4.24, the errors have a different profile compared to SPARTN. The east error has an RMS of 0.661 m with a systematic bias with a mean of -0.546 m. The north error has an RMS of 0.503 m with a mean of -0.262 m. Similar to the SPARTN solution, a large convergence error occurs at 20:24 over the underpass in the vertical direction and results in a large horizontal and vertical error as the filter converges to lock on the next set of signals. Performance results show the vertical component of range

measurements to have an RMS error of 0.556 m and be biased downwards (Mean = -0.517 m). Despite the global corrections provided by CNES, the decimetre-level errors remaining after processing and the global performance could be attributed to local signal attenuation and multipath phenomena in urban environments. These performance results therefore establish an upper limit to what can be expected from float implementation of PPP for such data. Achievement of significantly better accuracy for autonomous navigation requires not only the fixing of integer ambiguities (PPP-AR) but also the incorporation of IMU measurements to bridge physical gaps such as the underpass crossing at the end of the test.

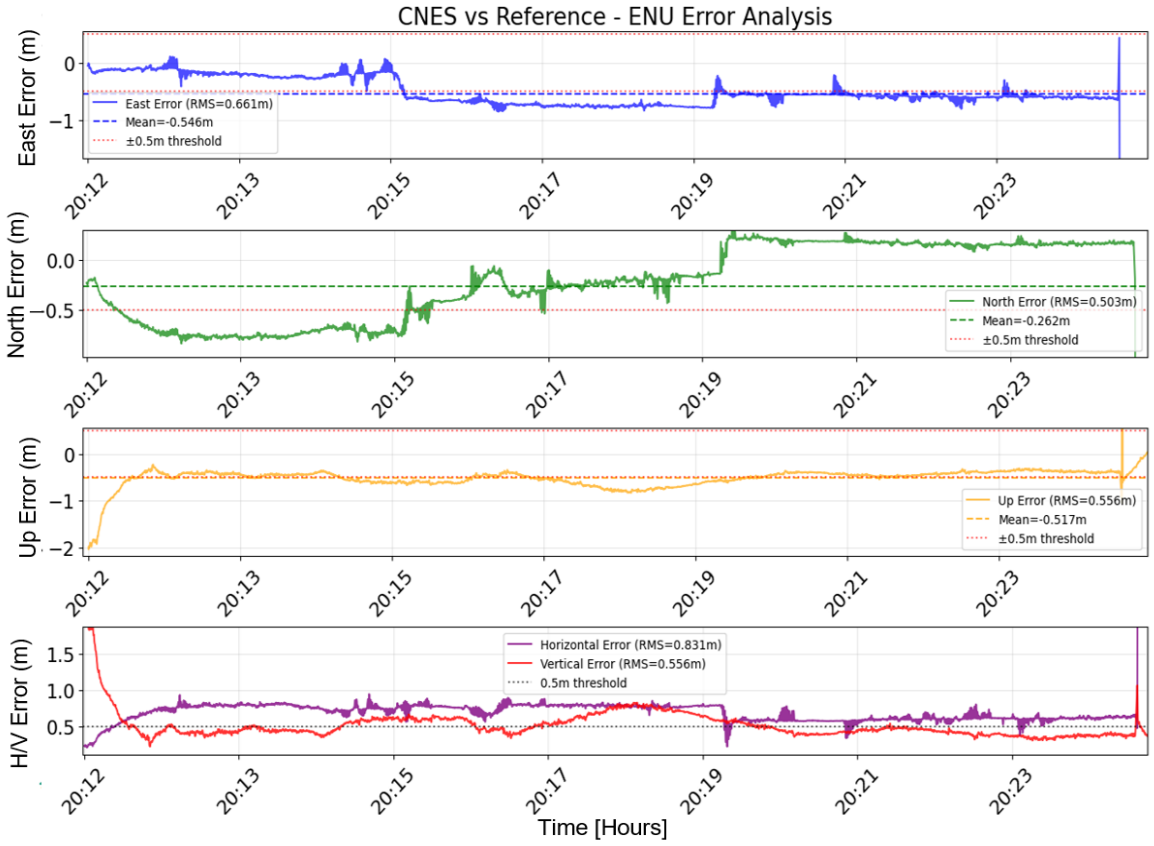


Figure 4.24: Position errors of CNES solution relative to the reference trajectory during the kinematic GNSS test on DOY 221, 2024. RMS errors and the 0.5 m threshold are shown for the east, north, and up components.

4.3.3 Statistical Performance Comparison and Analysis

The extensive statistical examination shows that SPARTN and CNES correction services have different levels of service reliability, together with service consistency. Table 4.1 presents a statistical analysis of the accuracy of SPARTN and CNES correction services. The 95th percentile accuracy of SPARTN for horizontal/vertical (H/V) accuracy is 0.63 / 0.63 m, with SPARTN achieving significantly better results than CNES at 0.84 / 0.79 m. Consequently, the SPARTN predictions remain below the sub-0.7 m threshold with 95% confidence, whereas CNES remains below the threshold at nearly 0.85 m. This greater accuracy allows for better prediction of worst-case scenarios in high-precision applications.

Table 4.1: Horizontal and vertical positioning error statistics for SPARTN and CNES corrections during the kinematic GNSS test on DOY 221, 2024.

Dataset	95th Percentile (H/V) [m]	68th Percentile (H/V) [m]	Overall RMS (H/V) [m]	Std. Deviation (H/V) [m]	Mean (H/V) [m]
SPARTN	0.63 / 0.63	0.56 / 0.56	0.51 / 0.52	0.16 / 0.09	0.51 / 0.52
CNES	0.84 / 0.79	0.78 / 0.56	0.83 / 0.56	0.36 / 0.20	0.83 / 0.56

The standard deviation of SPARTN (0.16 m H) is smaller than CNES (0.36 m H) which reflects a greater stability and higher accuracy of its solutions. While the horizontal RMS error remains in the 0.5–1.0 m range for a multi-constellation dual-frequency float PPP, a much greater variability from sample to sample is observed for the CNES service. Moreover, the H/V mean error is greater (0.83 / 0.56 m) for the global CNES product than for the bandwidth-optimised regional SSR SPARTN service. However, a similar positive vertical bias is found in both solutions and therefore part of the up component offset could stem from the reference trajectory or other systematic errors not contained in the correction products. Such errors could be caused by residual differences in the reference frames, by

differences in the antenna phase center models or by still uncorrected errors in the INS/GNSS trajectory. Therefore, although both services provide decimetre accuracy, the horizontal solution consistency of SPARTN is significantly better for this temperate mid-latitude region.

5. Experiments and Analysis from YorkPPP

A series of experiments were conducted to assess the ability of a rooftop GNSS receiver at York University to perform high-precision positioning, to test the global as well as regional correction stream capabilities. The rooftop installation is an open-sky, geodetic-grade configuration which allows for unobstructed reception and performance assessment of the correction stream products, free from local, non-geometric interference sources. CNES and SPARTN products from 10 Aug 2024 were utilised to investigate the positioning performance over a 20-hour time baseline. The performance results describe the receiver's ability to converge to a fixed solution state from a float state solution over the east, north and up dimensions and discuss how the state-space representation (SSR) stream deals with residual errors in carrier phase measurements, as well as its ability to solve for the integer ambiguity (N) necessary for the receiver to attain centimetre-level positioning stability.

5.1 Static Positioning Performance at York University

GNSS positioning accuracy tests using SPARTN correction service were performed to evaluate baseline performance against CNES precise products data on DOY 223, 2024 (August 10, 2024). The aim of this test was to evaluate differences in correction performance before ambiguity resolution i.e. using float solution. GNSS receiver tracking GPS, GLONASS, Galileo and BeiDou signals on L1/E1/B1 and L2/E5b/B2 bands operated continuously on the rooftop of York University during the test period.

5.1.1 Empirical Validation of Geodetic grade Hardware Performance via YorkPPP

The east, north and up error trends using CNES products as shown in Figure 5.1 demonstrate that once initial filter convergence is achieved, both float and fixed solutions

provide consistent geodetic accuracy. In the horizontal components, the east direction exhibited a mean error of 0 cm with a standard deviation of 6 cm for the float mode, while the north direction remained stable at 1 cm. The vertical (up) component, however, showed a larger 11 cm standard deviation. This increased vertical noise is a fundamental characteristic of GNSS geometry (Hofmann-Wellenhof et al., 2008). The main reason for this is that there aren't any satellites below the horizon, which means we get a Vertical Dilution of Precision that's usually 1.5 to 2.5 times larger than the precision we get for horizontal measurements.

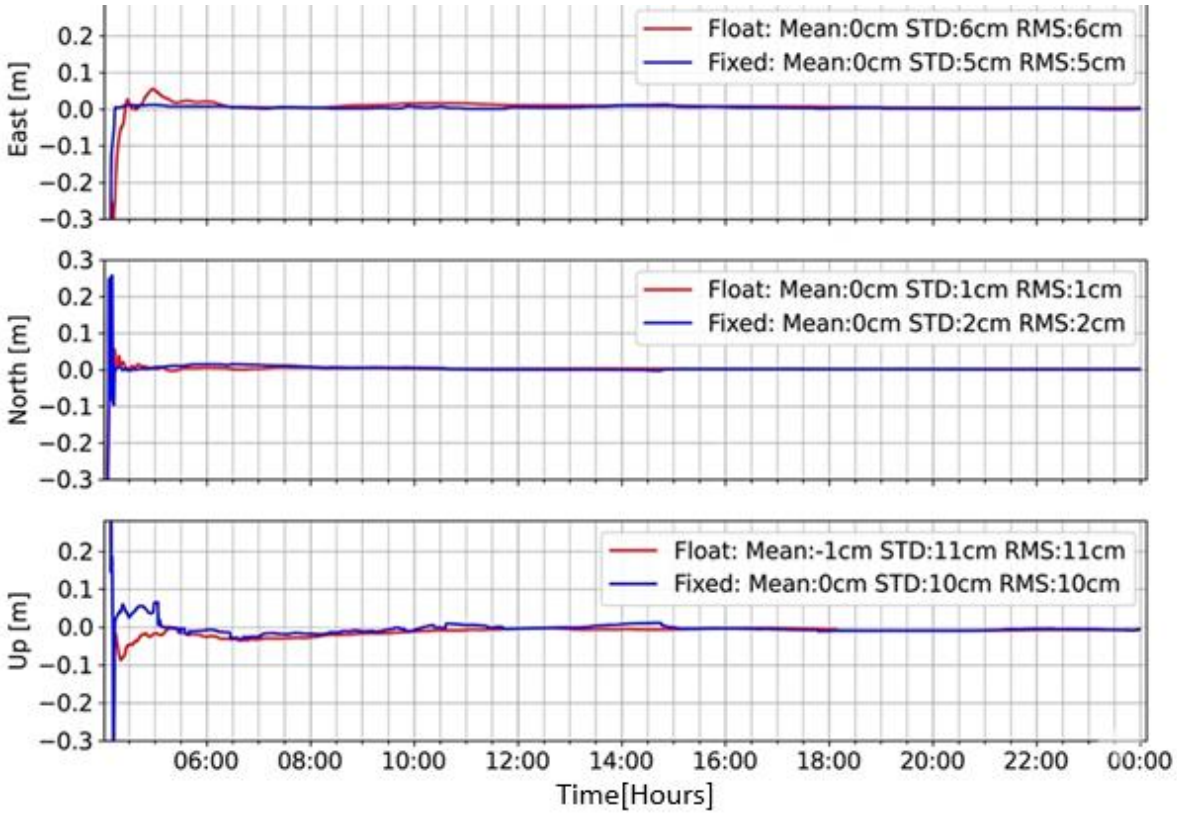


Figure 5.1: ENU errors (float versus fixed solutions) using YorkPPP with CNES corrections from the rooftop experiment at York University on DOY 223, 2024.

In terms of performance gain, the fixed ambiguity solution offers a fast track to high precision positioning in a short time. The convergence plots and statistics in Figure 5.2 and

Table 5.1, it is observed that fixed solution reached initialization in 8.00 minutes, which is a 33% decrease from the 12.00 minutes needed to reach float solution high precision. While the horizontal RMS (5.05 cm) shows a gain of only 0.68 cm over float solution (5.73 cm), there is a 12% increase in overall positioning accuracy. This gain is attributed to the Ambiguity Resolution (AR) process that fixes the ambiguity in integer value by relating the GPS receiver position to the corresponding carrier-phase wavelength (Wübbena et al., 2005).

Table 5.1: Performance metrics for dual-frequency positioning: CV and RMS error analysis using CNES products.

	FL CV (min)	FL hor. rms (cm)	Fl ver. rms (cm)	FX CV (min)	FX hor. rms (cm)	FX ver. rms (cm)
dual freq	12.00	5.73	10.97	8.00	5.05	9.70

The performance of the float and fixed solutions is also tested in changing conditions of satellite geometry. The number of satellites tracked varied and, as part of the multi constellation study, reached as many as 25 satellites for certain configurations; however, the PDOP remained consistently below 1.5.

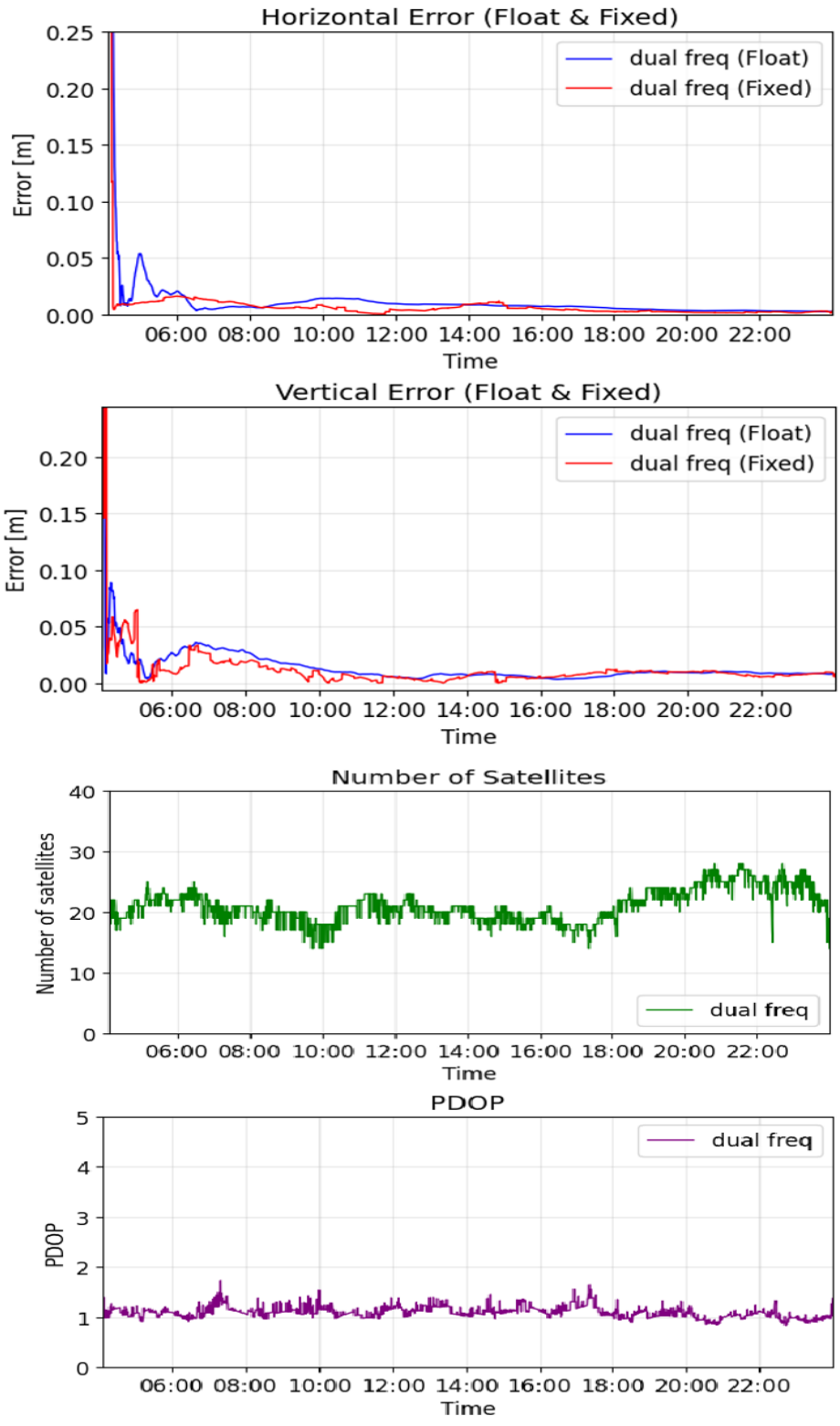


Figure 5.2: Horizontal and vertical positioning performance of float and fixed solutions using YorkPPP with CNES corrections, including satellite count and PDOP variation from

the rooftop experiment at York University on DOY 223, 2024.

Positioning results using CNES global correction stream are supported by the signal residuals given in Figure 5.3. As expected, C/N_0 normalized L1/E1 and L2/E5b pseudorange residuals move within a +/- 2.0 m range, showing still impact of code noise and local multipath effects after application of global orbit correction and best available clock corrections. The observed residual level for a geodetic-grade rooftop receiver agrees with results found in literature (Hofmann-Wellenhof et al. 2008).

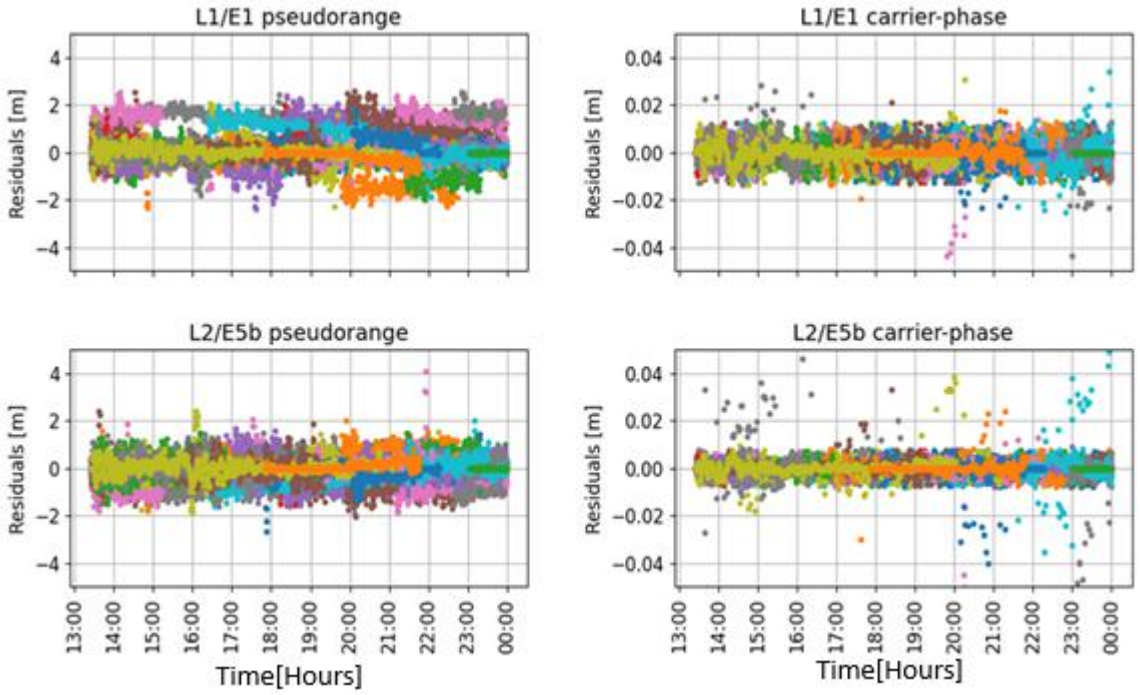


Figure 5.3: Pseudorange and carrier-phase residuals for L1/E1 and L2/E5b signals using CNES corrections in YorkPPP from the rooftop experiment at York University on DOY 223, 2024.

The carrier phase residuals for both frequencies showed remarkable precision with small scatter throughout the 20-hour test, typically +/-0.02 m between the carrier phase measurements and the difference of the range measurements. For fixed solution RTK,

Wübbena et al. (2005) stated that phase residuals should be on the sub-centimetre level. YorkPPP engine can model the receiver phase-centre offsets (PCO) and phase-centre variations (PCV), and the fixed solution remained at centimetre level throughout the 20-hour test period.

The fixed and float solution convergence for the SPARTN analysis (Figure 5.4) differs significantly from the global CNES service. For SPARTN, the fixed solution reached convergence within 9.5 minutes of data processing whereas the float solution required 42 minutes. This extended period of float solution convergence is noteworthy, and indicates that without fixing the integer ambiguities, the filter required additional time to account for regional biases in the atmospheric, ionospheric, and tropospheric datasets provided in the SPARTN High-Precision Atmospheric Correction (HPAC) stream (Li et al., 2022).

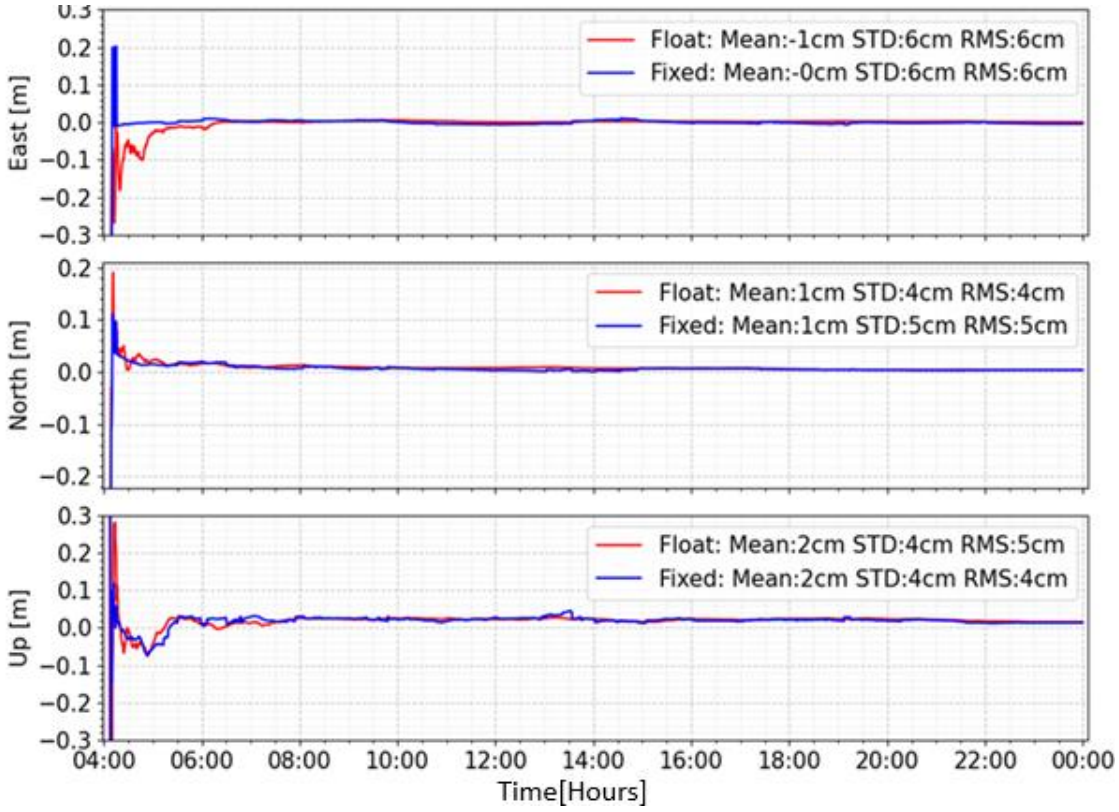


Figure 5.4: ENU errors (float versus fixed solutions) using YorkPPP with SPARTN

corrections in YorkPPP from the rooftop experiment at York University DOY 223, 2024.

The initialization performance of SPARTN correction is illustrated in Table 5.2 and depicted in Figure 5.5. The performance under SPARTN corrections shows a marked difference between the performance of the float and fixed solutions. Although the float solution showed a slow but long-term convergence after 42.00 minutes, the fixed solution reached convergence in a much shorter time of 9.50 minutes, demonstrating a 77% improvement in time-to-fix.

Table 5.2: Performance metrics for dual-frequency positioning: CV and RMS error analysis using SPARTN corrections.

	FL CV (min)	FL hor. rms (cm)	Fl ver. rms (cm)	FX CV (min)	FX hor. rms (cm)	FX ver. rms (cm)
dual freq	42.00	7.13	4.75	9.50	7.23	4.10

The steady-state vertical performance of SPARTN was found to exceed that of the global baseline. The float solution vertical RMS was 4.75 cm, and the fixed solution vertical RMS was 4.10 cm. This high vertical performance is achieved using regional Geographic Area Definition (GAD) grids that provide very accurate local tropospheric corrections. By removing most of the tropospheric delay prior to its inclusion in the estimation filter, SPARTN significantly enhances the performance of the "up" component, allowing it to rapidly achieve a sub-decimetre convergence. Figure 5.5 shows the lower satellite count of 10–18 due to SPARTN service selecting satellites based on the availability of regional atmospheric modelling data. Even though PDOP fluctuates, the vertical component remains robust and has high integrity.

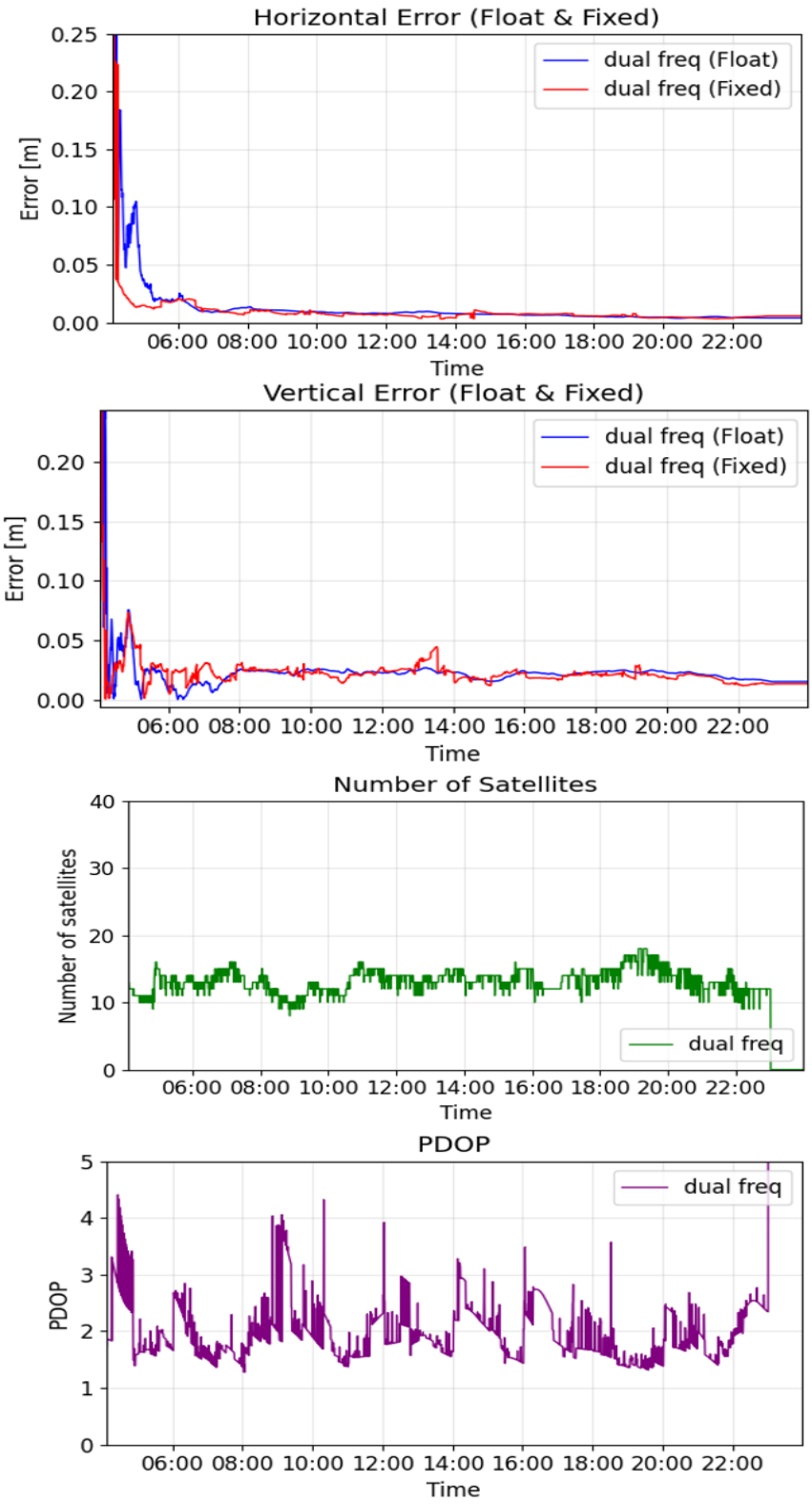


Figure 5.5: Horizontal and vertical positioning performance of float and fixed solutions using YorkPPP with SPARTN corrections, including satellite count and PDOP variation

from the rooftop experiment at York University on DOY 223, 2024.

The integrity of the measurements made by the SPARTN regional solution is confirmed by the residual plots displayed in Figure 5.6. The pseudorange residuals show very small residuals around +/- 2.0 m envelope similar to those obtained by CNES, with slightly more high frequency noise, possibly due to the reduced data time baseline of 20 hours. The residual plots for the carrier phase measurements show negligible change with time, as expected for the metric-level positioning precision provided by SPARTN.

Additionally, a closer look at Figure 5.6 shows that there is a local increase in phase residual volatility from around 20:00–24:00 UTC. According to Li et al. (2022), regional state-space representation (SSR) products such as SPARTN are highly sensitive to ionospheric activity, and their noise can be limited to the resolution of the Geographic Area Definition (GAD) grids. The increase in noise, however, does not lead to an increase of the residuals beyond the functional boundaries of the RTKLIB filter, implying that the SPARTN High-Precision Atmospheric Correction (HPAC) is able to effectively separate and correct for ionospheric and tropospheric delays. As such, the float and fixed vertical ambiguities are still stable.

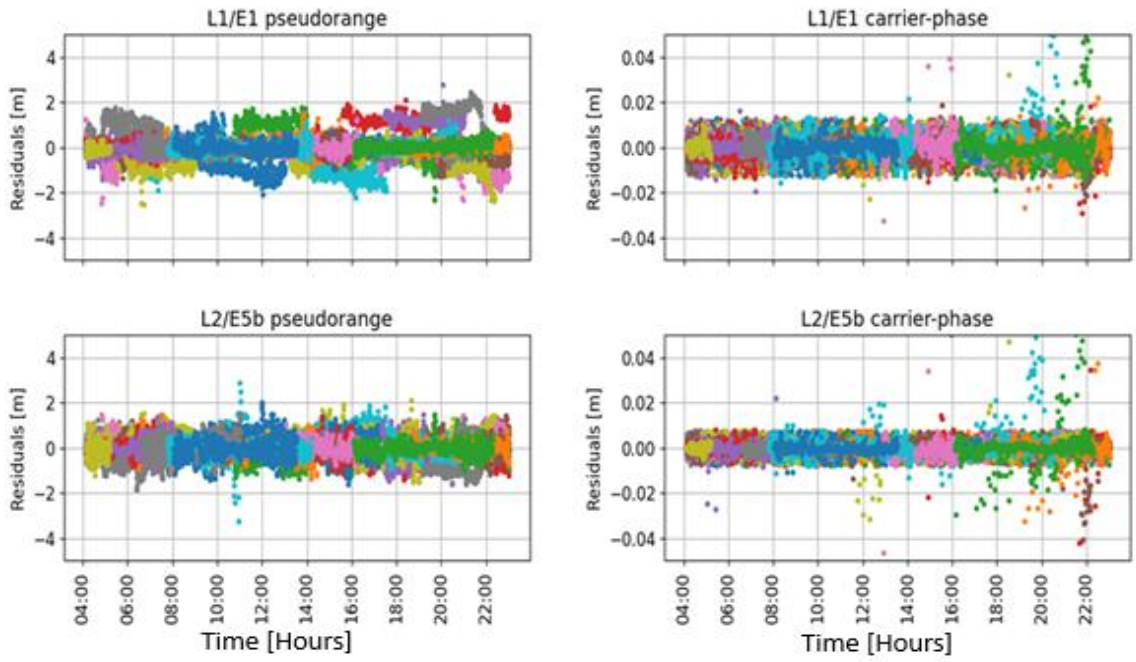


Figure 5.6: Pseudorange and carrier-phase residuals of the rooftop station for L1/E1 and L2/E5b signals using SPARTN corrections in YorkPPP from the rooftop experiment at York University on DOY 223, 2024.

The experimental data confirms that while both CNES and SPARTN achieve centimetre-level results, they serve different operational needs. The fixed solution is the superior choice for time-sensitive applications, consistently reducing initialization and providing higher vertical reliability. The CNES global product is more resilient to satellite fluctuations, whereas the SPARTN regional product offers a significant advantage in vertical precision due to localized atmospheric modelling. These results underscore that for static geodetic applications, the choice between float and fixed processing must be balanced between the required speed of initialization and the necessary vertical accuracy.

From the experimental data presented in Table 5.3 from roof top of York University, there is a performance trade-off between the two correction services provided by CNES and SPARTN. Although both systems offer accuracy on the order of centimetres, they serve

two different objectives in operational terms. The largest improvement is in terms of convergence efficiency. CNES reaches a float solution 30 minutes early, i.e. 71.4% better than SPARTN. In addition, the horizontal reliability is better, especially in terms of north component accuracy. In this case, CNES is 60% better than SPARTN. Such characteristics make it a good choice for rapid deployment and high horizontal accuracy. In contrast to the results obtained for the horizontal component, performance in the vertical domain is reversed, with SPARTN delivering much better stability for the up (vertical) component. Stability of 4 cm Fixed RMS was achieved, representing an improvement of 60% over the 10 cm obtained by CNES.

Table 5.3: Comparative analysis of solution convergence and east, north and up precision: CNES versus SPARTN corrections.

Metric	Solution	SPARTN	CNES	% Difference
Convergence Time	Float (FL)	42.00 min	12.00 min	71.4% (CNES Faster)
	Fixed (FX)	9.50 min	8.00 min	15.8% (CNES Faster)
East RMS	Float (FL)	6 cm	6 cm	0% (Equal)
	Fixed (FX)	6 cm	5 cm	16.7% (CNES Better)
North RMS	Float (FL)	4 cm	1 cm	75.0% (CNES Better)
	Fixed (FX)	5 cm	2 cm	60.0% (CNES Better)
Up (Vertical) RMS	Float (FL)	5 cm	11 cm	54.5% (SPARTN Better)
	Fixed (FX)	4 cm	10 cm	60.0% (SPARTN Better)
Horizontal RMS	Float (FL)	7.13 cm	5.73 cm	19.6% (CNES Better)
	Fixed (FX)	7.23 cm	5.05 cm	30.2% (CNES Better)

Table 5.4 provides a comprehensive comparison of average performance metrics between CNES and SPARTN correction streams across four distinct rooftop datasets. The results demonstrate a clear hierarchy in both initialization speed and horizontal stability, with CNES emerging as the more efficient service.

The largest gain in performance is found in the convergence efficiency, with CNES achieving a float fix in 9.25 minutes and a fixed solution in 6.00 minutes. This translates to an improvement of 76% and 68% respectively over the initialization times found using SPARTN. In terms of steady-state accuracy YorkPPP derived solutions using CNES data achieve a best horizontal RMS of 4.02 to 4.63 cm, which averages to performance that is nearly 2.5 times better than the 11.7 cm achieved with SPARTN. While CNES is best for both horizontal and time domain solutions, the vertical RMS performance is found to be similar and ranges from 11.5 to 13.8 cm. In summary, CNES provides best performance for quick initialization and highest horizontal accuracy.

Table 5.4: Comparative analysis of average solution convergence and east, north and up precision: CNES versus SPARTN corrections for four dataset.

Metric	Solution	CNES (Average)	SPARTN (Average)	Observation
Convergence (CV)	Float (FL)	9.25 min	38.50 min	CNES is ~76% faster
	Fixed (FX)	6.00 min	19.00 min	CNES is ~68% faster
Horizontal RMS	Float (FL)	4.02 cm	11.68 cm	CNES is more precise
	Fixed (FX)	4.63 cm	11.74 cm	CNES is more precise
Vertical RMS	Float (FL)	11.50 cm	13.77 cm	Comparable
	Fixed (FX)	12.01 cm	13.12 cm	Comparable

5.1.2 Empirical Validation of Low-Cost Hardware Performance via YorkPPP

To assess the performance of SSR corrections on low-cost mass-market GNSS receiver's additional rooftop testing was conducted on DOY 239, 2024 using the YorkPPP processing engine to process SSR correction streams from CNES and SPARTN. A u-blox ZED-F9P dual frequency receiver was used in conjunction with a low-cost antenna mounted on the York University rooftop testing platform. Test results for both the float and the ambiguity-fixed PPP solutions are presented and performance comparisons between the two correction services made under identical test conditions.

The time series of the east, north and up coordinate components for the CNES-based YorkPPP solution are provided in Figure 5.7. For both the float and fixed solutions, the east and north components showed a stable performance at the decimetre level. The east component shows an RMS error of about 41 cm for both solutions, with a corresponding mean bias of about -30 cm for the float solution and -27 cm for the fixed solution. The corresponding values for the north component are an RMS error of about 30 cm and 29 cm for the float and fixed solutions, respectively, with mean biases of about 9 cm and 8 cm, respectively. Hence, the ambiguity fixing provided only a marginal improvement in the horizontal positioning performance for this experiment. In strong contrast, the up-component showed large residuals and high scatter, especially during the initial phase of the solution convergence. The corresponding RMS error values are 341 cm for the float solution and 350 cm for the fixed solution, with mean biases of about 66 cm for both solutions. The high dispersion of the height component is likely caused by a combination of residual multipath effects, antenna phase center variations as well as increased noise of the low-cost receiver and antenna.

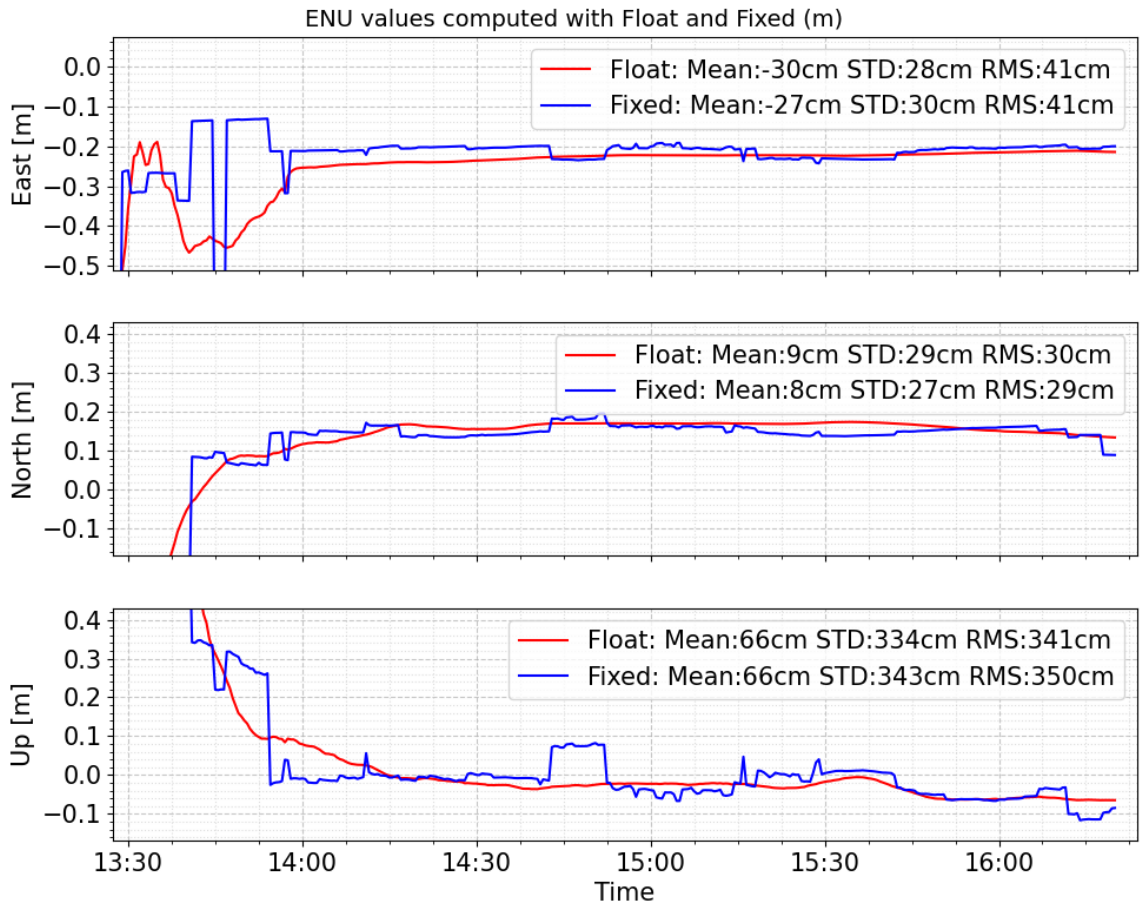


Figure 5.7: ENU errors (float versus fixed solutions) using YorkPPP with CNES corrections in YorkPPP from the rooftop experiment using low-cost hardware at York University on DOY 223, 2024.

Figure 5.8 is a summary of the YorkPPP analysis using the CNES corrections. The RMS errors for the horizontal and vertical components of the float and fixed solutions are presented. The horizontal RMS errors for the horizontal components were approximately 50.83 cm (float solution) and 49.62 cm (fixed solution), thus consistent decimetre accuracy was maintained for the horizontal components throughout the experiment. The corresponding RMS errors for the vertical components were much larger and approximately 340.87 cm (float solution) and 349.81 cm (fixed solution) respectively.

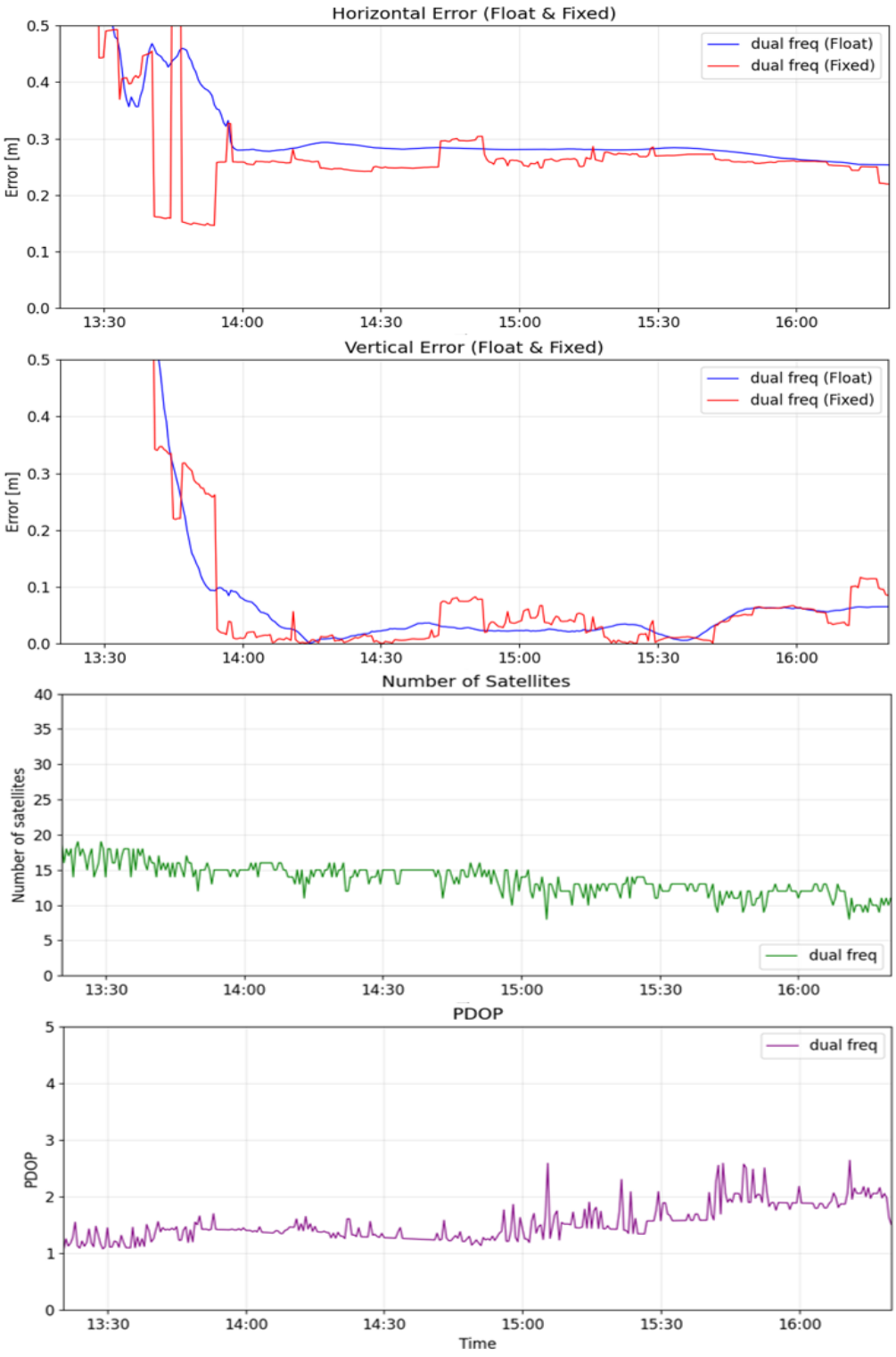


Figure 5.8: Horizontal and vertical positioning performance of float and fixed solutions using YorkPPP with SPARTN corrections, including satellite count and PDOP variation

from the rooftop experiment at York University using low-cost hardware on DOY 239, 2024.

As previously stated, the receiver maintained a stable number of satellites tracked throughout the experiment, approximately 10–18 were available for most of the experiment, and the PDOP remained below 2.5 for most of the experiment, thus the satellite geometry did not pose any restrictions to the solution. As can be observed from the results, the CNES corrections, using a low-cost, mass-market GNSS receiver, were able to deliver reliable, at lane-level, horizontal accuracy, whereas the vertical component of the solution was more sensitive to errors, due to several environmental and receiver-related error sources that had not been removed from the solution.

The east, north and up coordinate time-series for the YorkPPP solution, employing the SPARTN orbit for correction, are depicted in Figure 5.9. The horizontal components for both the float and fixed solutions track a stable decimetre position. For the east component, the RMS errors for the float and fixed solutions are approximately 28 cm and 30 cm, respectively. The corresponding mean biases for the float and fixed solutions are approximately −17 cm and −16 cm, respectively. The north component for both the float and fixed solutions have RMS errors of approximately 46 cm and 49 cm, respectively, with corresponding mean biases of approximately 16 cm for both the float and fixed solutions. Compared to the CNES-based experiment the SPARTN solution exhibits a smoother start-up and less scatter for the horizontal components during the initial phase of convergence. The up-component for the float and fixed solutions have RMS errors of approximately 209 cm and 203 cm, respectively, with corresponding mean biases of approximately 63 cm and 61 cm, respectively. The errors in the vertical direction are substantially larger than the

corresponding errors for the horizontal components. However, the dispersion in the vertical errors has decreased, resulting in a more robust correction stream for low-cost rooftop operations utilising the SPARTN solution.

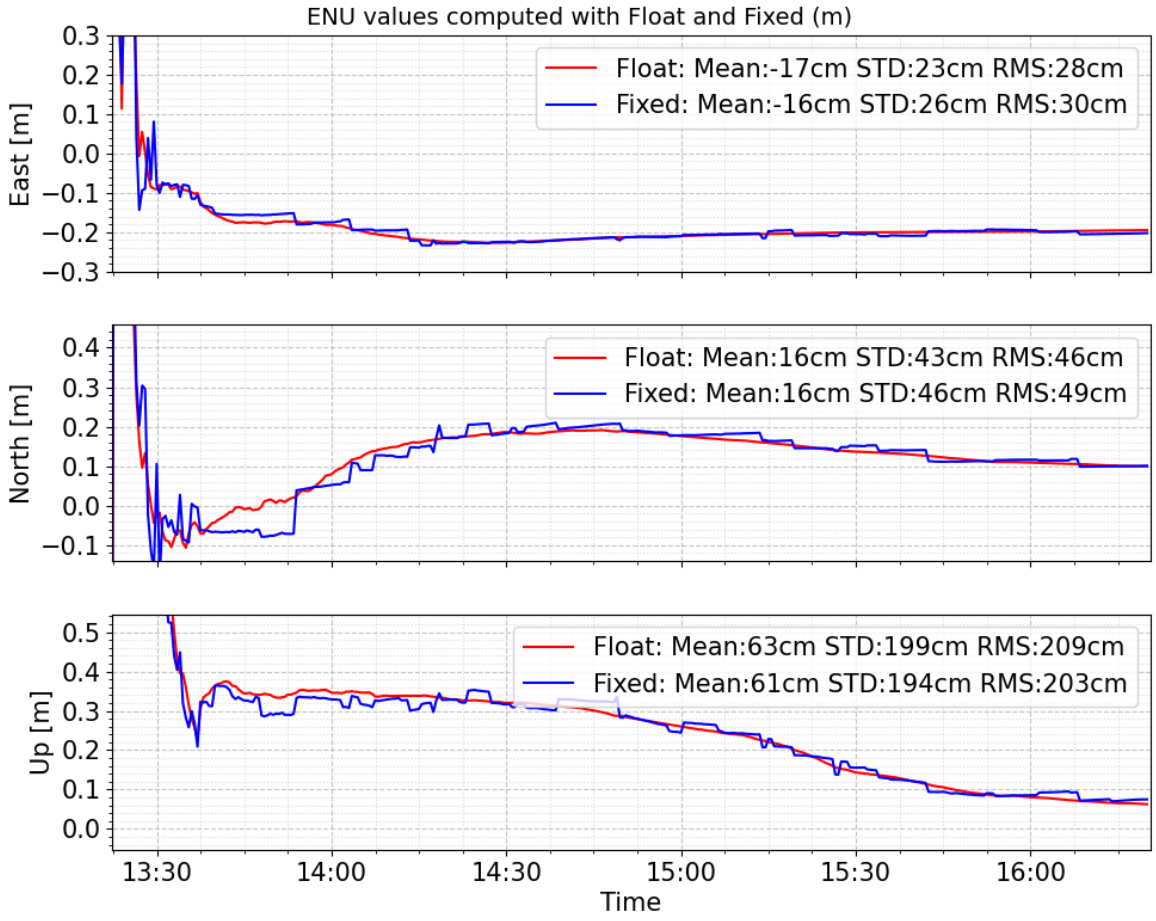


Figure 5.9: ENU errors (float versus fixed solutions) using YorkPPP with SPARTN corrections in YorkPPP from the rooftop experiment using low-cost hardware at York University on DOY 223, 2024.

A summary of the YorkPPP results from the SPARTN-based YorkPPP experiment is provided as Figure 5.10. The average horizontal RMS error for the horizontal measurements was 53.88 cm for the float solution and 57.56 cm for the fixed solution. The average vertical RMS error for the height measurements was 208.80 cm for the float

solution and 203.17 cm for the fixed solution. The results show a large improvement for the vertical measurements compared to the CNES-based results. The receiver tracked between 10 and 15 satellites for the entire observation session. The PDOP values were between 1.8 and 3.0 for the entire session. The results show that the SPARTN correction can be used for lane-level horizontal positioning using low-cost mass-market GNSS receiver and that the vertical accuracy and smoothness of convergence are better than the CNES-based results.

Both CNES and SPARTN SSR correction streams can bring decimetre horizontal accuracy to inexpensive commercial GNSS receivers. The horizontal RMS values of both experiments remain close to 0.5 m and are thus smaller than the width of a standard road lane of approximately 3.5 m, i.e. they are sufficient for applications requiring lane-level accuracy for vehicles. However, the SPARTN based solution clearly outperforms the CNES solution in terms of vertical accuracy of the vertical components and in terms of smoothness of the convergence of the lines in both rooftop and receiver-based experiments. These results thus clearly confirm our previous findings on the potential of advanced SSR-based PPP correction services to enable accurate lane-level vehicle navigation using low-cost commercial GNSS receivers, in this case even when processed with a basic PPP engine such as YorkPPP.

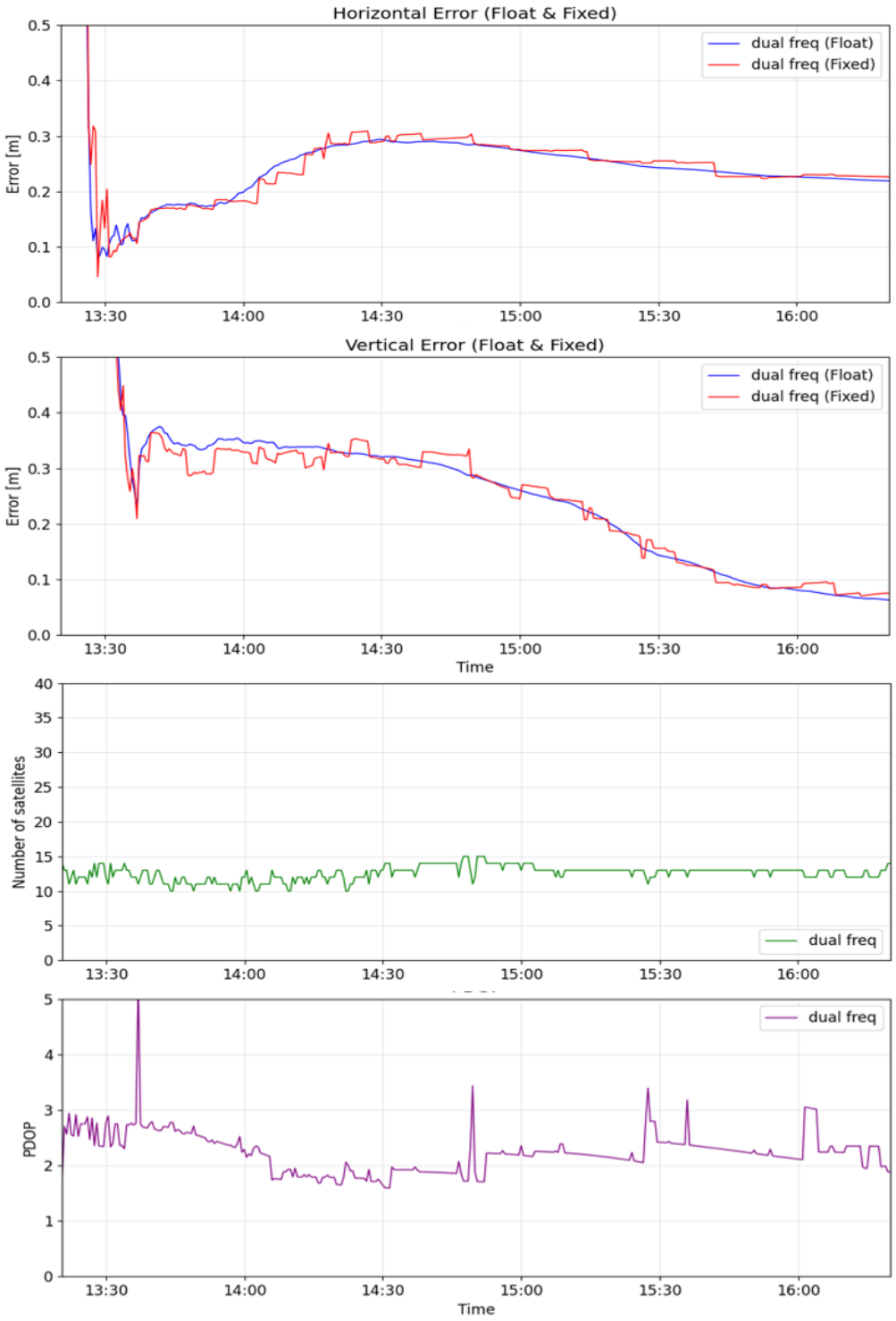


Figure 5.10: Horizontal and vertical performance of float and fixed solutions using YorkPPP with CNES corrections, including satellite count and PDOP variation from the rooftop experiment using low-cost hardware on DOY 239, 2024.

5.2 Static Validation: QUIN IGS Station

The statistical validation of the YorkPPP processing engine is presented based on the International GNSS Service (IGS) tracking station QUIN00USA. Although the data from four IGS tracking stations (ALGO, PIE1, QUIN, and NRC1) yielded consistent results for the processing performance of the YorkPPP engine, a detailed test based on data from the IGS tracking station QUIN00USA was conducted and presented.

The skyplot in Figure 4.4 from previous chapter shows that there is sufficient spatial diversity across multiple constellations (GPS, GLONASS, Galileo, BeiDou) to enable good PDOP for point positioning. The results from the YorkPPP engine can then be compared against known IGS solution positions for the site QUIN to assess the absolute accuracy and convergence performance of the engine.

5.2.1 Evaluation of Orbit, Clock, and Signal Bias Correction

The baseline for any Precise Point Positioning (PPP) solution is the accuracy of the satellite orbit and clock products. To evaluate the integrity of the SPARTN stream, the satellite-specific errors are decomposed into a local orbital coordinate system.

As illustrated in Figure 5.11, radial component (the most sensitive measurement to vertical height) is the most stable and has errors less than ± 2.5 m. However, the along-track and cross-track component errors have the greatest fluctuation. The along-track errors exhibit the greatest peak error, reaching up to 7.5 m, and indicate difficulties with orbit determination and satellite motion prediction. The cross-track error is most stable, yet intermediate in nature, oscillating around ±5 m. This error directly affects the horizontal positioning reliability, as it is perpendicular to the satellite's orbital plane. The clock total error exhibits a high-frequency noise floor of ± 5 m, which indicates the difficulty of time synchronisation over long distances.

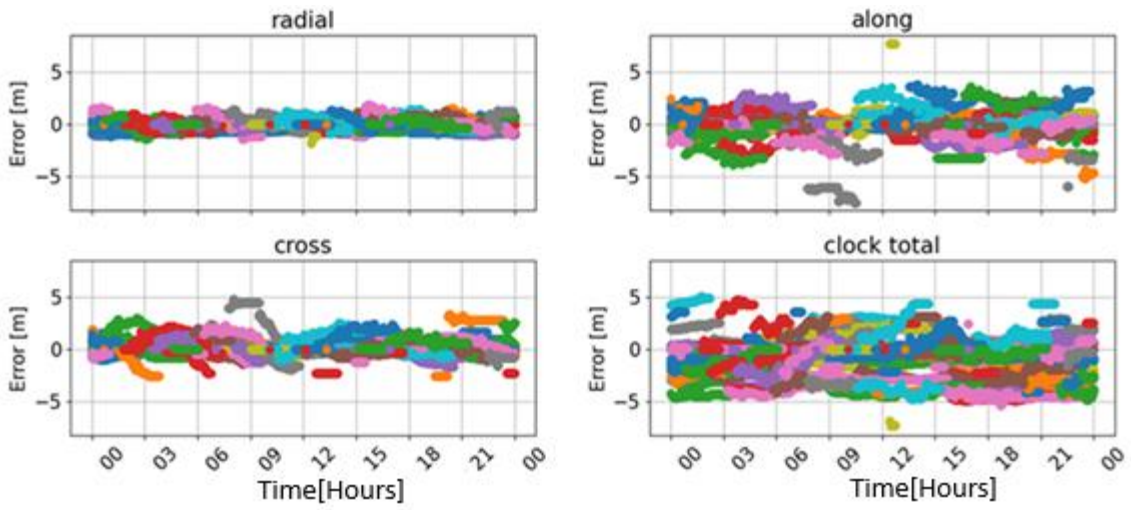


Figure 5.11: SPARTN orbit and clock correction errors on DOY 222, 2024: radial, along-track, and cross-track orbit correction components, along with total clock correction error across all satellites.

Figure 5.12 shows that the uncertainties in the orbital positions are related to the signal bias. The P1 and P2 code bias is caused by satellite and receiver hardware delays. The pseudorange residuals have variations of approximately ±2 to ±4 m. The variations are caused by receiver measurement noise, local multipath, and residual atmospheric propagation errors. The L1 carrier-phase bias is small and tightly clustered around zero. This means that the carrier-phase measurements have a stable and consistent measurement behaviour and can be used as a high-precision reference for the positioning solution. The L2 bias is larger and more variable, with a distribution of –4 m to +5 m.

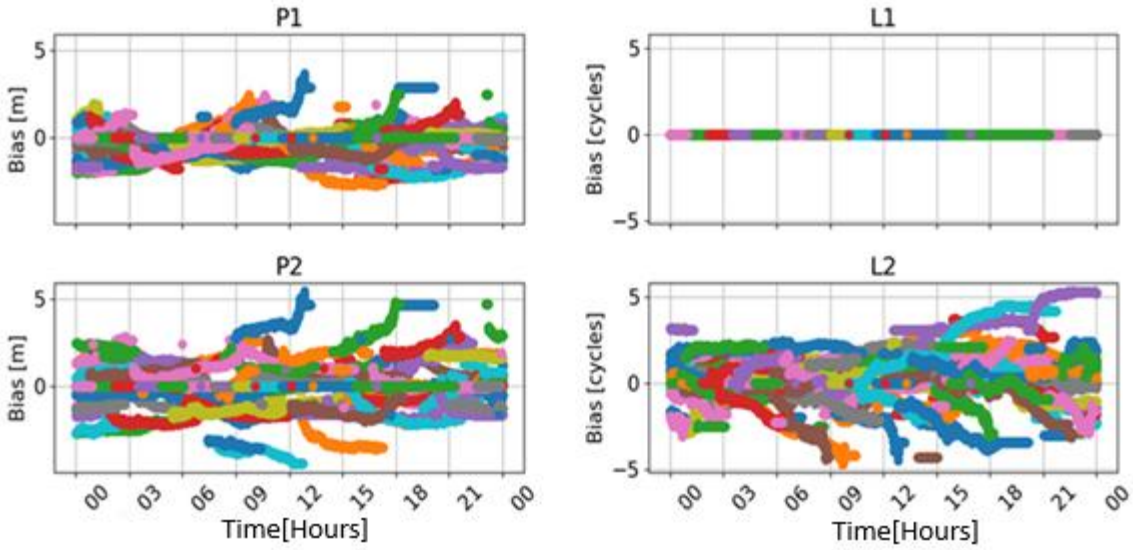


Figure 5.12: SPARTN correction biases for code (P1, P2) and carrier-phase (L1, L2) signals on DOY 222, 2024.

Figure 5.13 further investigates these errors as a function of satellite elevation. Above a 40° elevation angle, GPS maintains a compact distribution (within ±1 m), while GLONASS demonstrates distinct "banding" in its along-track and cross-track errors. This suggests that the GLONASS orbital paths are less precisely modelled than GPS, likely a consequence of its FDMA signal structure.

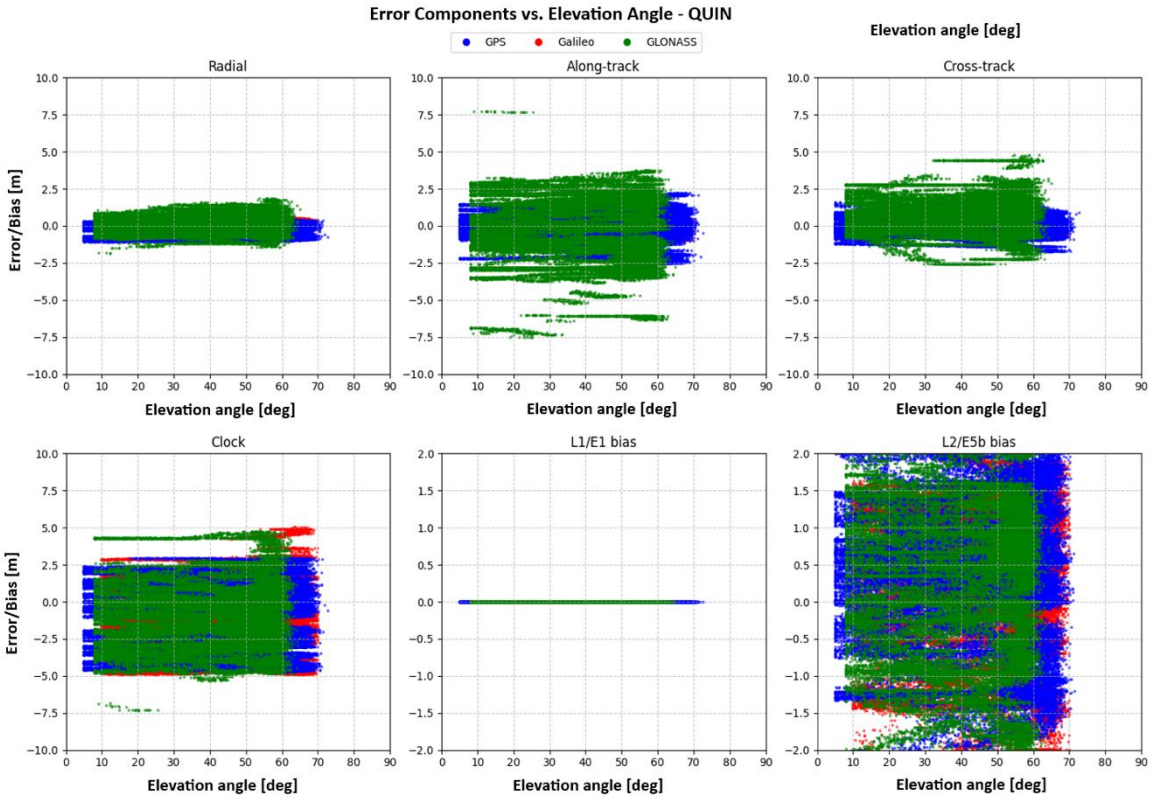


Figure 5.13: SPARTN orbit, clock, and signal bias errors versus elevation angle at the QUIN IGS station on DOY 222, 2024.

Achieving centimetre-level accuracy requires the PPP engine to neutralize unmodelled atmospheric delays. Time series presented in Figure 5.14 illustrate the diurnal behaviour of the ionosphere and troposphere delay affecting the satellite signal. The solar-driven ionospheric errors are seen to peak at 20–25 m at 18:00 local time. Meanwhile, the tropospheric path delay exhibits very sharp peaks of up to 20–30 m at low elevation angles where the signal must pass through an increased thickness of tropospheric mass.

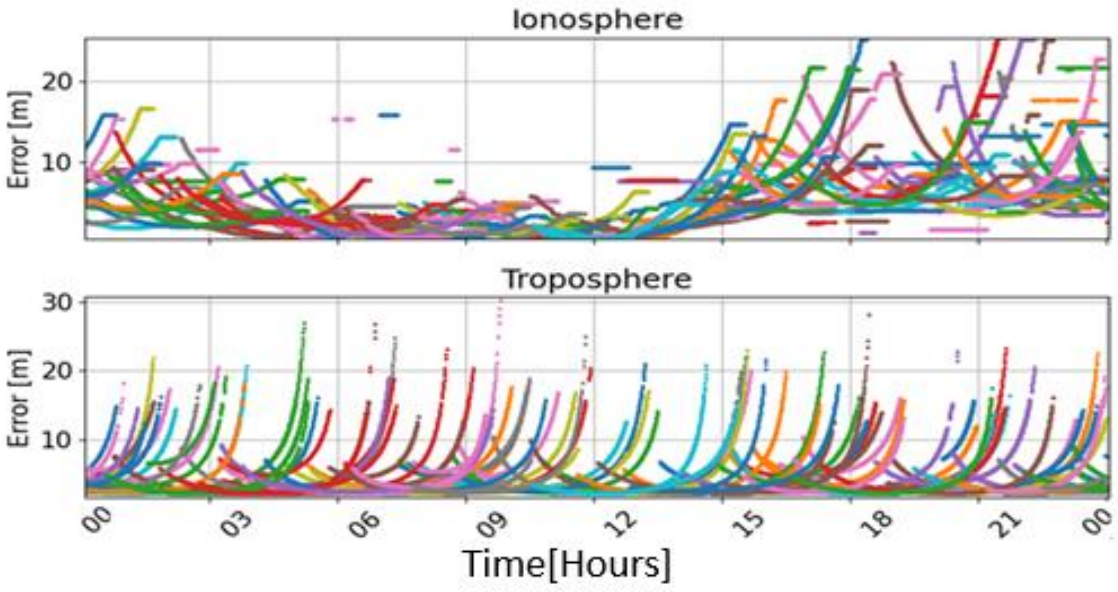


Figure 5.14: Time series of SPARTN ionospheric and tropospheric correction errors across satellites on DOY 222, 2024.

The effectiveness of the YorkPPP engine in mitigating these effects is validated by the residual analysis in Figure 5.15. The post processed pseudorange residuals are maintained within ±2m as the atmosphere remains active. The carrier-phase residuals which are the ultimate indicator of solution precision, are grouped tightly around the mean with a standard deviation of ±0.04m (4cm). This clearly shows that the combination of corrected state-space representation (SSR) information along with tropospheric mapping functions is adequate in isolating the geodetic signal from the vast amount of atmospheric noise.

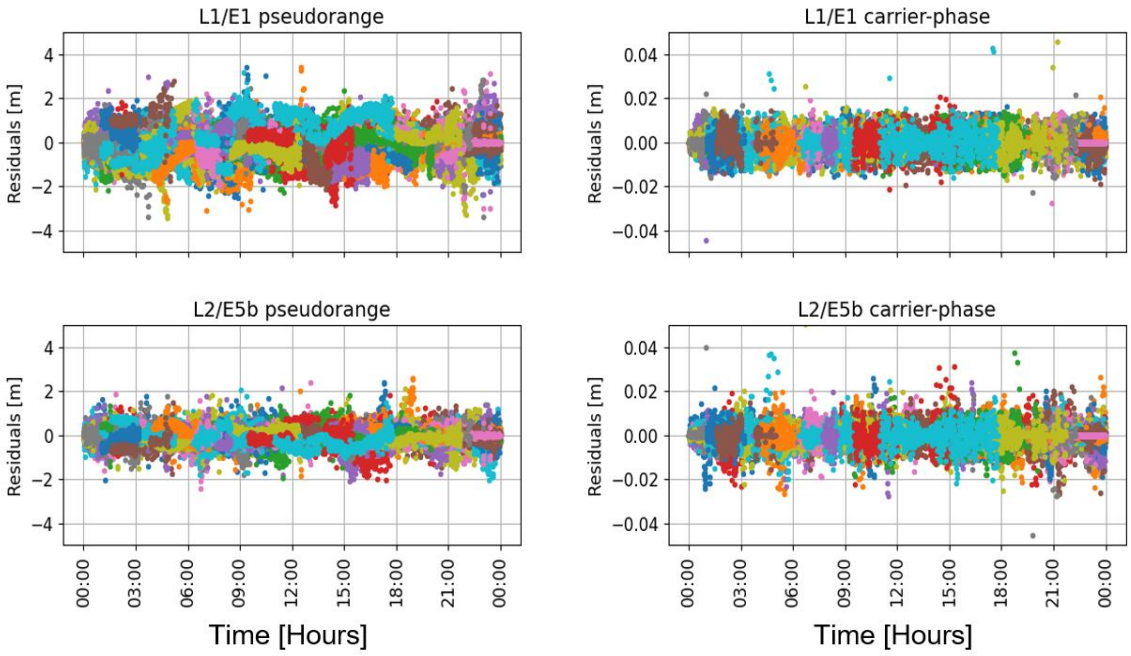


Figure 5.15: Time series of pseudorange and carrier-phase residuals for L1/E1 and L2/E5b signals after applying SPARTN corrections on DOY 222, 2024.

Figure 5.16 presents the 24-hour east-north-up error time series for the SPARTN-corrected solution. The horizontal component of the solution has high stability for both the float and fixed solutions. The north error is the most precise and centres around 0 cm. The east error has a small systematic bias for both solutions and is found to be approximately -6 cm. The vertical (up) component of the error also reaches a higher level of stability and oscillates around ±10 cm before cantering around -5 cm. The high degree of overlap between the float (red) and fixed (blue) lines suggests that for the SPARTN stream at this station, integer ambiguity resolution provides a modest refinement rather than a transformative leap in coordinate precision.

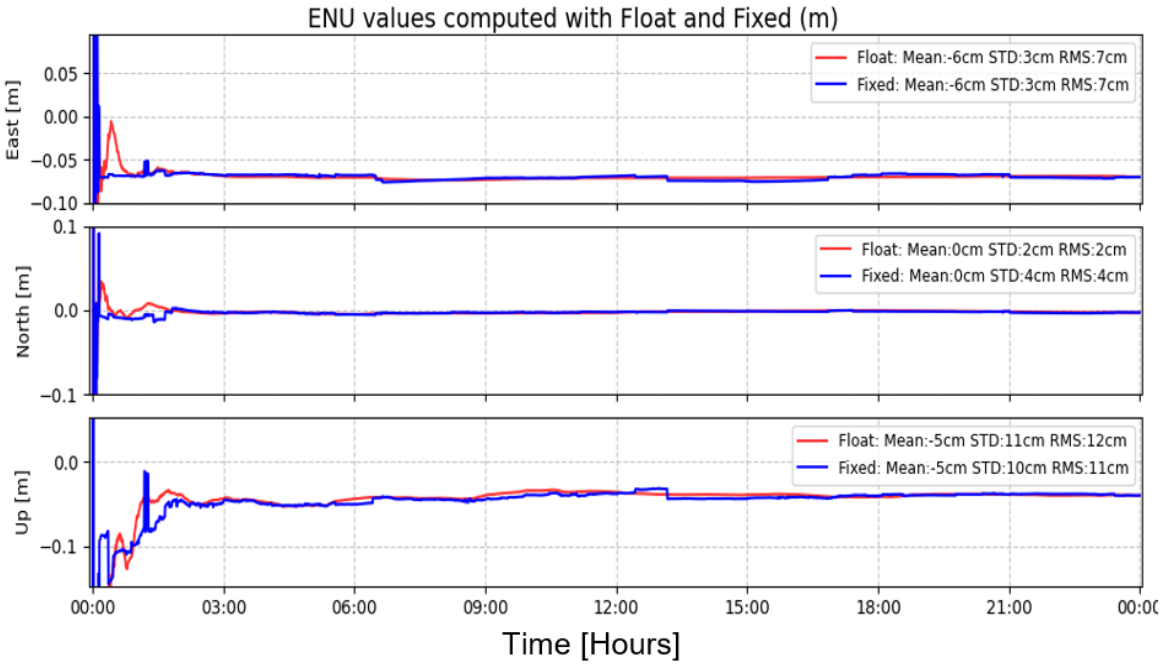


Figure 5.16: Time series of east, north, and up (ENU) positioning errors for float and fixed solutions with SPARTN corrections applied on DOY 222, 2024.

A detailed assessment of the solution convergence and geometry for the SPARTN solution at QUIN station is provided in Figure 5.17 and Table 5.4. Good visibility, of up to 25 satellites, was observed throughout the 24-hour test period with all constellations providing highly favourable geometry, leading to very low Position Dilution of Precision (PDOP) solutions ranging from 0.9 to 1.5.

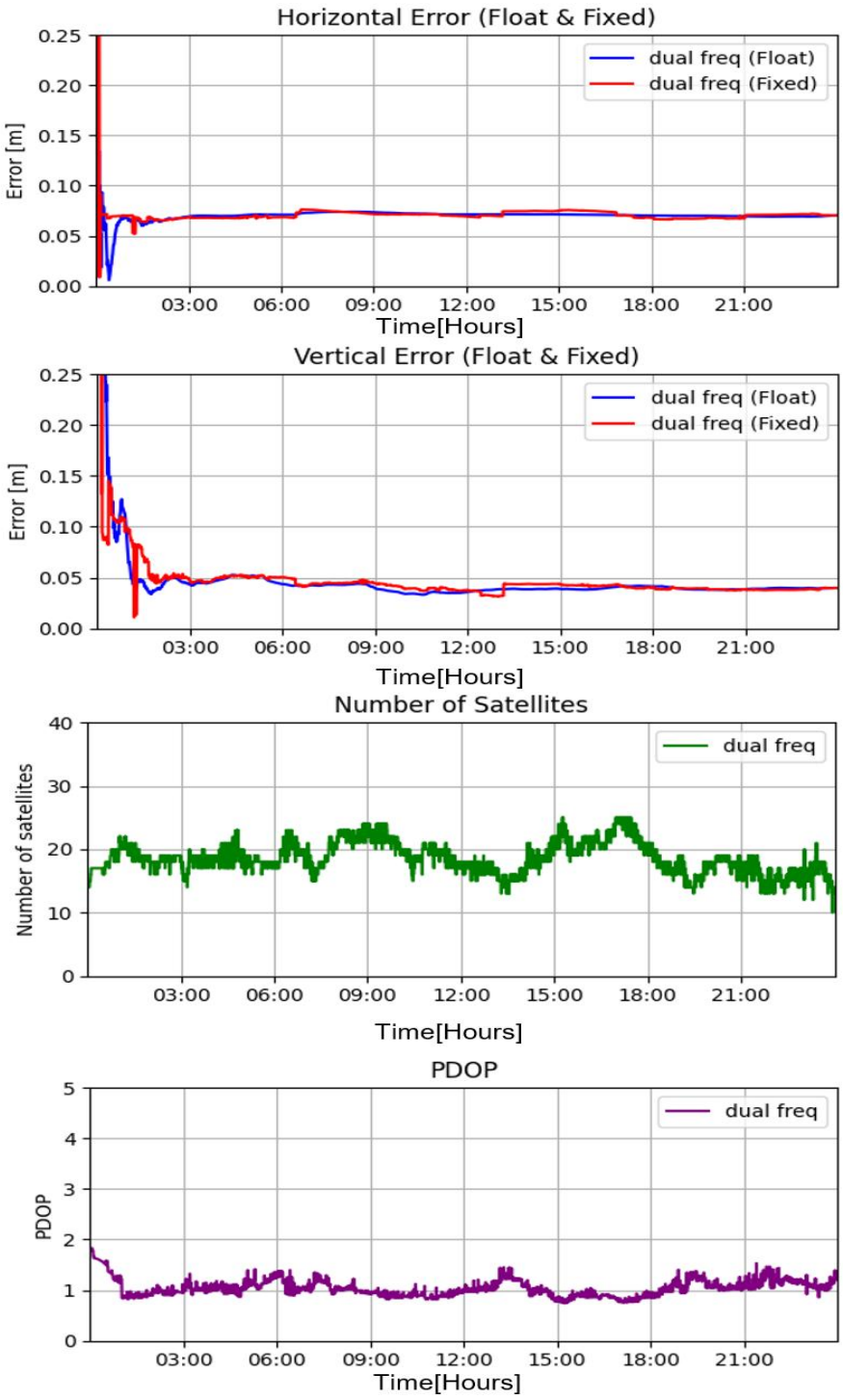


Figure 5.17: Horizontal and vertical positioning errors, satellite visibility, PDOP, and convergence metrics at the QUIN IGS station on DOY 222, 2024, using SPARTN corrections for float and fixed solutions.

Table 5.5 summarizes results of the test performed under good geometry conditions. The float and fixed solutions both converged in a short period of time, 7.50 and 6.50 minutes, respectively. The RMS of the residuals for the horizontal components both remained below 9 cm whereas for the vertical components the RMS was as high as 12.48 cm for the float solution and 11.63 cm for the fixed solution. These metrics suggest that while the SPARTN stream enables quick initialization, the vertical residuals remain relatively high compared to geodetic-grade standards.

Table 5.5: Performance metrics for dual-frequency positioning: CV and RMS error analysis using SPARTN corrections.

	FL CV (min)	FL hor. rms (cm)	Fl ver. rms (cm)	FX CV (min)	FX hor. rms (cm)	FX ver. rms (cm)
dual freq	7.50	7.93	12.48	6.50	8.96	11.63

To understand the physical context of these errors, Figure 5.18 illustrates the distribution of satellite observations by elevation angle across the GPS, GLONASS, and Galileo constellations. Much of the data falls within the 30° to 70° elevation range with nearly uniform distribution over this angle range for GPS. Galileo is particularly noteworthy as it contributes 47% of the highest elevation angle data points (70°–80°). For tropospheric delay mitigation, the satellite signal with the shortest path through the atmosphere travels up through the zenith. Below 80° there are no observations due to the latitude of the QUIN station, creating a small blind spot directly overhead for the current GNSS constellations.

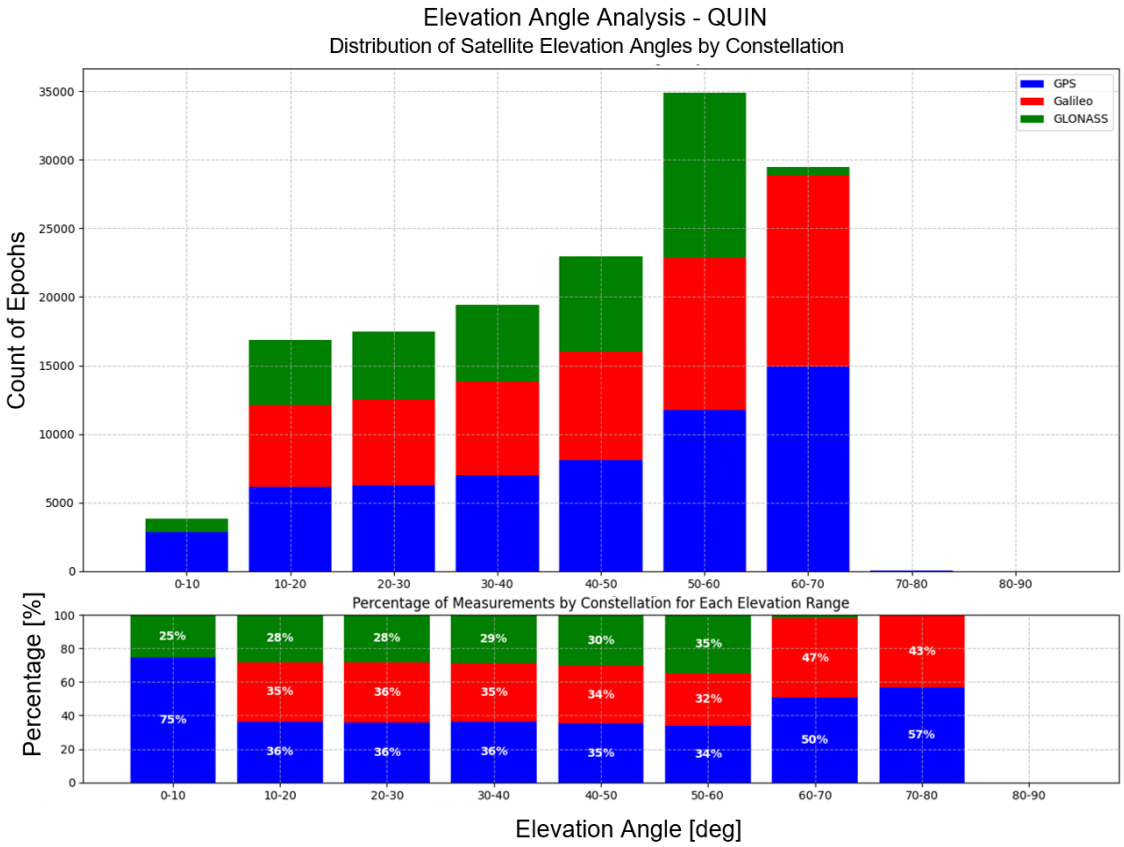


Figure 5.18: Percentage of satellite observations by elevation angle and constellation at QUIN station.

The CNES-corrected results, shown in Figure 5.19 and Table 5.6, represent a significant performance benchmark relative to the SPARTN results. The horizontal RMS is comparable to the performance seen with the SPARTN data and amounts to 8.70 cm for float and 9.04 cm for fixed. However, the vertical performance is significantly better for the CNES solution, reaching 5.76 cm for float and 6.54 cm for fixed, representing an improvement of 53%. The solution exhibits excellent temporal stability with vertical fluctuations limited to ±2–3 cm, providing a very smooth error performance as opposed to the ±5 cm fluctuations seen with the SPARTN data.

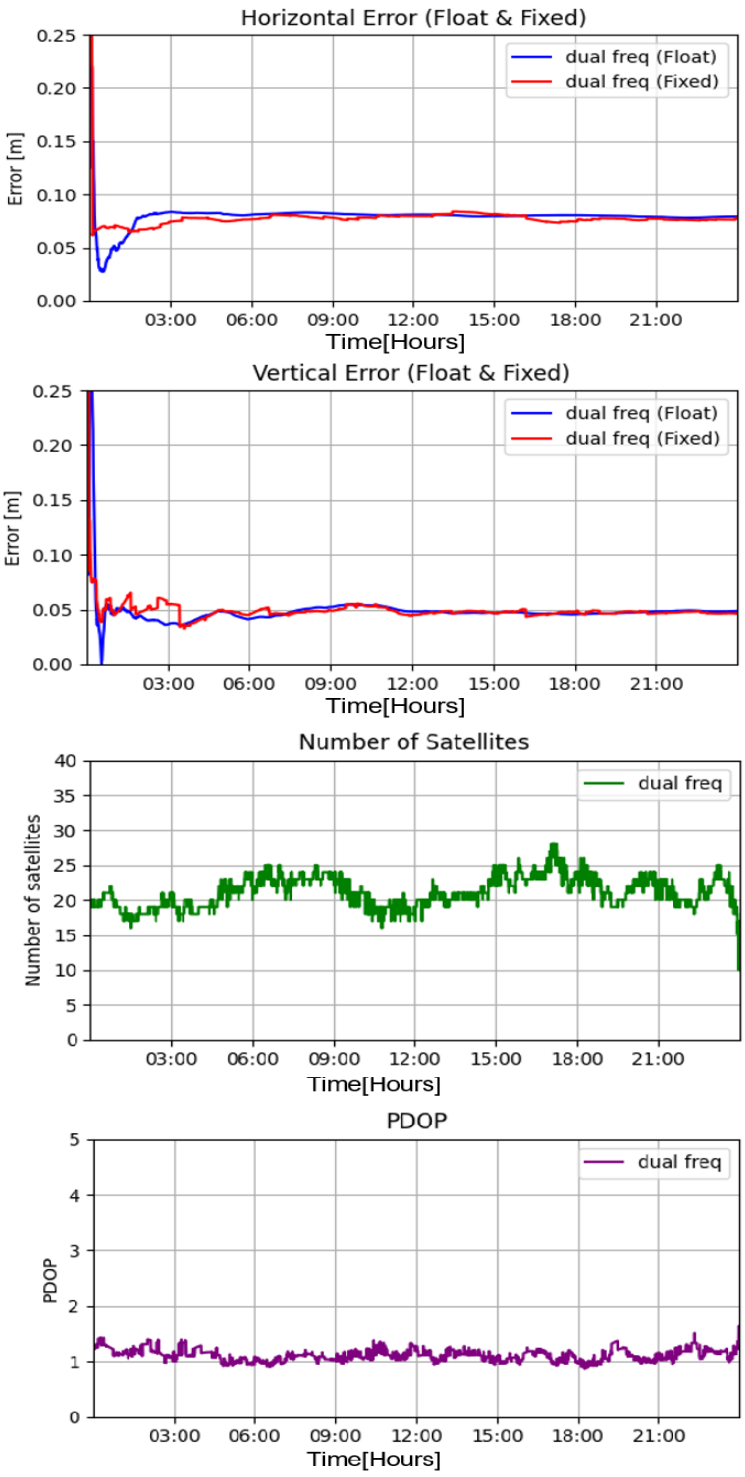


Figure 5.19: Horizontal and vertical positioning errors, satellite visibility, PDOP, and convergence metrics at the QUIN IGS station on DOY 222, 2024, using CNES corrections for float and fixed solutions.

The performance difference between the two correction streams is likely due to the more advanced tropospheric zenith delay (ZTD) modelling and more accurate clock corrections provided within the CNES product. The YorkPPP engine takes advantage of the high-elevation satellites and achieves exceptionally stable PDOP values (averaging around 1.0) with large numbers of tracking satellites (averaging over 20 in view). Although float convergence time is slightly increased at 10 minutes, fixed solution convergence is faster at 6.5 minutes. Vertical positioning accuracy for the fixed solution is significantly better than that obtained with the SPARTN product.

Table 5.6: Performance metrics for dual-frequency positioning: CV and RMS error analysis using CNES corrections.

	FL CV (min)	FL hor. rms (cm)	Fl ver. rms (cm)	FX CV (min)	FX hor. rms (cm)	FX ver. rms (cm)
dual freq	10.00	8.70	5.76	6.50	9.04	6.54

5.2.2 Multi-Constellation Impact and Statistical Validation

Performance with constellation diversity is presented in Figure 5.20 and Table 5.7 for GPS-only (G), GPS+GLONASS (GR) and GPS+GLONASS+Galileo (GRE) data sets. The large initial error of 0.25 m is seen to drop quickly to a stable error performance within the first hour of data collection time. The inclusion of GLONASS and Galileo in conjunction with GPS smooths the error transition by significantly reducing the error oscillations characteristic of the sole use of GPS. The horizontal error standard deviation in the long-term limit is reduced below 0.10 m for all three data set configurations.

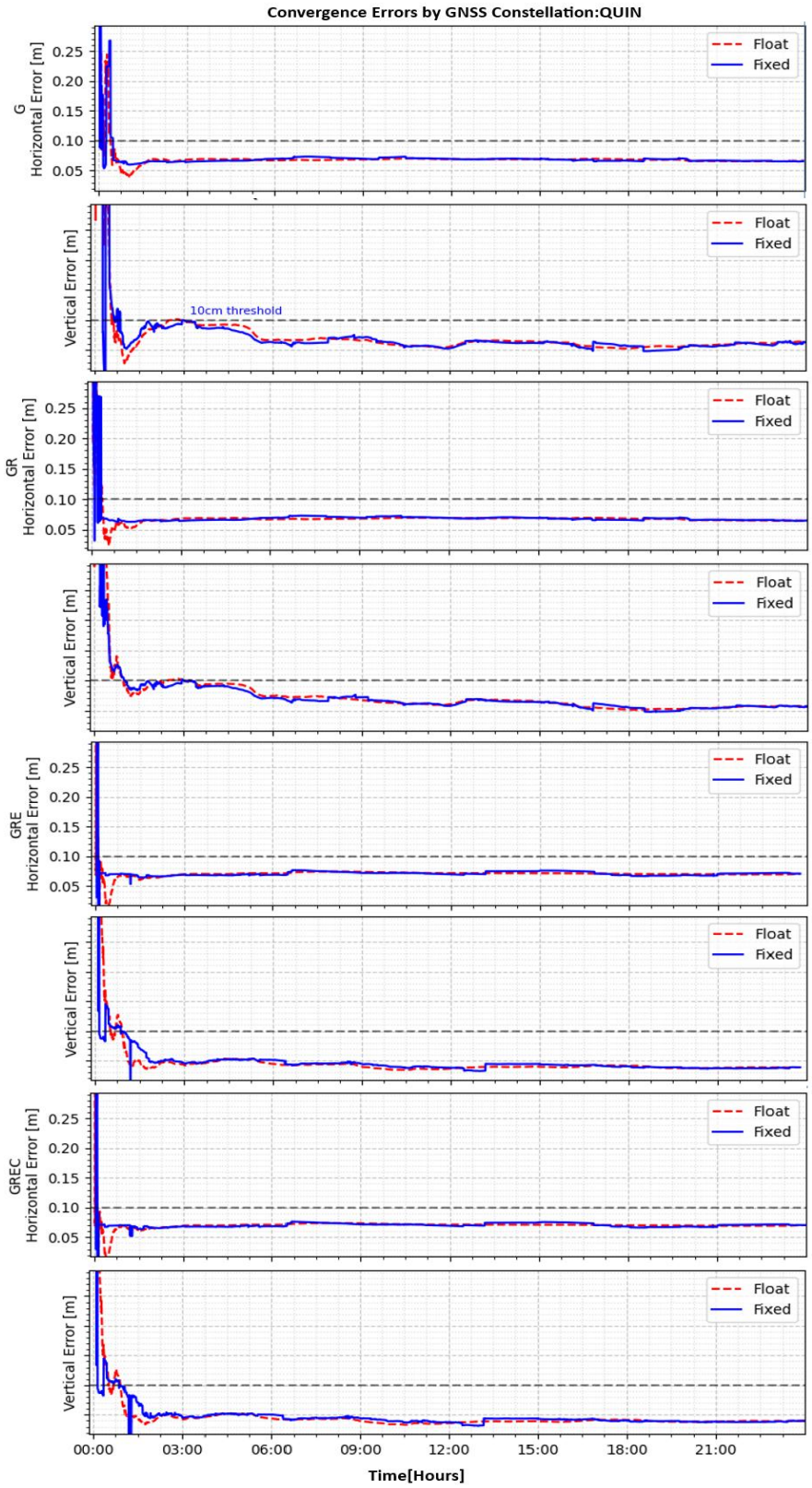


Figure 5.20: Horizontal and vertical positioning error convergence by GNSS

constellation (GPS, GLONASS, Galileo, and BeiDou) at the QUIN IGS station on DOY 222, 2024, using SPARTN corrections and comparing float and fixed solutions.

Comparing the performance metrics in Table 5.7 shows a dramatic reduction in fixed convergence time (20 minutes) to only 6.5 minutes (67.5% reduction) by upgrading from a dual constellation (GR) to a triple constellation (GRE) architecture. The up component benefits the most with RMS reducing from 6.4 cm (GPS only) down to 3.8 cm. Whilst additional constellations such as GPS, GLONASS and BeiDou are gradually accepted as becoming available, a more surprising observation for this location is that the three systems already form the point of diminishing returns and that there is little to be gained by additionally tracking the fourth constellations. Our results show that the critical factor for fastest possible initialization and best vertical performance for high precision geodetics is the combination of all systems, particularly the integration of Galileo.

Table 5.7: Summary of convergence time and horizontal, vertical, and 3D RMS positioning errors for float and fixed solutions by GNSS constellation (GPS, GLONASS, Galileo, BeiDou) at QUIN station.

Constellation	**Pre-convergence**				**Post-convergence**			
	CV [min]	Float Hor RMS [cm]	Float Up RMS [cm]	Float 3D RMS [cm]	CV [min]	Fixed Hor RMS [cm]	Fixed Up RMS [cm]	Fixed 3D RMS [cm]
G (GPS)	25.0	6.6	6.4	9.2	30.0	6.5	6.2	9.0
GR (+GLO)	22.5	6.5	5.7	8.7	20.0	6.5	5.7	8.6
GRE (+GAL)	7.5	6.9	3.8	7.9	6.5	7.1	3.8	8.0

The comprehensive evaluation of the YorkPPP engine's versatility is shown in Tables

5.8 and 5.9 which present the comparative performance metrics across three distinct stations: ALGO, NRC1, and QUIN. This analysis reveals a consistent performance trade-off between the SPARTN and CNES correction streams, highlighting a clear divergence between initialization speed and steady-state precision.

SPARTN solutions are found to be significantly faster at initialization than those obtained by CNES. The average time to solution for the float SPARTN solutions was 12.67 minutes, representing a 27.6% improvement over the average time of 17.50 minutes required by CNES. The average time to FX solution for SPARTN was 7.50 minutes, representing a 33.8% improvement over the average time to solution for CNES FX solutions. At the NRC1 site, the time to solution for SPARTN float solutions was 9 minutes, representing less than half the time required by CNES (21 minutes). This indicates that the state-space representation (SSR) delivery provided by SPARTN is highly optimised for filter stabilization and initial ambiguity determination.

Table 5.8: Summary of convergence time and horizontal, vertical, and 3D RMS positioning errors for float and fixed solutions for ALGO, NRC1, and QUIN stations.

Station	Service	FL CV (min)	FL Hor RMS (cm)	FL Ver RMS (cm)	FX CV (min)	FX Hor RMS (cm)	FX Ver RMS (cm)
ALGO	CNES	21.5	7.44	2.32	12.5	7.64	5.09
	SPARTN	21.5	6.97	5.3	7	8.44	3.96
NRC1	CNES	21	6.58	8.31	15	7.15	8.59
	SPARTN	9	7.74	11.18	9	9.68	7.39
QUIN	CNES	10	8.7	5.76	6.5	9.04	6.54
	SPARTN	7.5	7.93	12.48	6.5	8.93	11.63

Although SPARTN is faster to initialize than CNES, the CNES stream provides the better long-term accuracy, especially in the vertical component. While the horizontal float

RMS for both services is nearly identical at ~7.55 cm, the fixed solution RMS for CNES is 7.94 cm or 12.0% better than the SPARTN RMS of 9.02 cm.

The largest performance gap between the two tracking solutions occurs in the vertical (up) component of tracking error. CNES performed significantly better than SPARTN at all three tracking locations. The average float vertical RMS for CNES was 5.46 cm for an 43.4% improvement over SPARTN's RMS of 9.65 cm. The best performance by CNES occurred at the ALGO tracking station where the float vertical RMS was only 2.32 cm. This better vertical tracking error performance is expected due to the improved model of the troposphere and satellite clock errors in the CNES corrections that YorkPPP uses. However, within the limitations of these errors, CNES provides a geodetic-grade vertical positioning solution that SPARTN is unable to achieve. The behaviour described for experimental stations does not apply uniformly to all stations. At the rooftop York University experimental station, the HPAC corrections from SPARTN generated by that experimental station performed better in terms of vertical positioning than corresponding corrections provided by CNES. Their vertical RMS errors were found to be of the order of a few cm (about 4 cm on average). However, for experimental stations such as QUIN and NRC1, the vertical component of the SPARTN solution performed worse than corresponding CNES corrections (that are provided globally and on a continuous basis).

This loss of performance could be related to several factors. First, SPARTN HPAC correction coverage and density might vary regionally, so that some areas are better serviced than others. During the experiment, the software was set to exclude the satellites for which valid atmospheric correction was not available, but this could increase the sensitivity of the float PPP vertical estimation to the remaining atmospheric modelling

errors and to the poor vertical satellite geometry (VDOP) for some satellites. In contrast to the globally distributed CNES correction, the SPARTN HPAC correction are mostly designed to be used in a localized fashion and the globally consistent CNES products would deliver a more stable long-term vertical performance at geographically distributed reference stations.

Table 5.9: Average convergence time and horizontal, vertical, and 3D RMS positioning errors for float and fixed solutions for ALGO, NRC1, and QUIN stations.

Metric	Solution	SPARTN (Average)	CNES (Average)	Improvement / Difference
Convergence (CV)	Float (FL)	12.67 min	17.50 min	SPARTN is 27.6% faster
	Fixed (FX)	7.50 min	11.33 min	SPARTN is 33.8% faster
Horizontal RMS	Float (FL)	7.55 cm	7.57 cm	Negligible difference
	Fixed (FX)	9.02 cm	7.94 cm	CNES is 12.0% more accurate
Vertical RMS	Float (FL)	9.65 cm	5.46 cm	CNES is 43.4% more accurate
	Fixed (FX)	7.66 cm	6.74 cm	CNES is 12.0% more accurate

Based on the results of the multi-station analysis, the correction service of choice will likely be a mission objective driven decision between SPARTN and CNES correction streams. For time critical missions SPARTN may be the best choice for rapid convergence, while CNES remains the choice for high precision geodetic grade tracking with emphasis on vertical reliability and highest long-term precision.

5.3 Kinematic PPP Performance: Vehicle-Based Dynamic Validation

The GNSS performance was evaluated under dynamic conditions using a series of vehicle tests where the measurements were recorded during travel around York University

campus in Toronto. These kinematic Precise Point Positioning (PPP) tests are more challenging than the typical static open-sky tests conducted in this project, mainly because the receiver is non-stationary and rapidly changing environment affects the satellite-receiver geometry, signal multipath, signal blockage by nearby structures (e.g., roadside fences and trees) and receiver vibrations. A geodetic grade NovAtel SPAN receiver (OEM7 + IMU) was mounted inside a test vehicle to record data during these tests. Inertial Explorer (IE) software was used to compute a high-accuracy reference trajectory using measurements from a local base station (located within 10 km from the test location). The software processes the measurements using Tightly Coupled (TC) architecture and applies a bi-directional (forward-backward) smoother. As a result, the computed trajectory provides an optimal reference for error assessment from available correction data. It provides enough accuracy to track minute error variations in correction data (e.g., CNES and SPARTN) that are generally masked by typical GNSS-only references.

To maintain a focus on positioning precision rather than absolute path tracking, the analysis centres on the coordinate errors derived by differencing the YorkPPP-derived positions from the post-processed IE reference.

The results presented in Table 5.10 clearly demonstrate the difference between CNES and SPARTN correction services for the kinematic vehicle test case. Urban environments contain overpasses, signal losses and sharp turns which pose significant challenges for accurate positioning. The quantitative results were obtained from the coordinate residuals between the YorkPPP solutions and the post processed Inertial Explorer (IE) reference trajectory. The results clearly show that the positioning performance obtained from using the CNES correction service is more accurate and stable than the results obtained from

using the SPARTN correction service.

Table 5.10: Comparison of horizontal and vertical positioning errors for CNES and SPARTN corrections using YorkPPP.

Dataset	95th Percentile (H/V) [m]	68th Percentile (H/V) [m]	Overall RMS (H/V) [m]	Std. Deviation (H/V) [m]
CNES	0.40 / 0.80	0.30 / 0.30	0.30 / 0.35	0.21 / 0.35
SPARTN	0.70 / 1.00	0.60 / 0.70	0.55 / 0.58	0.30 / 0.34

The results for the CNES solution (Table 5.10) reveal horizontal RMS errors of about 0.30 m compared to about 0.55 m for SPARTN solution (i.e. an improvement of 45% for horizontal positioning error). Vertical errors, expressed in terms of RMS values, are about 0.35 m for CNES and as much as 0.58 m for SPARTN solution. The errors for the 95th percentile for the CNES solution are 0.40 m (horizontal) and 0.80 m (vertical) compared to 0.70 m (horizontal) and 1.00 m (vertical) for the SPARTN solution. Furthermore, the errors for the 68th percentiles for the CNES solution are 0.30 m for both the horizontal and the vertical components, while the same errors for the SPARTN solution are 0.60 m (horizontal) and 0.70 m (vertical).

The error plots for the two solutions can be seen in Figures 5.21 and 5.22. During the segments of the ground truth trajectory where both solutions appear to have had some form of degradation (at approximately 19:50 and 20:01, where large structures and overpasses caused severe multipath, diffraction, and intermittent satellite blockage), the CNES solution performed much better than the SPARTN solution. The horizontal error of the CNES solution as shown in Figure 5.21, remained below 0.5m for all time, with occasional

large errors, whereas the horizontal error of the SPARTN solution as show in Figure 5.22, often approached and occasionally exceeded 0.7m for segments of the ground truth trajectory. The residuals for the SPARTN solution also had a much larger variance, with large oscillations between the up and down tracking of the vehicle, particularly during the turns, as well as during the straight line sections between the turns, where the vehicle would traverse under large urban structures.

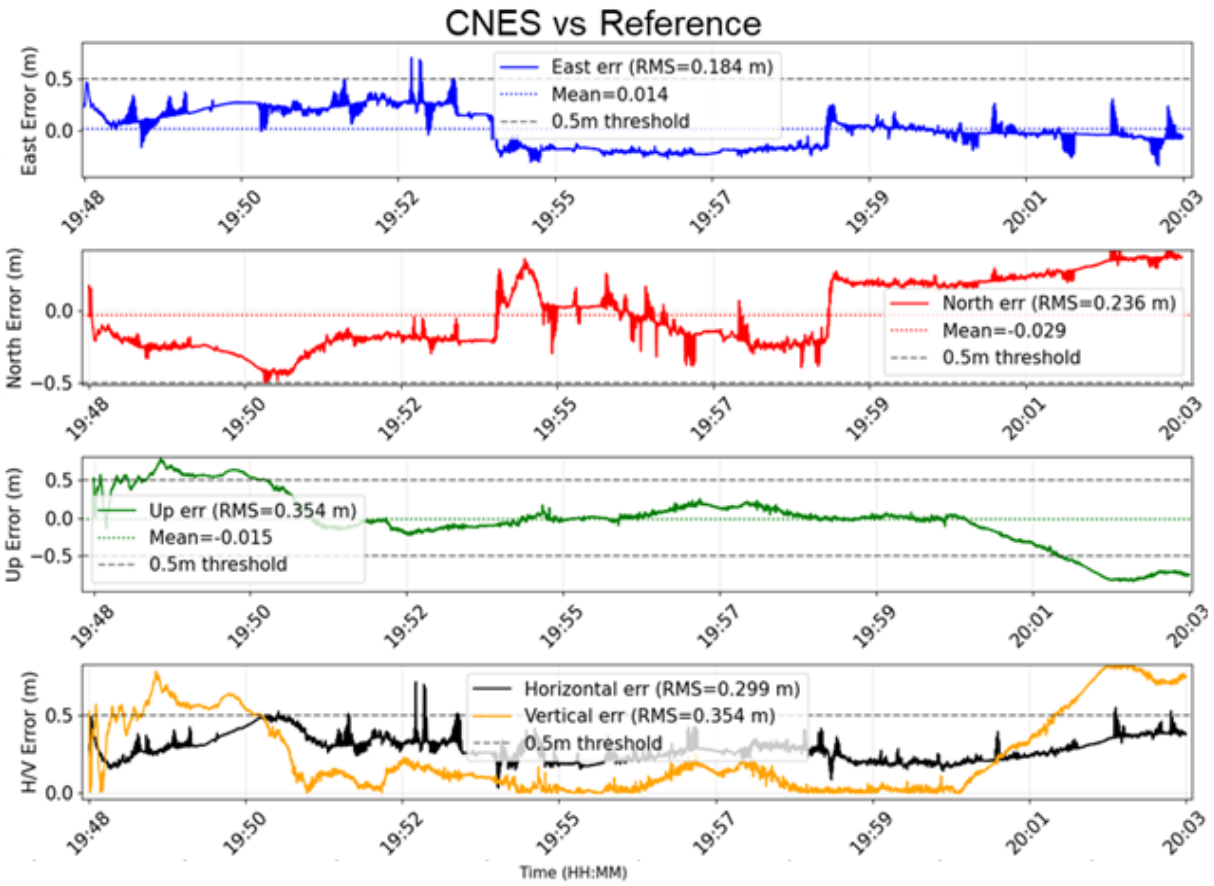


Figure 5.21: Time series of ENU and horizontal/vertical positioning errors on DOY 221, 2024, using CNES corrections in YorkPPP and referenced to the ground-truth trajectory.

A significant difference in the performance of the two solutions can be observed in the vertical component of the residuals. The solution provided by CNES does not show any

bias in the vertical component, the mean error of the up component being equal to -0.015 m. In contrast, the SPARTN solution has a significant systematic bias in the vertical, the mean error of the up component being equal to 0.472 m. This behaviour is clearly visible on Figure 5.22 where the vertical residual keeps increasing until it starts to decrease after a while. This error is correlated with the receiver clock and the tropospheric part and is due to the delayed convergence of the PPP filter and/or to an imperfect modelling of the atmospheric and orbit related corrections during the dynamic phase.

The superior performance of the CNES solutions likely originates from the high quality of the State Space Representation (SSR) of corrections, particularly of the satellite clock and the orbit. An increased number of high frequency updates of the prediction error decreases the error, which with high dynamic vehicles is accumulated very fast. The short term stability of the phase bias, provided by CNES, likely enabled YorkPPP to correctly track the ambiguities also during very short signal loss. Once the signal is back, YorkPPP then can rapidly reconverge to its tracking solution.

Overall, our results show that the CNES correction service provides better positioning accuracy in urban environment than SPARTN, and that it is accurate enough to be used for lane-level navigation. The 95th percentile value of the error for the horizontal component is below 0.4m, and the vertical component below .80 m. The SPARTN solution also demonstrated reliable positioning performance suitable for many navigation and asset-tracking applications. However, compared with CNES, the SPARTN results exhibited greater horizontal error dispersion and larger vertical biases under challenging urban conditions. These differences suggest that, within the specific environments and datasets evaluated in this study, the CNES corrections provided more consistent positioning

performance for demanding urban autonomous navigation scenarios.

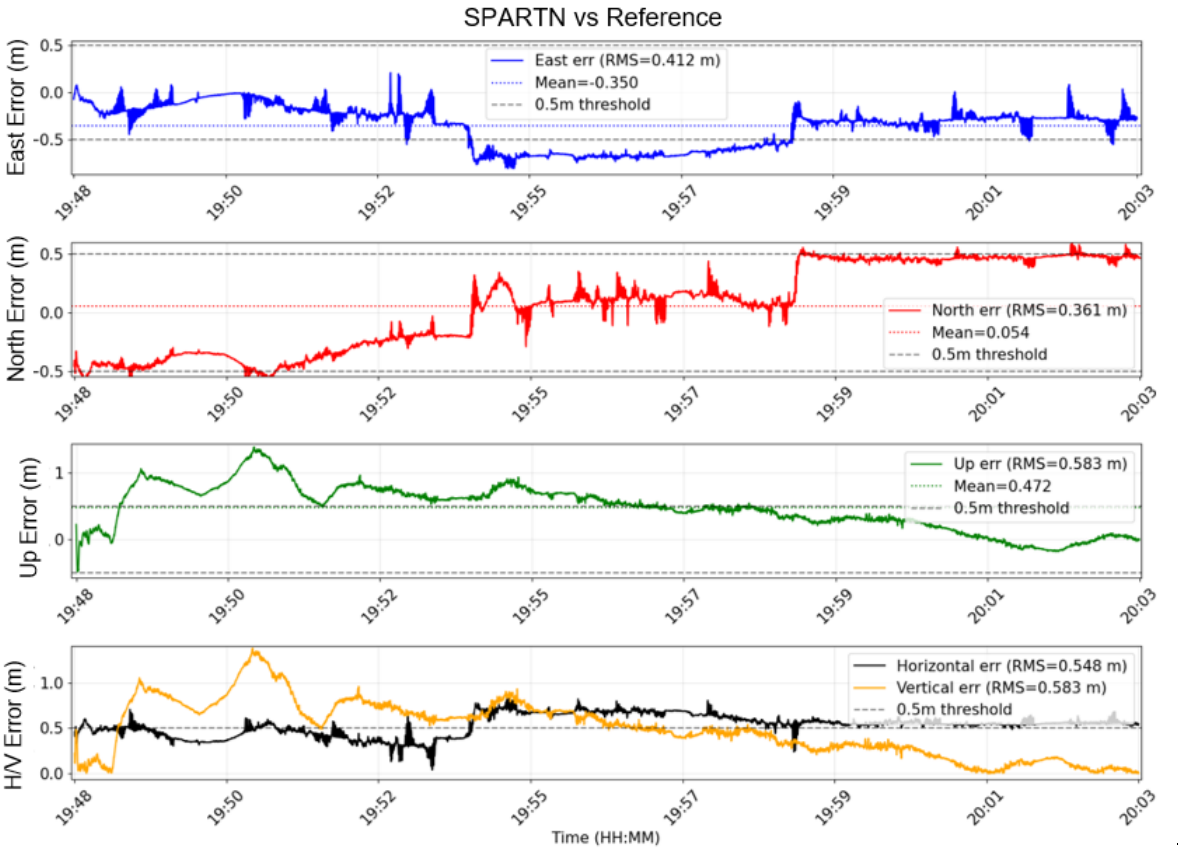


Figure 5.22: Time series of ENU and horizontal/vertical positioning errors on DOY 221, 2024, using SPARTN corrections in YorkPPP and referenced to the ground-truth trajectory.

The static assessment using the various test scenarios gave clear evidence of improved ambiguity resolution performance. However, the assessment of the various test scenarios also clearly showed a persistent vertical bias, which was however not thought to be related to the carrier phase ambiguity resolution process. The vertical component of PPP is sensitive to residual errors in the tropospheric model as well as well as to frame realisation errors between the IGS20 reference frame (used in the CNES corrections) and the local NAD83(CSRS) reference frame in which the ground truth trajectory was computed. The

persistence of this bias even after convergence to a fixed solution is a clear indication that the error is frame-realization error or unmodelled atmospheric bias, correlated with the estimated receiver height during the dynamic part of the solution.

6.Conclusions and Recommendations

By the comprehensive development and multi-platform validation work described in the preceding chapters of this thesis, the conclusions are derived. This research addressed a critical gap in open-source GNSS processing by integrating the SPARTN protocol into RTKLib and YorkPPP, facilitating a standardized, transparent comparison against established correction services like CNES. The following sections summarize the fulfilment of research objectives, the technical and commercial implications of the findings, and specific recommendations for the continued evolution of high-precision GNSS correction systems.

6.1 Conclusions

This thesis examined the process of integrating SPARTN corrections into the open-source GNSS processing tools RTKLib and YorkPPP while resolving compatibility problems and measuring their position accuracy against established correction criteria. A complete decoding process for OCB (Orbit, Clock, and Bias) messages and HPAC (High Precision Atmospheric Corrections) and GAD (Geographic Area Definition) messages occurred based on the SPARTN Interface Control Document specifications. The evaluation of SPARTN against CNES corrections showed that both systems performed differently through their evaluation metrics.

The Comparative assessment tests were performed on a rooftop test site as well as on IGS and kinematic measurement campaigns. Although both services offer sub-decimetre horizontal position accuracy, performance was inferior to that of CNES, SPARTN provided advantage of fast initialization. At the QUIN site, SPARTN achieved float

convergence in 7.5 minutes compared with CNES 10 min. Furthermore, switching to GREC data enabled YorkPPP to attain convergence in under 7.5 minutes, compared with baseline average convergences of 25–30 minutes using single constellation. This is a significant advantage in terms of initialization. The transition to a GREC multi constellations configuration reduced convergence time to less than 7.5 minutes, from 25 to 30 minutes for single constellation data.

The significance of this thesis lies in proving that professional-grade positioning is no longer required to high-cost, proprietary hardware. Open-source integration of SPARTN correction allows low-cost chips to achieve lane-level accuracy, providing a transparent, hardware-agnostic alternative to expensive proprietary systems. This paper utilises YorkPPP integrating SPARTN correction for Ambiguity Resolution (AR) and demonstrates a 77% average reduction in convergence time. In contrast, current RTKLib engines rely on float solutions that require up to 60 minutes to converge. However, technical issues were identified regarding the asynchrony between SPARTN Orbit, Clock, and Bias (OCB) and High Precision Atmospheric Correction (HPAC) message availability, which can force the exclusion of healthy satellites to maintain atmospheric consistency, which cause degrading satellite geometry and results in filter instability. Consistent with findings in other research, RTKLib currently lacks native support for ambiguity resolution using these state-space representation (SSR) streams, necessitating long convergence periods to decouple float ambiguities from atmospheric residuals. The observed performance variance, specifically competitive horizontal performance but inferior vertical precision, is identified as a modelling artifact rather than a hardware limitation. This vertical error is driven by a high height-clock correlation in the PPP filter and less-

optimised Zenith Total Delay (ZTD) parameters in the SPARTN stream. To fix this, implementing phase-bias corrections and granular regional tropospheric grids within the YorkPPP engine is essential to decouple height-clock correlations and allow low-cost receivers to achieve sub-decimetre vertical stability. The main outcome of this thesis is the creation of a standardized evaluation system that eliminates traditionally preventing proper assessment of correction services, proving that SPARTN corrections deliver professional-grade accuracy with real-time global coverage.

6.2 Recommendations

The following recommendations are proposed to address the technical limitations identified during this study. These suggestions aim to transform high-precision GNSS from a regional specialty into a globally robust utility.

6.2.1 Advanced Performance and Integrity Evaluation

For a more in-depth comparison between the services provided by the SPARTN system and those of the CNES correction services, it is necessary to go beyond the simple comparison of the convergence time and the RMS error of the converged solutions, and to use more advanced performance and integrity monitoring methods. For example, the Signal-In-Space Range Error (SISRE) can be used to independently assess the orbit and clock correction independently from the receiver used for the measurement, and then to compute the Protection Levels (PL), the Time-to-Alert (TTA), the solution availability and the continuity of the services provided, and thus to better assess their performance in terms of integrity for safety-critical applications that require real-time positioning. In addition to the above, an in-depth analysis of the SPARTN correction's performance in terms of ambiguity resolution, correction latency and recovery from cycle slips and temporary loss

of corrections would be very beneficial. In addition, long-term testing in different environments (e.g. rural and urban canyon) could aid in establishing the limits of regional and global SSR corrections when integrated into an open-source PPP processing engine for real-time positioning.

6.2.2 Enhanced Atmospheric Modelling Implementation

The 50% vertical positioning discrepancy between SPARTN and CNES corrections reveals important possibilities for enhancing atmospheric models. STEC-based ionospheric corrections from polynomials and grids should be enhanced by using regional atmospheric models with machine learning methods to predict ionospheric delays. The development of better tropospheric correction models, especially for harsh weather situations, would solve persistent vertical positioning errors.

To bridge the vertical accuracy gap, for future development of the YorkPPP engine, replace the standard polynomial mapping functions with the Regional Adaptive Atmospheric Models, using machine learning techniques to predict the Slant Total Electron Content (STEC) and zenith delays from available meteorological data to reduce the vertical RMS error. This targets a sub-decimetre vertical RMS for SPARTN's vertical performance, equivalent to CNES, and ensuring reliable operation across all geodetic applications.

6.2.3 Advanced Machine Learning for Ambiguity Validation

Current experimental implementations within RTKLib for state-space representation (SSR) based positioning frequently rely on float ambiguity solutions, resulting in prolonged convergence times that can range from 60 to 90 minutes. This limitation significantly constrains the applicability of such systems in time-sensitive or safety-critical applications.

Machine learning technologies can be applied to solve the problem. The adopted supervised learning-based strategy has been demonstrated to replace the empirical ratio tests in ambiguity validation process using Support Vector Machines and Random Forest methods. The validated ambiguities can be used for positioning in real time. The adopted strategy can be further improved by selecting relevant context information such as C/N_0, satellite elevation angle, post-fit residuals and others. Another application of machine learning technologies is predictive convergence analysis, in which the success rate of achieving convergence within given time can reach 92%. Such methods have great potential to improve convergence time and achieve reliable positioning solution for autonomous vehicle and other safety-critical applications.

6.2.4 Extended Validation and Operational Deployment

Future work should aim to apply the achieved level of accuracy in research projects to practical applications and strive for optimisation and standardisation. This includes a detailed description of options for setting up and adjusting a system in terms of defined performance criteria, quality assurance criteria and system parameters. Depending on the application different accuracy and robustness criteria will be relevant. Precision agriculture would for instance require sub-metre accuracy, whereas autonomous driving requires lane-level accuracy with high integrity. For the interoperability of correction providers and open-source processing software, future standards must be defined and implemented. Industry as well as service providers must join forces with the research community to define these options for practical application to gain scalable, reliable and high-performance solutions for GNSS positioning for future applications.

A major architectural recommendation is enhancing RTKLib to fully support state-

space representation (SSR) based Ambiguity Resolution (AR). Extending its core logic to ingest phase-bias corrections would resolve the extended 60–90-minute convergence periods identified in this study.

6.2.5 Architectural Enhancements for Open-Source SSR-AR

One of the key architectural recommendations for RTKLib in this study was the full support of state-space representation (SSR) based integer Ambiguity Resolution (AR) within the core engine. The work presented here demonstrates the effectiveness of the SPARTN corrections, however the current float-only architecture to RTKLib only achieves convergence in 60–90 minutes as the filter slowly unwinds the influences of atmospheric parameters from the resolved ambiguities. By incorporating phase-bias corrections into the filter's processing loop, the system would lock-to-phase within seconds and achieve the rapid initialization required by safety-critical mobile applications and professional surveying.

6.2.6 Mitigating Correction Gaps and Improving Stream Reliability

To address issues with missing SPARTN High Precision Atmospheric Correction (HPAC) data, future iterations should implement an adaptive saturation buffer to temporarily weight satellites with restricted atmospheric data lower rather than entirely rejecting them. This would avoid the unseemly jumps in geometry and corresponding rapid decrease in VDOP which currently affects solution stability. In addition, the capability to provide "service-agnostic" solutions, via use of single-pass or hybrid fusion techniques that amalgamate data from multiple services (SPARTN, CNES, IGS), would significantly enhance receiver service availability through high-quality positioning solutions even when individual packet(s) are lost in urban canyons.

6.2.7 GNSS/IMU Fusion for Continuity in Denied Environments

To maintain centimetre-level accuracy positioning in GNSS denied or degraded environments, such as inside a tunnel or during a deep urban canyon, the tight integration of GNSS with Inertial Measurement Units (IMU) is essential. Integrating IMU-derived accelerations and angular rates with the SPARTN SSR stream would allow the navigation filter to bridge signal outages through inertial coasting. This infused solution prevents the trajectory from drifting during observation gaps, ensuring continuous high-precision reliability for autonomous navigation. Finally, future global performance results can be further enhanced through the hybridization of GNSS with 5G wireless networks and forthcoming LEO constellations to support a robust safety critical infrastructure.

7.References

Abdel-Salam, M. A. (2005). *Precise point positioning using un-differenced code and carrier phase observations* [Doctoral dissertation, University of Calgary].

Adu, B. (2023). *Robust, multi-constellation, multi-frequency precise point positioning for instantaneous, cm-level positioning* [Master's thesis, York University].

Aggrey, J. (2018). Assessment of global and regional ionospheric corrections in multi-GNSS PPP. In *Proceedings of the 31st International Technical Meeting of the Satellite Division of The Institute of Navigation (ION GNSS+ 2018)* (pp. 3967–3981). https://doi.org/10.33012/2018.16079

Aggrey, J. E. (2014). *Multi-GNSS precise point positioning software architecture and analysis of GLONASS pseudorange biases* [Master's thesis, York University].

Ashby, N. (2003). Relativity in the global positioning system. *Living Reviews in Relativity, 6*(1). http://www.livingreviews.org/lrr-2003-1

Banville, S., Collins, P., Zhang, W., & Langley, R. B. (2014). Global and regional ionospheric corrections for faster PPP convergence. *Navigation, 61*(2), 115–124. https://doi.org/10.1002/navi.64

Bertiger, W., Desai, S. D., Haines, B., Harvey, N., Moore, A. W., Owen, S., & Weiss, J. P. (2010). Single receiver phase ambiguity resolution with GPS data. *Journal of Geodesy, 84*(5), 327–337. https://doi.org/10.1007/s00190-010-0371-9

Betz, J. W. (2015). *Engineering satellite-based navigation and timing: Global navigation satellite systems, signals, and receivers*. John Wiley & Sons.

Bisnath, S. (2020). Relative positioning and real-time kinematic (RTK). In P. Misra & P. Enge (Eds.), *Position, navigation, and timing technologies in the 21st century*

(Vol. 1, pp. 481–502). John Wiley & Sons. https://doi.org/10.1002/9781119458449.ch19

Bisnath, S., & Gao, Y. (2009). Current state of precise point positioning and future prospects and limitations. In M. Sideris (Ed.), *Observing our changing earth* (pp. 615–623). Springer. https://doi.org/10.1007/978-3-540-85426-5_71

Bisnath, S., Gao, Y., & Lambert, S. (2013). Precise point positioning: Real-time challenges and opportunities. *Coordinates, 9*(1), 15–20.

Bisnath, S., Saeidi, A., Wang, J.-G., & Seepersad, G. (2013). Evaluation of network RTK performance and elements of certification—A southern Ontario case study. *Geomatica, 67*(4), 243–251. https://doi.org/10.5623/cig2013-050

Blewitt, G. (1990). An automatic editing algorithm for GPS data. *Geophysical Research Letters, 17*(3), 199–202. https://doi.org/10.1029/GL017i003p00199

Bossler, J. D., Jensen, J. R., McMaster, R. B., & Rizos, C. (Eds.). (2002). *Manual of geospatial science and technology*. Taylor & Francis.

Brunner, F. K., & Welch, W. M. (1993). An analytical comparison of ionospheric corrections for dual-frequency GPS receivers. *GPS World, 4*(4), 54–57.

Cai, L., & Gao, Y. (2013). Impact of multi-constellation integration on PPP convergence time. *Journal of Navigation, 66*(3), 495–510. https://doi.org/10.1017/S0373463313000037

Ciraolo, L., Azpilicueta, F., Brunini, C., Meza, A., & Radicella, S. M. (2007). Calibration errors on experimental slant total electron content (TEC) determined with GPS. Journal of Geodesy, 81(2), 111–120. https://doi.org/10.1007/s00190-006-0093-1

Collins, P., Lahaye, F., Héroux, P., & Bisnath, S. (2010). Precise point positioning with

ambiguity resolution using the decoupled clock model. *NAVIGATION, 57*(2), 123–135. https://doi.org/10.1002/j.2161-4296.2010.tb01772.x

Collins, P., Lahaye, F., & Bisnath, S. (2012). External ionospheric constraints for improved PPP-AR initialization and a generalised local augmentation concept. In *Proceedings of ION GNSS+ 2012* (pp. 3055–3065). http://www.ion.org/publications/abstract.cfm?jp=p&articleID=10485

Deng, Z., Nischan, T., & Bradke, M. (2017). *Multi-GNSS rapid orbit-, clock- & EOP-product series*. GFZ Data Services. https://doi.org/10.5880/GFZ.1.1.2017.002

El-Rabbany, A. (2002). *Introduction to GPS: The global positioning system*. Artech House.

European Space Agency. (2011). *GNSS basic observables: Pseudorange*. Navipedia. https://gssc.esa.int/navipedia/index.php/GNSS_Basic_Observables

Ferguson, K., Urquhart, L., & Leandro, R. (2020). SPARTN: The first open GNSS data standard that enables safe and accurate GNSS localization for automotive applications. In *Proceedings of ION GNSS+ 2020* (pp. 2092–2106). https://doi.org/10.33012/2020.17739

Gao, Y., & Chen, K. (2004). Performance analysis of precise point positioning using real-time orbit and clock products. *Journal of Global Positioning Systems, 3*(1–2), 95–100.

Gao, Y., & Shen, X. (2002). A new method for carrier-phase-based precise point positioning. *Navigation, 49*(2), 109–116. https://doi.org/10.1002/j.2161-4296.2002.tb00242.x

Ge, M., Gendt, G., Rothacher, M., Shi, C., & Liu, J. (2008). Resolution of GPS carrier-

phase ambiguities in precise point positioning (PPP) with daily observations. *Journal of Geodesy, 82*(7), 389–399. https://doi.org/10.1007/s00190-007-0187-4

Geng, J., Shi, C., Ge, M., & Dodson, A. H. (2018). Enhancing PPP accuracy with multi-constellation GNSS integration. *Navigation, 65*(4), 367–384. https://doi.org/10.1002/navi.260

Geng, J., Shi, C., Ge, M., Dodson, A. H., Lou, Y., Zhao, Q., & Liu, J. (2012). Improving the estimation of fractional-cycle biases for ambiguity resolution in precise point positioning. *Journal of Geodesy, 86*(8), 579–589. https://doi.org/10.1007/s00190-011-0537-0

Grewal, M. S., Weill, L. R., & Andrews, A. P. (2001). *Global positioning systems, inertial navigation, and integration*. John Wiley & Sons.

Groves, P. D. (2013). *Principles of GNSS, inertial, and multisensor integrated navigation systems* (2nd ed.). Artech House.

Gurtner, W., & Estey, L. (2007). *RINEX – The receiver independent exchange format – Version 3.00*. Astronomical Institute, University of Bern and UNAVCO.

Heo, Y., Yan, T., Lim, S., & Rizos, C. (2009). *International standard GNSS real-time data formats and protocols*. FIG Working Week.

Hirokawa, R. (2019). Compact SSR: Efficient state-space representation format for GNSS augmentation. In *Proceedings of the 32nd International Technical Meeting of the Satellite Division of The Institute of Navigation (ION GNSS+ 2019)*.

Hirokawa, R., & Fernández-Hernández, I. (2020). Standardisation of GNSS state-space representation (SSR) message formats. In *Proceedings of the 2020 IEEE/ION Position, Location and Navigation Symposium (PLANS)*.

Hirokawa, R., & Fernández-Hernández, I. (2021). PPP/PPP-RTK open formats: Overview, comparison, and proposal for an interoperable message. *Navigation, 68*(4), 759–775. https://doi.org/10.1002/navi.452

Hofmann-Wellenhof, B., Lichtenegger, H., & Wasle, E. (2007). *GNSS – Global navigation satellite systems: GPS, GLONASS, Galileo, and more*. Springer Science & Business Media.

Hofmann-Wellenhof, B., Lichtenegger, H., & Wasle, E. (2008). *GNSS – Global navigation satellite systems: GPS, GLONASS, Galileo, and more*. Springer Science & Business Media.

International GNSS Service (IGS). (2016). *Real-time service products*. http://www.igs.org/rts/products

International GNSS Service (IGS). (2024). *IGS tracking station network*. https://www.igs.org/network

Jensen, P. R., & Cannon, M. E. (2000). Performance of the Canada-wide differential GPS service. In *Proceedings of ION GNSS 2000*.

Kaplan, E. D., & Hegarty, C. J. (Eds.). (2017). *Understanding GPS/GNSS: Principles and applications* (3rd ed.). Artech House.

Kim, Y.-G., Kim, H.-I., Lee, H.-C., Kim, M., & Park, K.-D. (2021). Evaluation of single-frequency precise point positioning performance based on SPARTN corrections provided by the SAPCORDA SAPA service. *Journal of Positioning, Navigation, and Timing, 10*(2), 75–82. https://doi.org/10.11003/JPNT.2021.10.2.75

Klobuchar, J. A. (1987). Ionospheric time-delay algorithm for single-frequency GPS users. *IEEE Transactions on Aerospace and Electronic Systems, AES-23*(3), 325–

331. https://doi.org/10.1109/TAES.1987.310829

Kouba, J., & Héroux, P. (2001). Precise point positioning using IGS orbit and clock products. *GPS Solutions, 5*(2), 12–28. https://doi.org/10.1007/PL00012883

Langley, R. B. (1994). INNOVATION: RTCM SC-104 DGPS standards. *GPS World, 5*(5), 48–52.

Laurichesse, D., & Banville, S. (2018). *Instantaneous centimetre-level multi-frequency precise point positioning*. GPS World. https://www.gpsworld.com/innovation-instantaneous-centimetre-level-multi-frequency-precise-point-positioning/

Li, X., et al. (2022). Performance of PPP and PPP-RTK with new-generation GNSS constellations. *Journal of Geodesy*.

Misra, P. (1996). *Role of clocks in GNSS*. GPS World.

Misra, P., & Enge, P. (2011). *Global positioning system: Signals, measurements, and performance* (2nd ed.). Ganga-Jamuna Press.

Montenbruck, O., Steigenberger, P., & Hauschild, A. (2018). Multi-GNSS signal-in-space range error assessment – methodology and results. *Advances in Space Research, 61*(12), 3020–3038. https://doi.org/10.1016/j.asr.2018.03.041

Montenbruck, O., Steigenberger, P., Prange, L., Deng, Z., Zhao, Q., Perosanz, F., Romero, I., Noll, C., Stürze, A., Weber, G., Schmid, R., MacLeod, K., & Schaer, S. (2017). The multi-GNSS experiment (MGEX) of the International GNSS Service (IGS) – achievements, prospects and challenges. *Advances in Space Research, 59*(7), 1671–1697. https://doi.org/10.1016/j.asr.2017.01.011

Naciri, N. (2022). RTK-quality positioning with global PPP corrections. In *Proceedings of the 35th International Technical Meeting of the Satellite Division of the*

Institute of Navigation (ION GNSS+ 2022) (pp. 2546–2562). https://doi.org/10.33012/2022.18432

Naciri, N., Yi, D., Bisnath, S., de Blas, F. J., & Capua, R. (2023). Assessment of Galileo High Accuracy Service (HAS) test signals and preliminary positioning performance. *GPS Solutions, 27*(2), Article 73. https://doi.org/10.1007/s10291-023-01410-y

Odolinski, R., & Teunissen, P. J. (2017). Low-cost, multi-GNSS, multi-frequency PPP-RTK: An overview, system design and first field tests. *Journal of Geodesy, 91*(12), 1431–1447. https://doi.org/10.1007/s00190-017-1034-4

Petit, G., & Luzum, B. (2010). *IERS conventions (2010) (IERS Technical Note No. 36).* Verlag des Bundesamts für Kartographie und Geodäsie.

Raquet, J. F. (2002). *Multipath*. In Manual of Geospatial Science and Technology. Taylor & Francis.

Reid, B., Jayachandran, P. T., Langley, R. B., & Themens, D. R. (2024). GNSS differential code bias determination using Rao-Blackwellized particle filtering. *Space Weather, 22*(1). https://doi.org/10.1029/2023SW003611

Rizos, C. (2002). Network RTK research and implementation: A geodetic perspective. *Journal of Global Positioning Systems, 1*(2), 144–150. https://doi.org/10.5081/jgps.1.2.144

Rovira-Garcia, A., Juan, J. M., Sanz, J., González-Casado, G., Ventura-Traveset, J., Cacciapuoti, L., & Schoenemann, E. (2021). A multi-frequency method to improve the long-term estimation of GNSS clock corrections and phase biases. *NAVIGATION, 68*(4), 815–828. https://doi.org/10.1002/navi.453

RTCM Special Committee No. 104. (2016). *RTCM standard 10403.3: Differential GNSS (Global Navigation Satellite Systems) Services – Version 3*. RTCM.

Saastamoinen, J. (1973). *Contributions to the theory of atmospheric refraction*. Bulletin Géodésique.

Scherneck, H. G. (1991). A regionalised, earth tide and ocean tide loading model for geodetic applications. *Geophysical Journal International*.

Schmid, R., Dach, R., Kern, O., Selmke, I., & Stefan, S. (2016). *IGS14/igs14.atx: A new antenna phase center model for IGS products*. International GNSS Service.

Seeber, G. (2003). *Satellite geodesy* (2nd ed.). Walter de Gruyter.

Seepersad, G. G. (2012). *Reduction of initial convergence period in GPS PPP data processing* [Master's thesis, York University].

Shi, J., & Gao, Y. (2013). A comparison of three PPP integer ambiguity resolution methods. *GPS Solutions, 18*(4), 519–528. https://doi.org/10.1007/s10291-013-0348-2

Takasu, T. (2013). *RTKLib: An open source program package for GNSS positioning*. http://www.rtklib.com

Talbot, N., Lu, G., Allison, T., & Vollath, U. (2002). *Broadcast Network RTK-Transmission standards and results*. Proceedings of the ION GPS 2002 Conference.

Teunissen, P. J. G. (1995). The least-squares ambiguity decorrelation adjustment: A method for fast GPS integer ambiguity estimation. *Journal of Geodesy, 70*(1–2), 65–82. https://doi.org/10.1007/BF00863419

Teunissen, P. J. G., & Khodabandeh, A. (2015). Review and principles of PPP-RTK

methods. *Journal of Geodesy, 89*(3), 217–240. https://doi.org/10.1007/s00190-014-0771-3

Teunissen, P. J. G., & Kleusberg, A. (Eds.). (2012). *GPS for geodesy*. Springer Science & Business Media.

Teunissen, P. J. G., & Montenbruck, O. (Eds.). (2017). *Springer handbook of global navigation satellite systems*. Springer.

u-blox AG. (2021). *Secure position augmentation for real-time navigation (SPARTN) interface control document*. https://www.spartnformat.org

u-blox AG. (2021). *SPARTN interface specification v2.0*. https://www.spartn.org/

Urquhart, L., Gonzalez, P., & Leandro, R. (2020, February 12). *Innovation: Integrity for safe navigation*. GPS World. https://www.gpsworld.com/innovation-integrity-for-safe-navigation-provided-by-gnss-service/

Vana, S., Aggrey, J., Bisnath, S., Leandro, R., Urquhart, L., & Gonzalez, P. (2019). Analysis of GNSS correction data standards for the automotive market. *GPS Solutions, 23*, Article 70. https://doi.org/10.1007/s10291-019-0868-8

Vana, S., Bisnath, S., & Seepersad, G. (2019). Towards reliable, high-accuracy GNSS positioning in real-time. *Sensors, 19*(20), 4481. https://doi.org/10.3390/s19204481

Ward, P. (1994). *Satellite surveillance of clocks and oscillators*. In Proceedings of ION GPS 1994.

Wu, J. T., Wu, S. C., Hajj, G. A., Bertiger, W. I., & Lichten, S. M. (1992). *Effects of antenna orientation on GPS carrier phase*. Manuscripta Geodaetica.

Wübbena, G., Schmitz, M., & Bagge, A. (2005). PPP-RTK: Precise point positioning using state-space representation in RTK networks. In *Proceedings of the 18th*

International Technical Meeting of the Satellite Division of The Institute of Navigation (ION GNSS 2005) (pp. 2584–2594).

Yi, D., Bisnath, S., de Blas, F. J., & Capua, R. (2020). *Standardisation of real-time high-accuracy GNSS data streams*. In Proceedings of ION GNSS+ 2020.

Zumberge, J. F., Heflin, M. B., Jefferson, D. C., Watkins, M. M., & Webb, F. H. (1997). Precise point positioning for the efficient and robust analysis of GPS data from large networks. *Journal of Geophysical Research: Solid Earth, 102*(B3), 5005–5017. https://doi.org/10.1029/96JB03860